Hydrodynamics of High Specific Power Pumps for Off-Design Operating Conditions

THÈSE N^{O} 4642 (2010)

PRÉSENTÉE LE 30 AVRIL 2010
À LA FACULTÉ SCIENCES ET TECHNIQUES DE L'INGÉNIEUR
LABORATOIRE DE MACHINES HYDRAULIQUES
PROGRAMME DOCTORAL EN MÉCANIQUE

ÉCOLE POLYTECHNIQUE FÉDÉRALE DE LAUSANNE

POUR L'OBTENTION DU GRADE DE DOCTEUR ÈS SCIENCES

PAR

Stefan BERTEN

acceptée sur proposition du jury:

Prof. M. Parlange, président du jury
Prof. F. Avellan, Dr M. Farhat, directeurs de thèse
Prof. G. Bois, rapporteur
Dr Ph. Dupont, rapporteur
Dr P. Ott, rapporteur

ÉCOLE POLYTECHNIQUE
FÉDÉRALE DE LAUSANNE

Suisse
2010

Wahrlich, keiner ist weise,
der nicht das Dunkel kennt.

H.Hesse

Acknowledgements

This work has been established during a 4.5 years research stay at the EPFL, which has been made possible by Dr. Philippe Dupont from Sulzer Pumps and Prof. Avellan at the EPFL-LMH. I like to thank especially Sulzer Pumps, but also Swiss Electric Research and the Swiss Competence Center of Energy and Mobility (CCEM) for the financial support of this work.

First and most important, I'd like to express my gratitude to my thesis directors Prof. François Avellan and Dr. Mohamed Farhat for the supervision of my work and the critical but always encouraging discussions we had.

It is impossible to perform a complex experiment as the presented one without the implication of many people from different domains and institutions. I'd like to thank the mechanical group at the workshop of the LMH, especially Mr. Louis Bezençon, for their help with the instrumentation of the machine, the design group at LMH with Mr. Foucherre, Prof. Kayal and Mr. Laurent Fabre from the EPFL-LEG, who developed the onboard data acquisition system, Mr. Rouiller and his colleagues for the support on the realization of the acquisition hardware. I like to thank also Isabelle for her help with the administrative problems, Philippe Cerutti for his support on informatics and the test bed team with Mr. Mombelli and Mr. Crittin for their recommendations on measurement hardware.

Thanks to the staff at Sulzer Pumps, Mr. Tobias Meier for the design work on the test pump, Mr. Handloser, Mr. Gallo and Mr. Eichenberger for their support during the experiments and Mr. Meuter for his critical monitoring of the performed work. Mr. Francisco Botero deserves special thanks for his very welcome help during the experiments.

Many thanks to the actual and former LMH doctoral students and post-docs, like Cécile, Sébastien, Philippe, Ali, Amir, Nicolas, Youcef, Steven, Martin, Marc, Vlad, Pierre for the discussions and the time we spent together. Olivier and Christophe, who not only gave valuable recommendations and hints for my work, but were also an important part of my non-scientific life.

Thanks to my friends Dina, Andi, Birgit, Thomas, Dörte, Mick and to my sister Claudia for keeping an eye on me, even when I remained quiet for a while.

I want to give a very special thank to Dr. J.Gülich, who critically followed up my work and offered me unique views on the alps, enriching my horizon significantly not only on the scientific side of life.

Finally I'd like to thank the members of the jury for the time and effort, they spent to evaluate this thesis and for their recommendations for the final documents.

Abstract

Part load operation of high energy centrifugal pumps is associated with increased vibration levels which may adversely affect the machines operational safety. The main sources of vibrations in centrifugal pumps are of hydrodynamic nature.

The interaction between rotating and stationary flow fields yields spatially distributed pressure fluctuation patterns, which excites mechanical vibrations of the rotating and stationary pump components. As virtually all modern, high-energy machines are operated using variable speed drives, an operation, where the excitation by rotor-stator interaction pressure fluctuations matches one of the natural frequencies of the impeller or the pumps stationary components, appears to be unavoidable during the impeller life span. This may yield, provided these vibrations are not sufficiently damped, structural damage to the centrifugal pump components.

Moreover, at off-design operation of centrifugal pumps, further phenomena are superposed to the Rotor-Stator interaction effects. Local flow separations affect the flow structure in the hydraulic components, modifying existing and creating supplementary hydraulic forces as excitations for deformations and vibrations at additional frequencies.

In the present work, experimental investigations of part-load hydrodynamic phenomena as sources of mechanical excitations in a conventional, high-energy centrifugal pump stage are presented. These investigations include unsteady pressure fluctuation measurements in the rotating and stationary elements of the investigated pump stage, performed at different rotational speeds and operating points. The unsteady pressure measurements were accompanied by measurements of impeller deformations using strain gauges embedded in the impeller shroud wall. The acquired data have been completed by measurements of shaft and bearing housing vibrations.

The measurements at part-load operation unveiled the existence of stationary and rotating instabilities in the diffuser of the pump stage, referred as stall. Stationary stall, which expresses itself as a non-rotating high pressure zone in the Rotor-Stator interface, yields additional pressure fluctuations at the rotational frequency and its harmonics. At specific relative flow rates, this high pressure pattern begins to rotate around the impeller circumference. This slowly rotating high pressure zone has a dramatic impact on the mechanical behavior of the pump stage. On the one hand, it forms the highest contribution to the impeller shroud strain, generating deformations several times higher than the ones generated by rotor-stator interaction pressure fluctuations. The perturbations in the circumferential pressure distribution yield further a radial net force, slowly rotating around the impeller citrcumference. This effect has been identified using the shaft vibration measurements, where it can be shown, that the shaft centerline displacement directly follows the radial force direction. This can negatively affect the rotor system dynamic stability but can also be used to detect rotating stall during the operation of the pump, as external pressure fluctuation measurements not always allow the detection of rotating stall.

The impeller blade passage through the stall zone strongly affects the flow in the impeller side rooms. The entrainment of fluid with low circumferential velocity reduces strongly the rotation of the flow in the side rooms and thus affects the steady pressure distribution and the axial net force. The blade passage through the detachment zone adds periodic variations of the axial force acting on the impeller, which can be identified in the axial shaft vibration signature, allowing a detection of stationary stall by a thorough analysis of the axial shaft vibrations.

Keywords:

Centrifugal pumps, pressure fluctuations, Rotor-Stator interaction, Rotating stall, Part-load flow

Zusammenfassung

Teillastbetrieb von Kreiselpumpen ist üblicherweise mit erhöhten Schwingungsniveaus verbunden, die das Betriebsverhalten dieser Maschinen negativ beeinträchtigen. Die Ursachen dieses Anstiegs der Schwingungsniveaus finden sich in hydrodynamischen Vorgängen bei Teillast.

Die Interaktion zwischen rotierenden und stationären Strömungsfeldern verursacht räumlich und zeitlich verteilte Druckfelder, die mechanische Eigenfrequenzen des Laufrades, aber auch der stationären Maschinenbauteile anregen können. Diese Schwingungen, vorausgesetzt sie sind nicht hinreichend gedämpft, können bis zur Zerstörung des Laufrades führen. Da annähernd alle modernen Hochleistungspumpen bei variablen Drehzahlen betrieben werden, sind Betriebspunkte, bei denen die Druckpulsationen aufgrund von Rotor-Stator-Interaktion (RSI) eine Eigenfrequenz des Laufrades anregen, nahezu unvermeidlich.

Bei Teillastbetrieb überlagern sich weitere Phänomene mit denen der RSI Druckpulsationen. Lokale Ablösungen beeinflussen die Struktur der Strömung in den hydraulischen Kanälen und verursachen weitere Deformationen und Schwingungen bei anderen Frequenzen.

In der vorliegenden Arbeit wird eine experimentelle Untersuchung von hydrodynamischen Vorgängen als Ursache von Schwingungen und Verformungen in einer Stufe einer Hochdruckkreiselpumpe vorgestellt. Im Rahmen dieser Untersuchungen wurden transiente Druckmessungen in den rotierenden und stationären Bestandteilen des Strömungspfades durch die Pumpe bei verschiedenen Drehzahlen und Betriebspunkten durchgeführt. Darüber hinaus war die Laufraddeckscheibe mit Dehnmessstreifen und piezoelektrischen Beschleunigungsaufnehmern ausgestattet. Axiale und radiale Wellenschwingungsmessungen vervollständigten die gemessenen Daten.

Während im Auslegungsvolumenstrom neben den unvermeidlichen mechanischen Unwuchten lediglich die RSI Druckpulsationen zu den Verformungen des Laufrades beitrugen, zeigten sich bei Teillast stationäre und rotierende Instabilitäten. Stationäre Ablösung im Leitrad, die sich als eine nicht rotierende Zone hohen Druckes, gefolgt von einer Druckabsenkung auf der Saugfläche der in Drehrichtung folgenden Leitschaufel manifestiert, verursacht zusätzliche Druckpulsationen, die im Laufrad als Druckpulsationen bei Drehfrequenz und deren Harmonischen erlebt wird. Bei bestimmten Volumenströmen beginnt diese Zone hohen Druckes langsam zu rotieren. Diese Ablösezone hat einen erheblichen Einfluss auf die mechanische Belastung der Pumpenstufe. Einerseits ist sie verantwortlich für die grösste Verformung der Laufraddeckscheibe, die mehrfach grösser ist, als die Verformungen aufgrund der Rotor-Stator Interaktion. Die lokale Druckerhöhung aufgrund der Ablösung erzeugt eine Radialkraft, die im Falle der rotierenden Ablösung mit der Winkelgeschwindigkeit der Ablösung umläuft. Diese Erscheinung kann mit Hilfe der radialen Wellenschwingungsmessungen nachgewiesen werden. Es kann gezeigt werden, dass der Wellenmittelpunkt direkt durch die Position der Ablösezone bestimmt wird. Dies kann die Rotordynamik der Pumpe negativ beeinflussen, kann aber andererseits dazu genutzt werden, rotierende Instabilitäten festzustellen, da es nicht immer möglich ist, rotierende Ablösungen mit Hilfe externer Drucksensoren zu identifizieren.

Weiterhin wurde eine Beeinflussung der Radseitenraumströmung durch das Vorhandensein von Ablösungen im Leitrad beobachtet. Das Einströmen von Fluid mit geringer Umfangsgeschwindigkeit reduziert die Fluidrotation im Radseitenraum erheblich und beeinflusst so die Druckverteilung im Radseitenraum und die daraus resultierenden stationären und transienten Axialkräfte. Dies kann mit Hilfe der axialen Wellenschwingungsmessungen nachgewiesen werden.

Schlüsselwörter:

Kreiselpumpen, Druckpulsationen, Rotor-Stator Interaktion, Rotierende Ablösungen, Teillastbetrieb

Résumé

Le fonctionnement à charge partielle des pompes centrifuges à haute énergie est associé au niveau accru de vibration qui peut compromettre la sûreté opérationnelle des machines. Les sources principales de vibration dans les pompes centrifuges sont de nature hydrodynamique.

L'interaction entre les champs d'écoulement tournants et stationnaires génère des modes de fluctuations de pression distribués dans l'espace, qui peuvent exciter des fréquences propres mécaniques de la roue et peuvent créer, si les vibrations ne sont pas suffisamment atténuées, des dommages structurels. Comme pratiquement toutes les machines modernes à haute énergie opèrent à vitesse variable, l'excitation de l'une des fréquences propres de la roue par les fluctuations de pression liées aux interactions rotor-stator semble être inévitable pendant la durée de vie de la roue.

Lors du fonctionnement à charge partielle des pompes centrifuges, d'autres phénomènes s'additionnent aux effets d'interaction rotor-stator. Les décollements locaux affectent la structure de l'écoulement dans les éléments hydrauliques, en modifiant les forces hydrauliques existantes et en créant d'autres forces supplémentaires pouvant générer des déformations et des vibrations à d'autres fréquences.

Cette thèse présente une étude expérimentale des phénomènes hydrodynamiques en tant que source d'excitation dans un étage de pompe centrifuge à haute énergie. Les investigations expérimentales incluent des mesures dynamiques de fluctuation de pression dans les éléments tournants et stationnaires de l'étage analysé, exécutées à différentes vitesses de rotation et points d'opération. Les mesures dynamiques de pression ont été accompagnées de mesures de vibrations et de déformation de la roue en utilisant des jauges de contrainte et des accéléromètres miniatures piézoélectriques incorporés dans le plafond de la roue. Les données acquises sont complétées par des mesures de vibrations sur l'arbre et le porte-palier.

Les mesures à charge partielle ont dévoilé l'existence d'instabilités stationnaires et tournantes dans le diffuseur de l'étage de la pompe, identifiées comme des décollements. Le décollement stationnaire, dont la signature est une zone à haute pression stationnaire à l'interface rotor-stator, génère des fluctuations additionnelles de pression à la fréquence de rotation et à ses harmoniques. A des débits relatifs spécifiques, cette zone à haute pression commence à tourner autour de la circonférence de la roue. Cette zone à haute pression tournante a un impact dramatique sur le comportement mécanique de l'étage de la pompe. D'une part, elle est la source majeure de déformation de la paroi de la roue, produisant des déformations bien plus importantes que celle générées par les phénomènes d'interaction rotor-stator. La perturbation dans la distribution de pression circulaire induit une force radiale nette, tournant lentement autour de la roue. Cet effet a été identifié en utilisant les mesures de vibration d'arbre qui démontrent que le déplacement de l'arbre suit directement la direction de force radiale. Ceci peut affecter négativement la stabilité dynamique du rotor mais peut également être employé pour détecter le décollement tournant pendant le fonctionnement de la pompe, ce que ne permet pas toujours des mesures de fluctuations de pression externes.

En outre, le passage de l'aube de la roue dans la zone de décollement affecte l'écoulement dans les chambres latérales de la roue. L'entraînement du fluide à basse vitesse circumférentielle réduit fortement la rotation de l'écoulement dans la chambre latérale et affecte ainsi la distribution de pression et la force axiale nette. Le passage de l'aube par la zone de décollement génère des variations périodiques de la force axiale agissant sur la roue et qui peuvent être identifiées au niveau de l'arbre par une analyse complète de ses vibrations axiales.

Mots-clefs:

Pompes centrifuges, Fluctuations de pression, Interaction Rotor-Stator, Décollement tournant, Ecoulement à charge partielle.

Contents

Introduction **3**

1 Problem Overview **3**
- 1.1 Centrifugal Pumps, Development and Application . . . 3
- 1.2 Root Causes of Deformations and Vibrations in Centrifugal Pumps . . . 13
- 1.3 Flow Separation and Stall . . . 21

2 Motivation of Study and Selected Test Case **25**
- 2.1 Motivation of Study . . . 25
- 2.2 Document Organisation . . . 27

I Experimental and Analysis Tools **29**

3 Experimental Setup **31**
- 3.1 Test Loop . . . 31
- 3.2 Model Pump . . . 33

4 Instrumentation **35**
- 4.1 Transient Pressure Measurements . . . 35
  - 4.1.1 Piezoresistive Pressure Transducers . . . 35
  - 4.1.2 Sensor Calibration . . . 35
- 4.2 Strain Gauges . . . 37
- 4.3 Accelerometers . . . 38
- 4.4 Proximity Sensors . . . 38
- 4.5 Data Acquisition . . . 39
  - 4.5.1 Stationary Domain Data Acquisition . . . 39
  - 4.5.2 Rotating Domain Data Acquisition . . . 39
  - 4.5.3 Synchronisation and Final Data Archiving . . . 41
  - 4.5.4 Angular Reference and Rotational Speed . . . 42
- 4.6 Sensor Locations . . . 43
  - 4.6.1 Embedded Sensors in the Rotating Domain . . . 43
  - 4.6.2 Pressure Sensors in the Stationary Domain . . . 44
  - 4.6.3 External Pressure Sensors . . . 45
  - 4.6.4 Eddy Current Shaft Proximity Probes . . . 46

5 Analysis Definitions and Methods 47
5.1 Time Domain Definitions . . . 47
5.1.1 Mean Value and Normalization . . . 47
5.1.2 RMS Value . . . 47
5.1.3 Phase Averaging . . . 48
5.2 Frequency Domain Methods and Definitions . . . 48
5.2.1 Sampling Frequency and Filtering . . . 48
5.2.2 Fourier Transform . . . 48
5.2.3 2D FFT . . . 50
5.3 Important Parameters of Single-Input / Output Relationships . . . 51
5.3.1 Correlation . . . 51
5.3.2 Coherence . . . 51
5.4 Instantaneous Phase Based Signal Processing . . . 52

II Results and Analysis 55

6 Observed Pressure Pulsations and Global Performance Values 57
6.1 Global Performance and Associated Pressure Pulsation Patterns . . . 57
6.2 Influence of Rotational Speed on Observed Pressure Fluctuations . . . 60
6.3 Side Room Pressures and Flow Rotation . . . 64

7 Analysis of Hydraulic Phenomena for Design Conditions 67
7.1 Impeller Pressure Fluctuations . . . 67
7.1.1 Estimation of Reference Pressure and Evaluation of Pressure Fluctuations at Impeller Inlet . . . 67
7.1.2 Evolution of Pressure fluctuations in Impeller Channel . . . 70
7.1.3 Spectral Analysis and Rotor-Stator Interaction Patterns in Rotating Domain . . . 72
7.2 Pressure Fluctuations in Stationary Domain . . . 76
7.2.1 Pressure Fluctuations at Rotor-Stator Interface . . . 76
7.2.2 Evolution of Pressure Fluctuations in Stationary Domain . . . 81
7.3 Side Room Pressure Fluctuations . . . 83

8 Analysis of Part-Load Pressure Fluctuations 87
8.1 Stationary Diffuser Stall . . . 87
8.1.1 Impeller Pressure Fluctuations . . . 87
8.1.2 Diffuser Pressure Fluctuations . . . 91
8.1.3 Side Room Pressure Fluctuations . . . 93
8.2 Rotating Diffuser Stall . . . 94
8.2.1 Impeller Pressure Fluctuations . . . 94
8.2.2 Diffuser Pressure Fluctuations . . . 96
8.2.3 Side Room Stall Passage Observations . . . 98
8.2.4 Stall Rotation in Stationary Domain . . . 99

9 Analysis of Impeller Mechanical Response to Observed Pressure Fluctuations 103
9.1 Impeller Deformation Due to Rotor-Stator Interaction 103
9.2 Effect of Uneven Pressure Distribution Due to Flow Separation 106

10 Shaft Vibration Observations 109
10.1 Shaft Vibrations at Design Conditions 109
10.2 Shaft Precession due to Rotating Instability 111
10.3 Effect of Flow Separation on Axial Shaft Vibrations 113

III Conclusions and Perspective 115

Conclusions and Perspective 117

11 Conclusions and Perspective 117
11.1 Conclusions 117
11.2 Outlook 118

Appendix 123

A Hydrodynamic Bearings 123

Bibliography 129

Notations

Latin

f	Frequency	[Hz] [s^{-1}]
b	Channel width	[m]
f_N	Rotational frequency	[s^{-1}]
g	Gravitational acceleration: $g \simeq 9.81$ m/s^2	[m s^{-2}]
$\mathbf{g}$	Gravitational acceleration vector, cartesian coordinates [0 0 -g]	[m s^{-2}]
$\mathbf{n}$	Normal vector	[–]
p	Static pressure	[Pa]
t	Time	[s]
x, y, z	Cartesian coordinates	[m]
z	Number of blades, number of channels	[–]
A	Surface	[m^2]
$\mathbf{C}$	Absolute velocity	[m s^{-1}]
C	Bulk velocity	[m s^{-1}]
C_m	Meridional velocity component	[m s^{-1}]
C_n	Velocity component normal to section	[m s^{-1}]
C_u	Circumferential absolute velocity	[m s^{-1}]
E	Pump specific hydraulic energy: $E = gH_I - gH_{\bar{I}}$	[J kg^{-1}]
E	Youngs modulus	[MPa]
H	Net hydraulic head	[m]
L	Length, length coordinate	[m]
N	Rotational speed: N=60f$_N$	[min^{-1}]
P_h	Hydraulic Power	[W]
Q	Flow rate	[m^3 s^{-1}]
Q_L	Leakage flow rate	[m^3 s^{-1}]
q	Relative flow rate	[-]
R	Radius	[m]
U	Peripheral velocity: $U = \omega R$	[m s^{-1}]
V	Volume	[m^3]

$\mathbf{W}$	Relative velocity	[m s^{-1}]
$\mathbf{X}$	Location vector	[m]

Greek

α	Absolute flow angle	[–]
β	Relative flow angle	[–]
δ	Relative gap between impeller and diffuser	[–]
ε	Strain	[μm/m]
η	Efficiency	[–]
μ	Slip factor	[–]
ν	Impeller shape number	[–]
θ	Angular coordinate	[-]
φ	Rotating Mode Phase	[–]
φ_s	Stall Phase	[–]
ρ	Density	[kg m^{-3}]
σ	Mechanical stress	[MPa]
ω	Rotational velocity (Impeller)	[rad s^{-1}]
ω_s	Stall rotational velocity	[rad s^{-1}]

Subscripts

0	Reference for non-dimensional numbers
b	Impeller (blade, domain, channel)
h	Hydraulic (power, losses)
m	Mechanic (power, torque)
n	Normal to section
r	Rotating frame (angular coordinates)
ref	Reference value
∞	Free-stream value
s	Stationary frame (angular coordinates)
s	Stall
S	System
t	Transferred by impeller (torque, power), through impeller (flow rate)
v	Diffuser (vane, domain, channel)
xx	Auto-spectral power density
xy	Cross-spectral power density

Superscripts

$\bar{\ }$	Time average of measured quantity, signal mean
$\tilde{\ }$	Fluctuation of measured quantity, centered signal
$*$	Referenced to the best efficiency point (pump)
$*$	Non-dimensional, referenced by $_0$

Dimensionless Numbers

$c_{\tilde{p}}$	Pressure coefficient	$c_{\tilde{p}} = \dfrac{p - p_{ref}}{\frac{1}{2}\rho U_{1e}^2}$
$C_{\tilde{p}}$	Discrete Fourier transform magnitude of the pressure coefficient $c_{\tilde{p}}$	
Re	Reynolds number	$Re = \dfrac{\rho C_0 L_0}{\mu}$
St	Strouhal number	$St = \dfrac{fL}{C_\infty}$
ν	Specific speed coefficient	$\nu = \dfrac{\varphi^{1/2}}{\psi^{3/4}}$
φ	Flow rate coefficient (Centrifugal pump)	$\varphi = \dfrac{C_{m,2}}{U_2} = \dfrac{Q}{2\pi b_2 R_2 \omega R_2}$
ψ	Specific energy coefficient	$\psi = \dfrac{2E}{\omega^2 R^2}$

Abbreviations

EPFL	Ecole Polytechnique Fédérale de Lausanne
LMH	Laboratoire de Machines Hydrauliques
BEP	Best Efficiency Point
BPF	Blade Passing Frequency
RSI	Rotor Stator Interaction

Introduction

Chapter 1

Problem Overview

1.1 Centrifugal Pumps, Development and Application

Pumps are technical devices to convert mechanical energy into potential energy by an increase of pressure. While positive displacement pumps rely on hydrostatic working principles, the energy conversion in centrifugal pumps is based on hydrodynamic phenomena.

Although there exists a manuscript by Leonardo da Vinci describing the use of centrifugal pumps to drain marshes [1], the first proposal of a centrifugal pump is usually attributed to Denis Papin at the end of the 17th century. He suggested a centrifugal pump equipped with an open impeller having straight vanes and a rudimentary spiral casing. The lack of appropriate high speed drives and the availability of positive displacement pumps with at that time sufficient characteristics prevented an immediate propagation of this new concept and therefore further development did not occured until 150 years later. In 1838 Combs proposed curved impeller blades and in 1839 W.H.Andrews introduced a volute casing followed 1846 by a shrouded impeller. First multistage pumps have been designed by W.H.Johnson and J.S.Gwynne. Osborne Reynolds obtained 1875 a patent for a vaned diffuser and with all necessary components available, after 1893 widespread production and use of centrifugal pumps began.

Nowadays, centrifugal pumps are amongst the most used machines, influencing every aspect of everyday processes as energy production, transportation of fluids and even solids, water supply, wastewater treatment and many more. The permanent development in the different processes, centrifugal pumps are used in, led to a continuous increase of technical demands as maximum efficiency, highest reliability even at off-design operation and high power densities. This makes a profound knowledge of all aspects of the centrifugal pump operation indispensable to permit a proper prediction of the operational behavior of the centrifugal pump and to avoid premature failures of centrifugal pump components which may have a strong economical or environmental impact.

---

[1] Leonardo da Vinci - Manuscript Ms. F, ca. 1508

Energy Conversion in Centrifugal Pumps

Fig. 1.1 shows a centrifugal pump installed between two free surface reservoirs. Provided, the flow rate Q_K in all sections is constant (no leakages, local deformations or hydroacoustic effects), the flow rate in an arbitrary section A_K is defined as

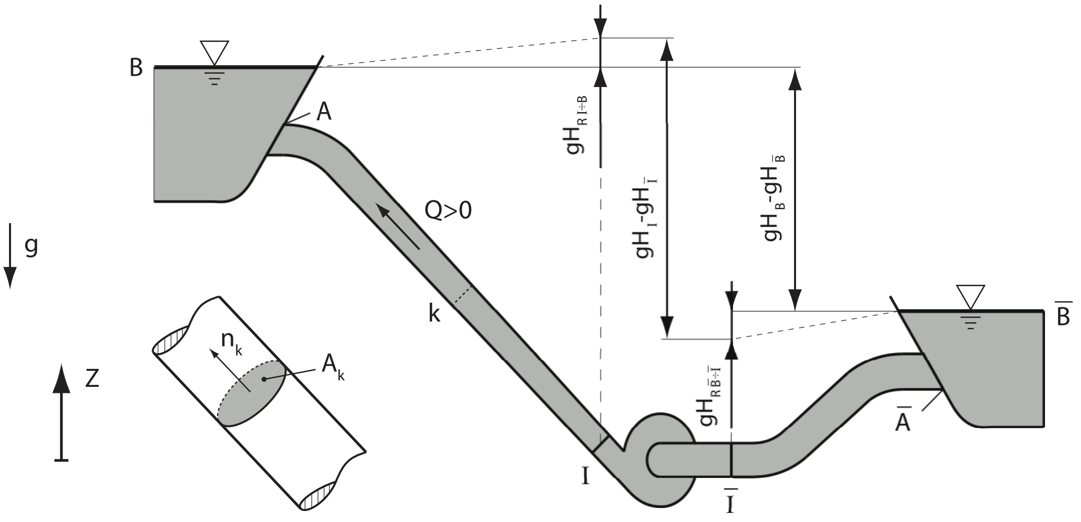

Figure 1.1: Pumping system

$$Q_K = C_k A_k = \int_{A_K} \boldsymbol{C} \cdot \boldsymbol{n} \, \mathrm{d}A \tag{1.1}$$

The mean specific hydraulic energy in the section A_k, consisting of potential energy in form of pressure p and elevation Z and of kinetic energy in form of velocity C, is defined as

$$gH_K = \frac{1}{Q} \int_{A_K} \left(\frac{p}{\rho} + \frac{C^2}{2} + gZ \right) \boldsymbol{C} \cdot \boldsymbol{n} \, \mathrm{d}A \tag{1.2}$$

The orientation of the normal vector $\boldsymbol{n}$ determines the sign convention for flow and power, it is selected in this work, as shown in Figure 1.1 to define positive flow rate and positive power, when the pump operates in its normal operating mode.

The hydraulic power transferred to the fluid in the pump is

$$P_h = \rho Q \left(gH_I - gH_{\bar{I}} \right) \tag{1.3}$$

and the transferred specific hydraulic energy is defined as

$$E = gH = gH_I - gH_{\bar{I}} \tag{1.4}$$

H is denoted as total head.

Under the assumption of an inviscid flow, the power transferred to the fluid by the impeller is given by

$$P_t = T_t \cdot \omega = \int_{A_1 \cup A_2} \rho \left(\boldsymbol{C} \cdot \boldsymbol{U} \right) \boldsymbol{C} \cdot \boldsymbol{n} \,\mathrm{d}A \tag{1.5}$$

With the flow rate passing the control volume

$$Q_t = \int_{A_1} \boldsymbol{C} \cdot \boldsymbol{n} \,\mathrm{d}A = - \int_{A_2} \boldsymbol{C} \cdot \boldsymbol{n} \,\mathrm{d}A \tag{1.6}$$

the hydraulic energy transferred in the impeller can be expressed as

$$E_t = \frac{P_t}{\rho Q_t} = \frac{\int_{A_1 \cup A_2} \rho \left(\boldsymbol{C} \cdot \boldsymbol{U} \right) \boldsymbol{C} \cdot \boldsymbol{n} \,\mathrm{d}A}{\rho Q_t} \tag{1.7}$$

Introducing coefficients of the distribution of $(C \cdot U)$ for one particular streamline (m)

$$k_{Cu1,m} = \frac{\int_{A_1} \rho \left(\boldsymbol{C} \cdot \boldsymbol{U} \right) \boldsymbol{C} \cdot \boldsymbol{n} \,\mathrm{d}A}{Q_t \left(C_{1,m} \cdot U_{1,m} \right)} \qquad k_{Cu2,m} = \frac{\int_{A_2} \rho \left(\boldsymbol{C} \cdot \boldsymbol{U} \right) \boldsymbol{C} \cdot \boldsymbol{n} \,\mathrm{d}A}{Q_t \left(C_{2,m} \cdot U_{2,m} \right)} \tag{1.8}$$

the global form of Euler's Turbomachinery equation is obtained

$$E_t = k_{Cu2,m} \left(C_{2,m} \cdot U_{2,m} \right) - k_{Cu1,m} \left(C_{1,m} \cdot U_{1,m} \right) \tag{1.9}$$

which depends on the velocity triangles (see Fig. 1.2) as well as on the velocity distribution at the low pressure (1) and high pressure (2) zones of the impeller. In the case of a purely axial inflow ($C_{1,m} \cdot U_{1,m} = 0$) and a radially uniform outflow ($k_{Cu2,m} = 1$), equation 1.9 can be transformed to

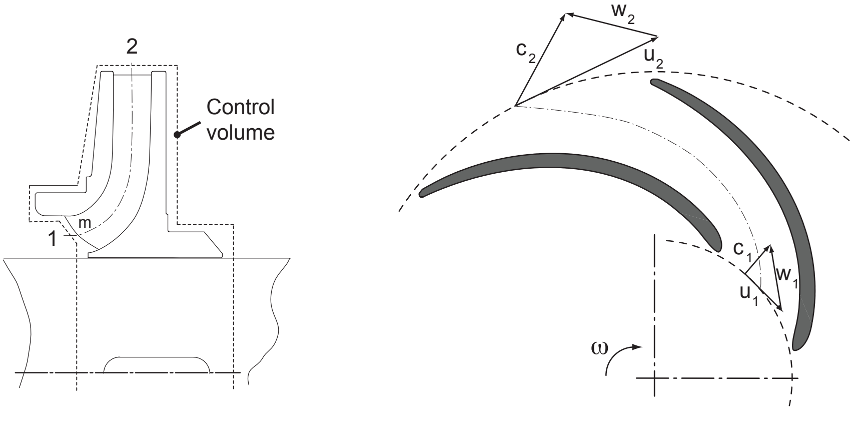

Figure 1.2: Momentum transfer in impeller

$$E = u_2 \cdot \left(u_2 - \frac{c_{2m}}{tan\beta_2} \right) \tag{1.10}$$

which defines a linear relation between the flow rate Q_t and the transferred energy in the impeller E_t.

Dimensional analysis yields the definition of a flow coefficient

$$\phi_2 = \frac{c_{2m}}{u_2} \tag{1.11}$$

and an energy coefficient as

$$\psi_2 = \frac{2E}{u_2^2} \tag{1.12}$$

The flow coefficient and the energy coefficient can be combined into a dimensionless coefficient

$$\nu = \frac{\phi_2^{1/2}}{\psi_2^{3/4}} \tag{1.13}$$

correlating with the meridional shape of the impeller, thus often referred as impeller shape number. Figure 1.3 depicts the attainable energy coefficients and the impeller shape for different specific speeds. While equation 1.13 defines a purely dimensionless coefficient, in the domain of centrifugal pumps a different, not strictly dimensionless definition is commonly used:

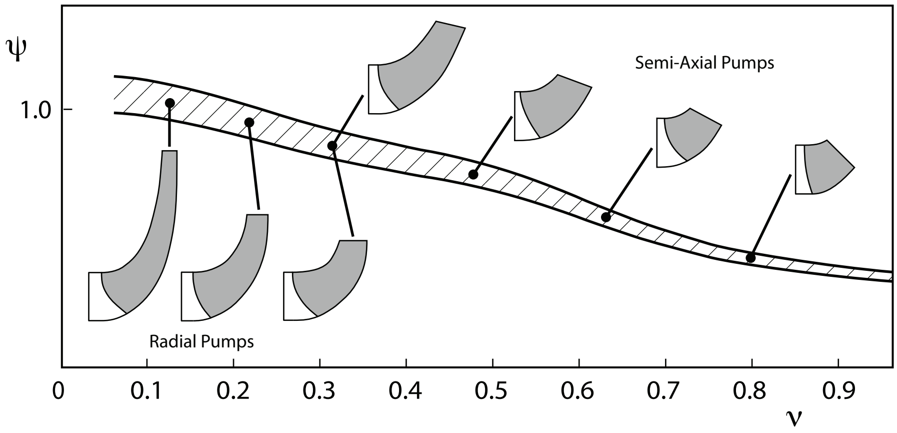

Figure 1.3: Impeller shapes and attainable energy coefficients depending on impeller shape number

$$n_q = n[rpm] \cdot \frac{(Q[m^3/s])^{1/2}}{(H[m])^{3/4}} \tag{1.14}$$

This specific speed defines the rotational speed of a geometrically similar impeller having a delivery head of 1 m and a flow rate of 1 m^3/s [103].

Due to the non-infinite number of blades, the outlet flow angle is smaller than the geometrical blade angle. This phenomenon is called slip and reduces the energy, transferred to the fluid. The slip can be defined as

$$c_{2u\infty} - c_{2u} = (1 - \mu)\, u_2 \tag{1.15}$$

Figure 1.4 depicts the outlet velocity triangle and the theoretical characteristic for different blade angles and the influence of slip.

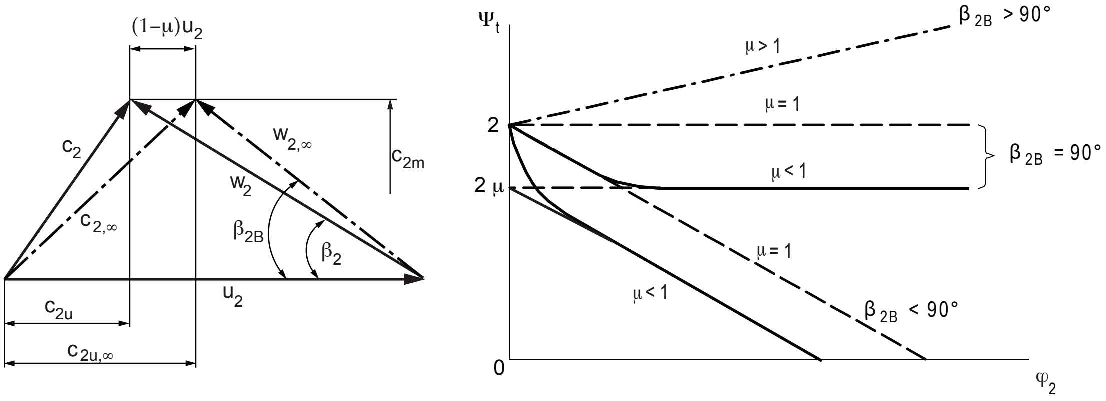

Figure 1.4: Theoretical characteristic and influence of slip

Evaluations of slip factors have been performed by Busemann [17], Wiesner [138] and Pfleiderer [103], but even recent analyses, as the one published by Backström [134] tend to predict correct slip factors only for particular geometries and need to be adapted empirically with statistical data.

Collector Geometries

The specific hydraulic energy at the impeller outlet is present as pressure energy and specific kinetic energy

$$E = \frac{p_2}{\rho} + \frac{c_2^2}{2} \tag{1.16}$$

In order to reduce losses, a significant part of the specific kinetic energy is usually converted into pressure energy by decelerating the flow in a stationary collector geometry. Two main forms of collector geometries are common, spiral casings (a) and vaned diffusers (b).

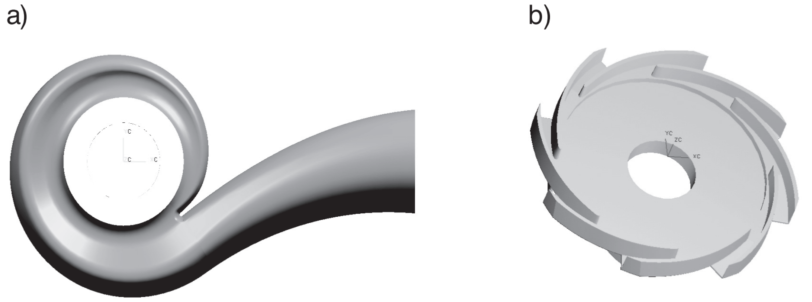

Figure 1.5: Common stationary collector geometries in centrifugal pumps

The flow, leaving the impeller, is following a trajectory, which can be described as a potential vortex

$$c_u \cdot r = const \tag{1.17}$$

until the entry of the diffuser or the end section of the spiral casing is reached. While the deceleration of the flow in spiral casings is performed in the discharge nozzle, which is executed as a straight or slightly curved diffuser, depending on the discharge nozzle position, the conversion of kinetic energy into static pressure in multistage diffuser pumps is obtained in the diffuser channels, which are defined by the diffuser vanes.

For low specific speed pumps, the diffuser inlet area is the main parameter influencing the location of the best efficiency point, generally it is assumed that the maximum efficiency is obtained, when the velocity in the diffuser throat

$$c_3 = \frac{Q}{A_3} \tag{1.18}$$

matches the absolute velocity of the approaching flow

$$c_3' = c_2 \cdot \frac{r_2}{r_3} \tag{1.19}$$

The pressure recovery depends on the length and the opening angle of the diffuser channel. The maximum opening angle of the diffuser is limited by the risk of flow separation in the diffuser channel, the diffuser length is often limited by design constraints.

Vaned diffuser channels are often designed applying empirical correlations for pressure recovery and separation limits ([79]; [43]). Diffuser channel optimization for high pressure recovery and low kinetic energy at the diffuser outlet in order to reduce the hydraulic losses in the machine or the piping system, often yields configurations, where the diffusers are operated close to their separation limits. If then, as it is the case at off-design operation of the centrifugal pump, strong non-uniformities are present in the approaching flow, flow separation can occur already at operating points close to the intended design point.

Part-load Flow in Centrifugal Pumps

With reduced flow rates, the flow in the impeller channels get increasingly three-dimensional and the relations outlined before are not valid anymore. Some analytical approaches to describe secondary flows in stationary and rotating cascades are presented in [68]. The flow patterns in the impeller are characterized by zones of flow separation and recirculation as shown in in Figure 1.6 and the pump exhibits increased vibrations and pressure fluctuations ([54]).

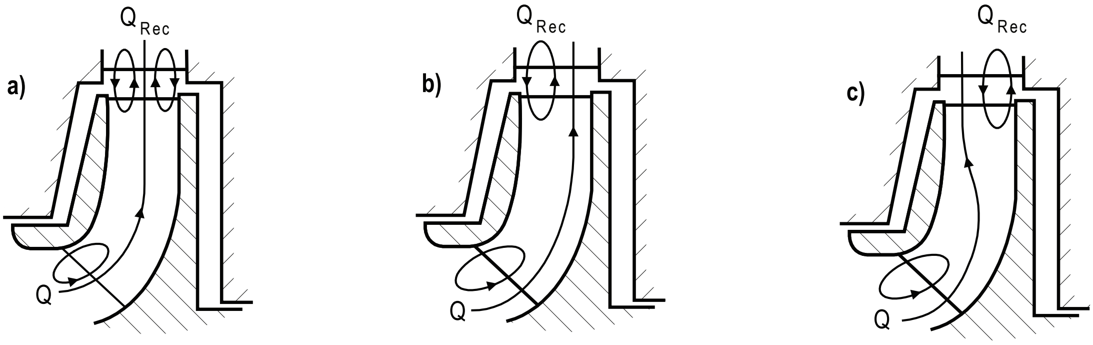

Figure 1.6: Recirculation patterns in radial centrifugal pump impellers at part load

At the impeller inlet, three physical mechanisms contribute to flow separation and recirculation:

- Deceleration of relative velocity in impeller throat
- Incidence at impeller leading edge
- Pressure gradients perpendicular to main flow

Figure 1.7 depicts the velocity relations and the velocity triangles in the impeller inlet at design flow and part load. At part-load flow, the relative velocity of the incoming fluid is reduced until the flow is sufficiently decelerated in the impeller throat area to yield flow separation. Furthermore, the incoming flow angle β_0 is reduced with reduced flow rate and, when the incidence angle, which is the difference between flow angle and blade angle, exceeds a certain value, the flow separates from the blade suction surface.

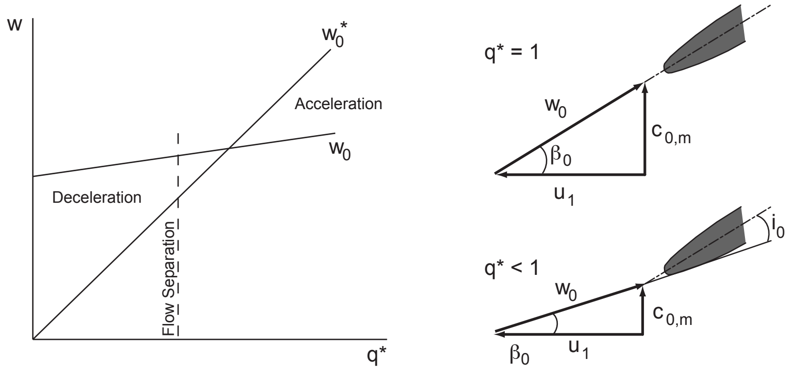

Figure 1.7: Velocity triangles and flow deceleration at impeller inlet for different flow rates

In the rotating frame of reference, defined by the impeller, the pressure gradient perpendicular to the inviscid, one-dimensional main flow on one particular streamline is determined by an equilibrium of forces caused by the following accelerations:

- Centrifugal accelerations due to rotation

$$a_{z,R} = \omega^2 \cdot r \tag{1.20}$$

- Centrifugal acceleration due to the streamline curvature

$$a_{z,SL} = \frac{w^2}{R_{SL}} \tag{1.21}$$

- Coriolis forces

$$a_c = 2 \cdot \omega \times w \tag{1.22}$$

which is expressed by

$$\frac{1}{\rho}\frac{\partial p}{\partial n} = 2 \cdot \omega \times w + r \cdot \omega^2 \frac{\partial r}{\partial n} - \frac{w^2}{R_{SL}} \tag{1.23}$$

Fig.1.8 illustrates the accelerations for a fluid element in the rotating impeller channel.

The recirculation at the impeller inlet depends on various geometrical parameters and the prediction of the onset of inlet recirculation based on empirical correlations is not possible ([56], [125]). Measurements performed by Rose [110] showed the inlet recirculation in a radial pump impeller.

The impeller inlet recirculation affects the pump efficiency, pressure fluctuations, mechanical vibration levels ([64]) and can have destructive effects on mechanical pump components and the piping system connected to the pump.

The flow at the impeller outlet tends to express separation and flow recirculation too ([74]) and the velocity distribution gets significantly changed as secondary flow patterns arise ([94]; [101]; [100]; [1]). Outlet recirculation zones as schematically shown in Fig.1.6 have been experimentally detected by Stoffel and Krieger [126], as well as Eisele et al. [34]. Meschkat [87] showed the influence of the stationary geometry downstream of the impeller, as he observed two completely different outlet recirculation patterns depending whether a spiral casing was installed downstream of the impeller or not.

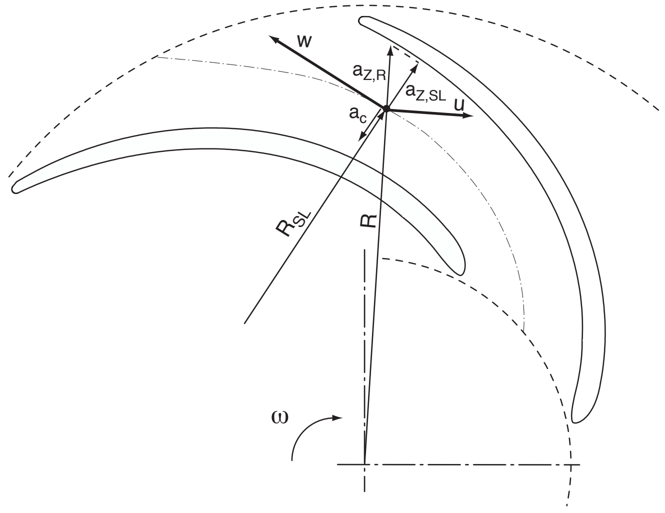

Figure 1.8: Velocities and resulting accelerations for a fluid element in the impeller channel

Essentially, as shown in Figure 1.9 and Figure 1.10 the same basic physical mechanisms, as being excessive deceleration in the diffuser throat and too high incidence angles at the diffuser vane entry are responsible for the outlet recirculation, but the geometrical parameters of the stationary components downstream of the impeller affect the form and the position of the recirculation zones ([56]). Inoue [71] performed experimental investigations of the discharge flow of an open radial (compressor) impeller and showed the occurrence of negative radial flow velocities close to the impeller shroud.

With reducing flow rates, the flow angle of the fluid approaching the diffuser inlet is reduced until a separation zone on the diffuser suction surface appears (see Figure 1.9).

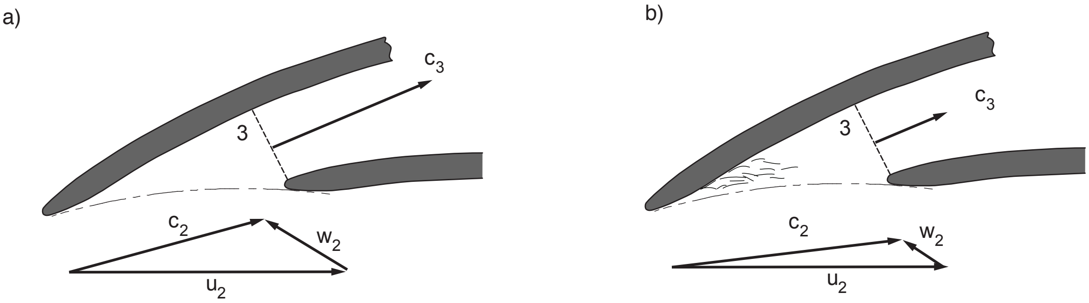

Figure 1.9: Diffuser velocity triangles at BEP (a) and part-load (b)

There have been attempts to use specific diffuser inlet profiles in order to improve the part-load behavior of the pump [137].

Another mechanism which can provoke flow separations is given by the deceleration of the absolute flow velocity in the diffuser inlet (throat) area at part load (Figure 1.10).

Although the outlet recirculation is triggered by a flow separation in the stationary downstream component, the intensity of the recirculation is believed by some authors to be influenceable. Zangeneh [140] numerically analyzed three different centrifugal impellers,

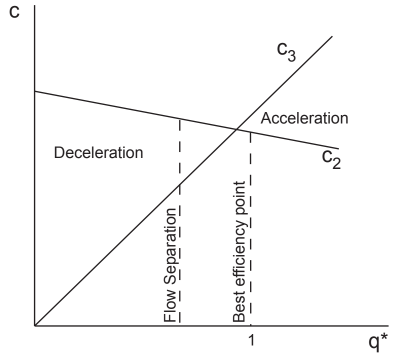

Figure 1.10: Velocity relations in the diffuser throat at different flow rates

having identical meridional shapes but different blade loading distributions in order to optimize the impeller outlet velocity distribution and to reduce secondary flows in the meridional plane. Inverse design methods as proposed by Goto and Zangeneh ([141]; [52]) tend to suggest the application of strongly inclined vanes at the impeller outlet in order to optimize the blade loading with respect to part load operation.

The recirculation at the impeller outlet has a significant influence on the stability of the head-flow characteristics, but until now, the underlying physical mechanisms are not fully understood.

1.2 Root Causes of Deformations and Vibrations in Centrifugal Pumps

General Classification of Excitation Mechanisms in Centrifugal Pumps

With respect to their causes , the excitation mechanisms of deformations and mechanical vibrations in centrifugal pumps can be classified into different categories, which will be briefly summarized here.

Mechanical and Rotodynamic Forces: Mechanical excitations can be attributed to the following causes:

- Rotor mechanical unbalance (vibration frequency equal to the rotational frequency of the shaft)
- Misalignment between motor and pump (vibration frequency equal or twice the rotational frequency)
- Forces perpendicular to the axis of rotation caused by circumferential non-uniformities in the flow in the pumps stationary components
- Rotordynamic forces, generated by the precessing movement of the shaft centerline of the centrifugal pump's rotor, containing contributions from the leakage flow through clearances and side rooms, the flow through the impeller and the flow in the bearings

Hydrodynamic Excitation Flow oscillations, appearing on a global or on a local scale are linked to pressure variations, acting as oscillating forces on the pump's components. Some of the mechanisms are listed here:

- Global flow oscillations
  - System instabilities as described in [53]
  - Acoustic resonances of the piping system with the blade passing frequency or its harmonics
  - System instabilities due to an acceleration of the reference frame (Pogo-Instabilities [127])
- Local flow oscillations
  - Interaction between rotating impeller pressure field and stationary components pressure field, called rotor-stator interaction
  - Blade excitation due to vortex shedding
  - Blade flutter
  - Stationary or rotating stall in impeller or diffuser
  - Cavitation oscillations

The mechanical dynamic loading of the pump impeller is mainly related to local flow oscillations.

Steady and Unsteady Operational Forces in Centrifugal Pumps

Radial Thrust

The circumferential pressure distribution in the stationary collector, being it a volute casing or a vaned diffuser yields a resulting steady radial force. This force depends on the geometry of the stationary collector as well as on the operating conditions. Agostinelli [3] performed radial force measurements on several volute pumps with single or double volutes. Further measurements on diffuser pumps have been performed by Hergt [62]. Figure 1.11 shows dimensionless radial forces for different stationary collector geometries. The steady radial forces can be relatively large at off-design conditions and need to be accounted for in the design of the pump bearings. The unsteadiness of the circumferential pressure distribution at off design conditions can excite vibrations and deformations of the impeller at additional frequencies (which can also contain modulated frequency contributions), as it has been shown by Guo et al. [58].

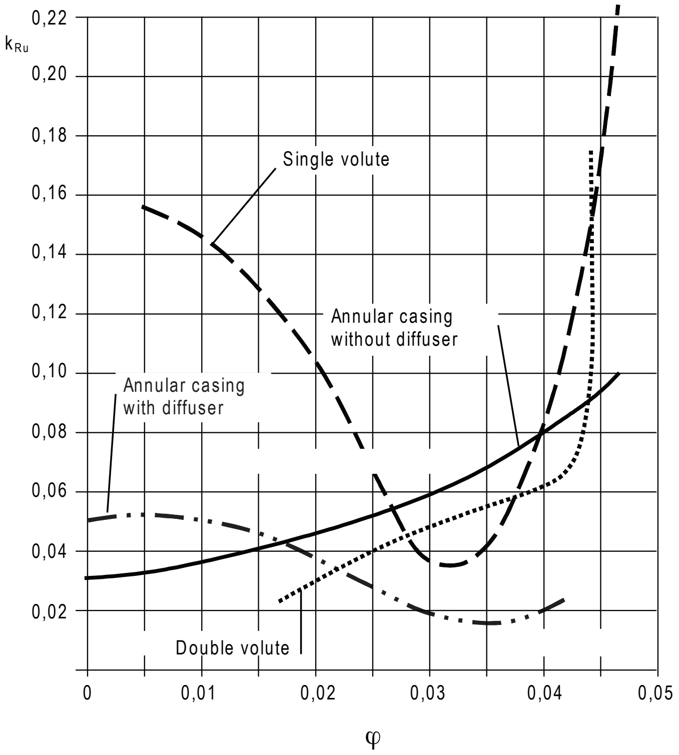

Figure 1.11: Radial thrust for different collector geometries [109]

Axial Thrust

The flow in the chamber between the rotating impeller and the pump or stage casing, referred as side room, imposes a pressure distribution as a function of the radius. This pressure distribution can be described by the Navier-Stokes equations in polar coordinates

$$\rho \frac{D\vec{c}}{Dt} = \vec{F} - \nabla p + \nabla \cdot \tau \tag{1.24}$$

which can be simplified under the following assumptions

- The flow is inviscid : $\nu = 0$
- The flow is steady: $\frac{\partial c_r}{\partial t} = \frac{\partial c_u}{\partial t} = \frac{\partial c_z}{\partial t} = 0$
- The flow circumferentially symmetric: $\frac{\partial c_r}{\partial \Theta} = \frac{\partial c_u}{\partial \Theta} = \frac{\partial c_z}{\partial \Theta} = \frac{\partial p}{\partial \Theta} = 0$
- The flow is two-dimensional: $c_z = 0$ and $\frac{\partial c_z}{\partial t} = 0$

to

$$\frac{\partial p}{\partial r} = \rho \cdot \frac{c_u^2}{r} - \rho \cdot c_r \cdot \frac{\partial c_r}{\partial r} \tag{1.25}$$

The pressure distribution in the hub and shroud side room yields a resulting axial force. Figure 1.12 depicts the flow patterns as well as the pressure distributions in the impeller hub and shroud side room.

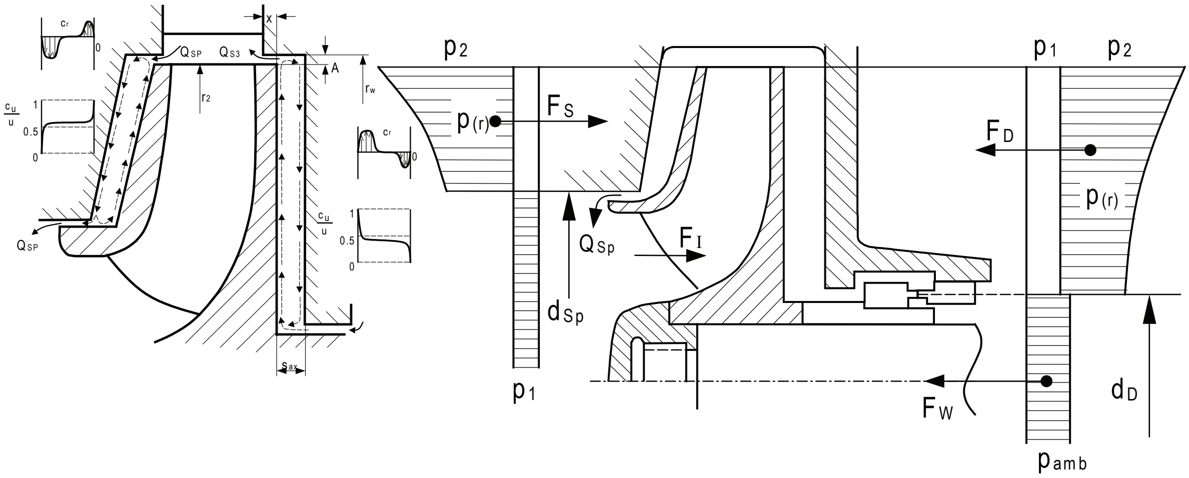

Figure 1.12: Side room definitions and flow

The flow in the impeller side rooms is rotating, driven by the impeller side walls. Superposed on this rotation is the leakage flow, depending on the machine design flowing at shroud inwards and at hub outwards (multistage pump) or inward (single stage pump and last stage of a multistage pump). The relative rotation is depending on the gap at the side room inlet, the axial width of the side room and the surface roughness of the impeller and the stationary wall. The rotation of the flow causes a reduction of the pressure following a parabolic curve. The integration of the radial pressure distribution in the side rooms yields an axial force acting on the impeller side wall, due to the different side room inner diameters a resulting axial thrust is acting on the impeller. The side room rotation can be estimated using the approach described in [56].

Under the assumption, that the fluid in a side room with leakage rotates as a potential vortex ($c_u \cdot r = const$), a dimensionless pressure reduction coefficient can be defined as

$$c_p = k^2 \cdot \left\{ 1 - \left(\frac{r_2}{r} \right)^2 \right\} \tag{1.26}$$

Zilling [144] and Moehring [91] proposed numerical procedures for a stepwise integration of the sideroom flow in order to obtain the radial pressure distribution in the side rooms.

Lauer [81] analysed the influence of the inlet boundary condition on the side room flow, while Gantar [46] investigated the active manipulation of the side room flow using devices, which either increase or reduce the flow rotation in the side room chamber. The forces resulting from the different pressure distribution in the hub and shroud side room have to be supported by an axial bearing. In multistage pumps, where the axial forces of several stages are summing up, axial force reducing devices as balance pistons or balance disks are applied in order to reduce the size of axial bearings.

Unsteady Radial and Axial Hydrodynamic Forces

Verhoeven [132], [133] and Guelich [55] give a comprehensive overview of the unsteady hydraulic forces being present during the operation of centrifugal pumps and its influencing parameters. Perez et al. [107] analyzed the influence of the radial gap between the volute tongue and the impeller blade outlet diameter on pressure fluctuations and the steady radial force in a single stage volute pump.

The steady circumferential pressure distribution in the stationary domain at the impeller outlet yields an unsteady loading of the rotating impeller. Superposed on this steady mean force, small excentricities of the impeller can yield a whirling motion of the impeller as shown by [18] and [2].

Miskovish and Brennen [88] performed measurements of dynamic radial and axial forces in a volute pump. Besides an analysis of the rotordynamic forces and moments, spectral analysis unveiled the presence of the blade passing frequency in the dynamic axial thrust, with a maximum instantaneous axial thrust, when an impeller trailing edge was close to the volute tongue.

Hasegawa [59] used a volute pump to perform experimental studies of the hydrodynamic forces acting on the impeller blades. The forces have been evaluated from the static pressure distribution on the impeller blade suction and pressure surface.

Tsukamoto [142] analyzed numerically and experimentally the hydrodynamic forces due to Rotor-Stator interaction in the unconventional case of equal impeller blade numbers and diffuser vane numbers.

Childs ([22], [23]) analyzed the stability of the side room flow using a bulk flow model (see Hsu [69] for a review of bulk flow models as used in rotodynamic analysis). These bulk flow models are now tend to be replaced by CFD RANS solvers ([92]). Poncet [104] performed experimental investigations of instabilities in the chamber between a stationary casing and a rotating disk, where a radial inflow has been superposed. In this, strongly simplified model of a side room, as found in centrifugal pumps, he demonstrated the existence of different types of instabilities. Tsujimoto et al. [130] investigated the influence of the precessing impeller motion on the rotodynamic forces generated by the side room flow.

Horiguchi et al. [67] performed analytical investigations based on the bulk flow model and experimental investigations with a disk, rotating close to a stationary disk and showed that the fluid forces can increase the axial vibrations of the rotating disk due to negative damping or negative stiffness, depending on the radial flow direction.

Guo and Maruta [58] performed experimental investigations of hydraulic excitations and the impeller response at off-design conditions with strongly nonperiodic circumferential pressure distributions and showed a modulation between the blade passing frequency and the circumferential unsteadiness, which finally led to an excitation of the impeller not only at the vane passing frequency due to the volute tongue but also at side bands, at each multiple of the rotational frequency.

The influence of part-load operation on axial vibrations in double suction pumps has been investigated by Hodkiewicz [65]. It has been found, that at low flow rates, the axial thrust strongly varied and even changed its direction.

Tanaka [129] presented the mechanical loading of high energy pump-turbine runners.

Unsteady radial forces due to hydraulic imbalance of the impeller flow are often present in rather specific impeller designs as found in sewage pumps ([12]).

Rotor-Stator Interaction

The relative motion of two closely spaced blade rows, as it is the case in centrifugal pumps and compressors, which are equipped with vaned diffusers downstream of the impeller, causes periodic pressure fluctuations at specific frequencies which are multiples of the blade passing frequency and can excite machine and component vibrations. The implications of this phenomenon, which is called Rotor-Stator interaction, are known for a long time, the first investigation concerning vibrations due to rotor-interaction in a Francis turbine has been published by DenHartog in 1930 [28].

Fig.1.13 illustrates the interaction between the flow, leaving the impeller and the pressure distribution at the diffuser vanes, which are arranged downstream of the impeller.

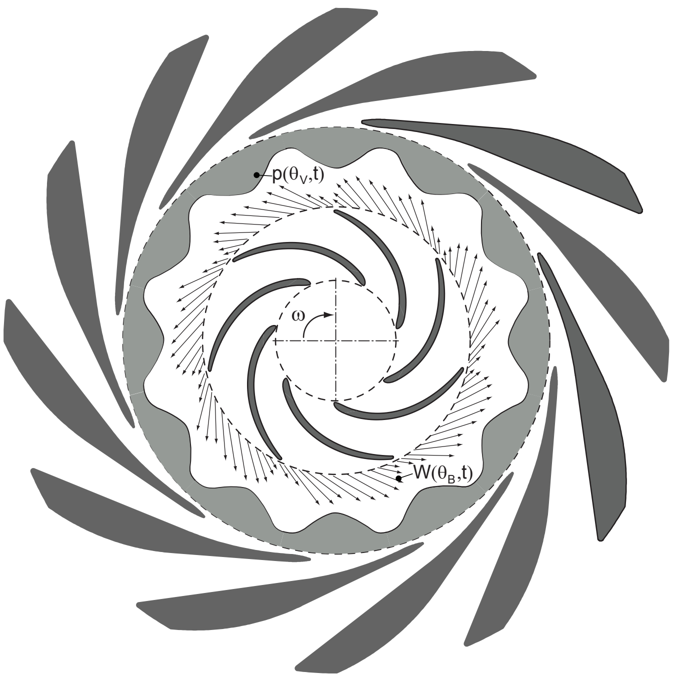

Figure 1.13: Rotor-Stator Interaction

Rotor-Stator interaction can be subdivided into two different phenomena, viscous interaction of the wake in the impeller outflow and inviscid potential flow interaction, which is resulting from the interaction of pressure gradients due to the potential flow around the impeller blades and the diffuser vanes and which extend upstream and downstream of the impeller blade and the diffuser vanes [31].

The unsteady pressure can be described as the sum of the mean pressure $\overline{\mathrm{p}}$ and the fluctuating part p'. The interaction between the rotating field at the angular coordinates θ_B and the stationary field at the angular coordinates θ_V can be described as a modulation as follows. The pressure fields in their respective reference frames can be decomposed into Fourier series

$$\begin{aligned} p'_B &= \sum_{m=1}^{\infty} p_m \cdot \cos(m \cdot z_B \cdot \theta_B) \\ p'_V &= \sum_{n=1}^{\infty} p_n \cdot \cos(n \cdot z_V \cdot \theta_V) \end{aligned} \tag{1.27}$$

and its modulation is calculated according to Bolleter [14] using

$$p'\left(\theta, t\right) = \sum_{n,m=1}^{\infty} p_n \cdot \cos(n \cdot z_V \cdot \theta_V) \cdot p_m \cdot \cos\left(m \cdot z_B \cdot \theta_B\right) \tag{1.28}$$

Rotating and stationary domain are related to each other through the relation

$$\theta_V = \theta_B - \omega \cdot t \tag{1.29}$$

which yields the time dependent pressure field in the stationary frame of reference

$$\begin{aligned} p'(\theta_V, t) \quad = \quad & \sum_{n,m=1}^{\infty} p_n \cdot \cos\left(m \cdot z_B \cdot \omega \cdot t - \left(m \cdot z_B - n \cdot z_V\right) \theta_V\right) \\ & + p_m \cdot \cos\left(m \cdot z_B \cdot \omega \cdot t - \left(m \cdot z_B + n \cdot z_V\right) \theta_V\right) \end{aligned} \tag{1.30}$$

By this equation 2 diametral pressure modes having the following number of nodes [44]:

$$k_1 = m \cdot z_B - n \cdot z_V \quad \text{and} \quad k_2 = m \cdot z_B + n \cdot z_V \tag{1.31}$$

can be found. These modes are rotating in the stationary reference frame with the angular velocities ω_1 and ω_2 ([44]):

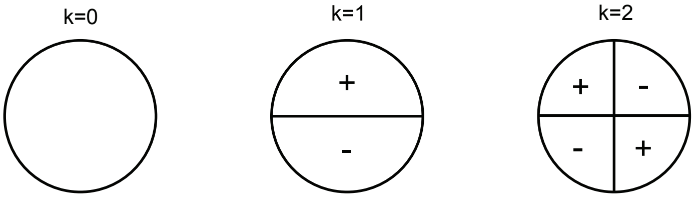

Figure 1.14: Rotor-Stator Interaction modes

$$\omega_1 = \frac{m \cdot z_B}{k_1} \cdot \omega \quad \text{and} \quad \omega_2 = \frac{m \cdot z_B}{k_2} \cdot \omega \tag{1.32}$$

The lower the mode order k is, the higher amplitudes are expected [14].

Numerous experimental and numerical investigations have been performed in order to analyze the pressure pulsation patterns due to Rotor-Stator interaction in rotating machinery. First analytical attempts to study the interaction problem are attributed to Kemp and Sears [78], who solved linearized potential equations for thin airfoils with small blade angle variations. Iino [70] numerically analyzed the potential interaction between the impeller and the diffuser in a centrifugal pump using a singularity method and showed, that an increased radial gap between the impeller trailing edge and the diffuser leading edge yields a reduction in the pressure fluctuation amplitude. Dring [31] performed detailed pressure fluctuation measurements in an axial compressor stage in order to analyze the interaction between diffuser vanes and impeller blades. Arndt et al. ([7], [8]) performed measurements in a centrifugal pump at different flow rates and radial gaps between impeller blades and diffuser vanes and showed, that the pressure fluctuations, observed in the impeller outlet, can reach significant levels up to the impeller head at part load. Ubaldi [131] analyzed experimentally the influence of a vaned diffuser on the impeller pressure and velocity and showed the strong decay of pressure fluctuations from the impeller outlet to the inlet. Dupont [32] measured the influence of the impeller outlet flow on the diffuser channel flow using 2D PIV.

Quin [108] performed numerical and experimental analysis of pressure fluctuations in a diffuser pump. The pressure fluctuations, calculated using a singularity method, agreed well with the experimental results. Shi [117] showed the capability of unsteady RANS CFD calculations to model correctly the Rotor-Stator interaction phenomena. Cizmas [24] applied proper orthogonal decomposition (POD) - also referred as principal component analysis (PCA) - to the results of a RANS simulation of a single stage axial turbine in order to analyze spatial and frequency distribution of pressure fluctuations and showed, that most of the energy is concentrated in the low-order pressure fluctuation modes. This allows to create a reduced order numerical model for the simulation of Rotor-Stator interaction in turbomachinery flows. Longatte [83] analyzed numerically the influence of the piping on rotor-stator interaction generated pressure and flow rate fluctuations in a volute pump. Zobeiri [145] performed numerical and experimental analysis of the pressure fluctuations in a pump turbine in generating mode, while Braun [15] analyzed the same geometry in pumping mode. Further numerical analyses of rotor stator interactions in pumps include [48], [40], [6], [16], [135], [143].

The influence of the the relative flow rate on the intensity of rotor-stator interaction pressure fluctuations has been shown first by Arndt et al. [8], further experimental investigations have been performed by Parrondo [99] and Akhras [4].

Spence([121], [122]) evaluated numerically and experimentally the influence of radial gap and impeller blade design at trailing edge of a single stage, double suction volute pump on pressure fluctuation amplitudes. Apart of the reduction of pressure fluctuations with increasing radial gap, they showed also a reduction of pressure fluctuations when the vanes of the two impeller halves were circumferentially staggered.

Excessive Rotor-Stator interaction pressure fluctuations may yield structural damage to the impeller or diffuser. Case studies for impeller failures are rather rarely found, but in the frame of a project on boiler feed pump reliability, initiated by the EPRI, a survey of boiler feed pump outages has been published ([84]). Prakash et al. [105] described cracks in the impeller shrouds and blade trailing edges of a feed pump rotating with 7451 rpm. Nearly all cracks appeared at the suction side impeller sidewall, some of the shrouds were completely broken. They explained the impeller failures by a too small gap between impeller and diffuser vanes, which caused unacceptable levels of pressure fluctuations. Ohashi [96] presented a case, where a side room wall broke due to excitation of a natural frequency of this side wall by rotor-stator interaction pressure fluctuations.

Compared to centrifugal pumps, high energy hydraulic turbines often have a rather fragile structure. Coutu et al. [26] reported cracks in a 447 MW Francis turbine runner after only 200 hours of operation, which they explained by the coincidence of pressure fluctuations and a structural natural frequency of the runner.

Acoustic Interaction and Phase Resonances

The rotor-stator interaction induced pressure pulsations generate acoustic waves traveling through the machine hydraulic passages as well as the piping system, the machine is connected to. If resonances occur, standing waves can cause severe vibration levels leading to structural damages of the machine or auxiliary parts [115]. Chen [19] proposed the decomposition of the pressure fluctuations into Fourier series and gave criteria to avoid phase resonances which could cause strong mechanical vibrations. The phase resonance phenomenon has been further investigated by Doerfler [30], who proposed an analytical method based on a pipe network and the use of transfer matrices. This more detailed model failed due to the lack of knowledge of the amplitude of the excitation. Morgenroth and Weaver [93] performed experimental investigations of the interaction of the blade passing frequency vibrations and the pipe network, the investigated pump was installed in. They proposed the separation of hydraulic pressure fluctuations, originating from vorticity, decaying while being convected from its origin, the rotor-stator interaction zone between impeller and diffuser, from acoustic pressure fluctuations, interacting with the acoustic properties of the flow passage and thus possibly being amplified, when coinciding with an acoustic eigenfrequency. Schneider [114] analyzed the passage of pressure waves through a single stage centrifugal pump.

Fluid-structure interaction originated problems in rotating components of fluid machinery are known for longer time in turbocompressors [33] and fans. Here, due to the lower wave speed in air, acoustic resonances in the casings and side rooms are reached in geometrically smaller machines. Eisinger [35], [36] shows how diametral acoustical modes and diametral structural modes can interact if resonance occurs. He also defines criteria, when strong coupling between acoustic phenomena and structural properties can lead to unfavorable results. Eckert [33] published a case of a broken radial compressor impeller shroud which he traced back to a self-excited aeroelastic impeller vibration. The stresses have been measured in the rotating system using strain gauges, the displacements have been measured using 2 by 90° rotated eddy current sensors at the impeller outer diameter. High vibration levels were measured in a relatively wide range of rotational speeds (2450 to 3000 rpm), the frequency of the vibrations remained nearly constant. A rotating deflection wave with 2 nodes has been identified, after 2 hours constant operation at 3000 rpm the rotating wave changed its sense of rotation. Shaft and bearing housing vibrations didn't indicate any vibrational problem in the machine. These self excited vibrations were depending on the gas, they were only observed using hydrogen ($a_0 = 1350 m/s$) no such vibrations have been observed using air ($a_0 = 350 m/s$).

Vortex Shedding

Vortex shedding occurs on hydraulic profiles trailing edges due to alternating flow detachment. This vortex shedding applies an oscillating mechanical load on the profiles trailing edge. The detachment is periodic with a frequency defined by a Strouhal number.

$$S_{Str} = \frac{f \cdot L_{char}}{w} \tag{1.33}$$

The Strouhal number depends on the geometry, values of the Strouhal number for different geometries can be found in [56].

Ausoni [9] performed extensive studies of vibrations of a hydrofoil due to turbulent vortex shedding and demonstrated the influence of cavitation on shedding frequency and amplitude. Zobeiri [146] studied the influence of the shape of trailing edge of a hydrofoil and showed, that the variation of lift forces due to vortex shedding can be significantly reduced by the application of an oblique cut at the trailing edge of the profile.

Vortex shedding appears to have a rather limited importance in radial centrifugal pumps, no publications indicating structural problems due to vortex shedding in radial centrifugal pumps are known to the author. On the other hand, mechanical problems related to vortex shedding have been reported in large hydro turbine runners and stay vanes ([118], [82], [42]).

1.3 Flow Separation and Stall

Stall refers to a backflow on a wall [79], no matter if an internal or an external flow is regarded. Flow separation or stall can be initiated by different flow phenomena as

- Incidence at profiles
- Pressure gradients normal to flow direction
- Obstacles in the flow path

Kline [79] was one of the first authors giving a comprehensive review of stall in internal flows.

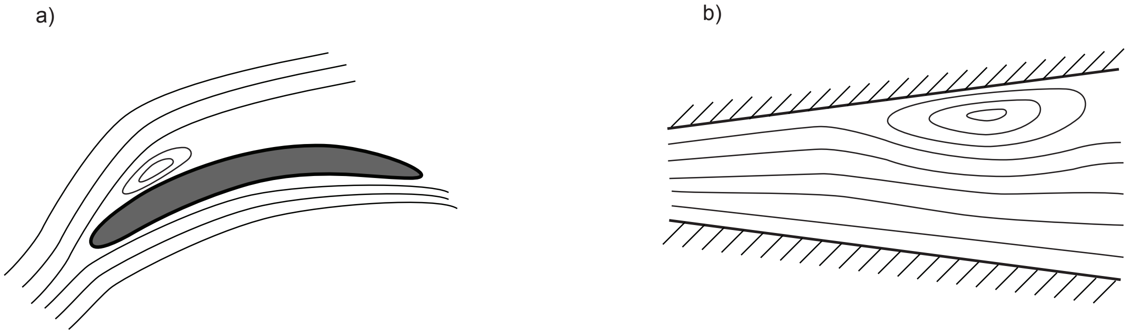

Figure 1.15: Flow separation for external (a) and internal flows (b)

Stall is a highly dynamic phenomenon, which can occur in impellers as well as in stationary components of hydraulic machinery, especially, when the flow conditions yield high incidence angles at the impeller blades or the diffuser vanes. Under specific conditions, a stationary separation zone begins to progress. This phenomenon is called rotating stall. A first explanation of rotating stall has been provided by Emmons et al. [37] along with a simplified analytical prediction model. The majority of investigations regarding rotating stall phenomena has been performed in the field of centrifugal compressors ([45], [60], [85], [41], [29],[72], [120]), while research on rotating stall in centrifugal pumps or hydraulic turbines remains relatively limited.

The common explanation of stall propagation is illustrated in Figure 1.16. The stalled channel deviates the approaching flow to the preceding and following channel.

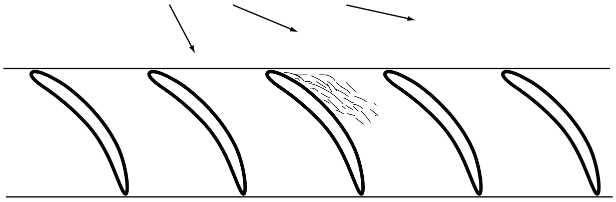

Figure 1.16: Two-dimensional, rectilinear cascade

The incidence angle for the preceding channel is increasing, while the incidence angle for the following channel is decreasing, yielding a growing separation zone at the next profile until this profile gets stalled.

For the strongly simplified case of a plane cascade, the onset of rotating stall can be determined based on a stability analysis in an infinite, two-dimensional rectilinear cascade [124].

Hergt and Benner [61] analyzed different diffusers in a free surface test stand. At different load points and different hydraulic design variations (vane number and -angle) they found rotating stall. From these observations they derived simple design recommendations for multistage pump diffusers. Akin and Rockwell [5] used high-image-density particle image velocimetry (PIV) to analyze the interaction of one stalled diffuser vane with the impeller outlet flow.

Braun [15] performed a numerical and experimental analysis of rotating stall observed in a reduced scale model of a radial pump turbine and provided a different explanation of the stall progression mechanism (Figure 1.17).

In this particular situation, the stall progression is driven by a secondary flow in the gap between the guide vanes and the stay vanes, resulting from the pressure difference between a stalled and an unstalled diffuser channel, which triggers flow separation in the subsequent diffuser channel.

Sano et al. [113] performed numerical simulations of a diffuser connected to an impeller using a moving grid method. The calculations were made "quasi" 2D, the mesh in the ground view was only one element high. Resulting from the simulation, diffuser rotating stall rotating with 10% of the impeller rotational frequency has been found. The simulated flow pattern was in accordance with the measurements of Hergt et al. [61], Sinha et al. [119], Wang [136] and Sano [112]. While in the case, studied by Sinha, the gap between diffuser and impeller vanes was large (20% of impeller radius), in Wang's analysis, the

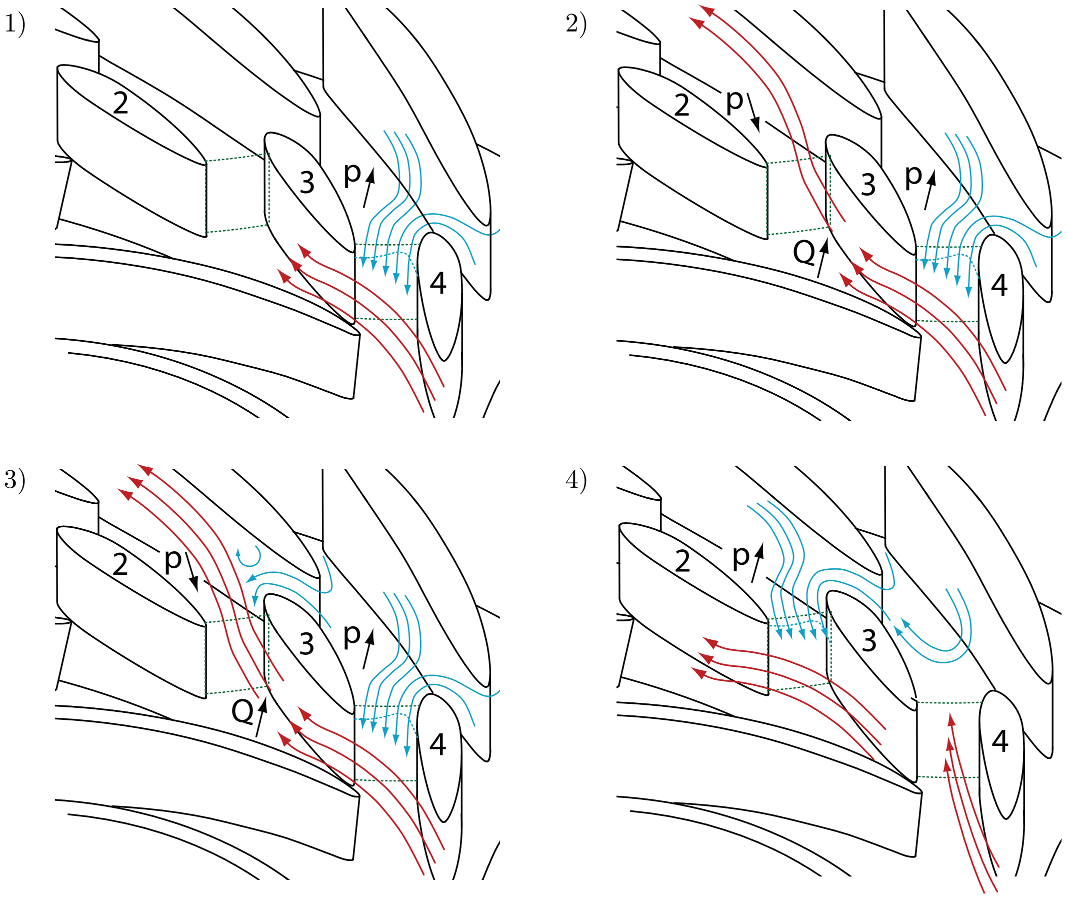

Figure 1.17: Schematic evolution of flow patterns for a pump turbine operating in pump mode [15]

gap was only 3% of the impeller outer radius and the stall rotational speed was strongly reduced. Yoshida et al. [139] analyzed rotating stall in a centrifugal pump, equipped with 2D-vanes in the impeller and in the diffuser. While the impeller had 7 vanes, different stationary geometries with 9 and 18 vanes and various radial gaps between 0.5% and 20% of the impeller diameter have been investigated. Miyabe [89] related the occurrence of rotating stall in the diffuser of a semi-axial pump to the observation of an instability in its performance curve.

Impeller rotating stall was mainly investigated in axial and radial compressors, since the surge limit, which defines the lower operating limit of compressors is often related to the appearance of rotating stall. Chen et al. ([21], [20]) developed an analogy between rotating stall flow in radial turbo compressors and the mid-latitude wind system in the earth atmosphere. This model has been later extended to axial compressors, where Rossby waves and their associated circular Karman vortex streets are again found to be the dominant factors. Krause et al. [80] investigated partload flow in a single stage volute pump and found rotating impeller stall starting at flow rates below 40% of optimum flow rate. At this flow rate the stall cell did not rotate with a constant speed, but remained longer periods in distinct channels of the 5 vanes impeller. At lower flow rates the stall cell started to rotate with an angular frequency of 88 % of the rotational frequency. Johnson et al [75] found at 25 % relative flow rate stationary stable stall cells in alternate impeller channels.

Chapter 2

Motivation of Study and Selected Test Case

2.1 Motivation of Study

High energy centrifugal pumps, which have power consumptions larger than 5 MW and rotating speeds above 5'000 rpm can be found in various applications, such as boiler feed pumps in thermal power generation or as injection pumps in the oil and natural gas exploration. The pressure rise required in these processes is too high to be obtained in one impeller, the circumferential velocity necessary to transfer the required mechanical energy to the fluid would result in mechanical loads beyond material limitations and less than maximal efficiencies are attainable. Therefore, the pressure rise is partitioned over several stages, arranged in series. This allows the selection of a hydraulic design close to the maximum attainable efficiency [128], the limitation of the impeller mechanical load and the reduction of the required suction pressure to prevent cavitation in the first stage impeller inlet.

Figure 2.1 depicts a typical multistage, high-pressure barrel pump. The pump consists of an outer barrel, containing the hydraulic components united in an exchangeable cartridge.

The liquid enters the pump through an inlet casing (1). The impeller of the first stage (2) is usually different from the remaining stage impellers (3) as it is optimized with respect to cavitation. Leaving the impeller, the fluid is guided through a vaned radial diffuser (4) and return vanes (5) to the inlet of the next stage impeller. In the last stage, the fluid is leaving the diffuser into a collection chamber (6) from where it is leaving the pump through the discharge nozzle. Multistage pumps are usually equipped with devices to balance the axial thrust generated by the different pressure distributions acting on each impeller's hub and shroud, these can be realized using a balance piston (7), as shown in Figure 2.1 or as a balance disk.

Depending on the process requirements, pumps are not always operated at their maximum efficiency flow rate, referred as best efficiency point (BEP), but are also casually utilized at flow rates below the best efficiency point, referred as part-load operation. Part-load operation is accompanied by reduced efficiency, increased pressure fluctuations and vibrations, wear and possible undesired system interactions. While at design conditions the rotating and stationary components are mainly loaded by periodic and stationary

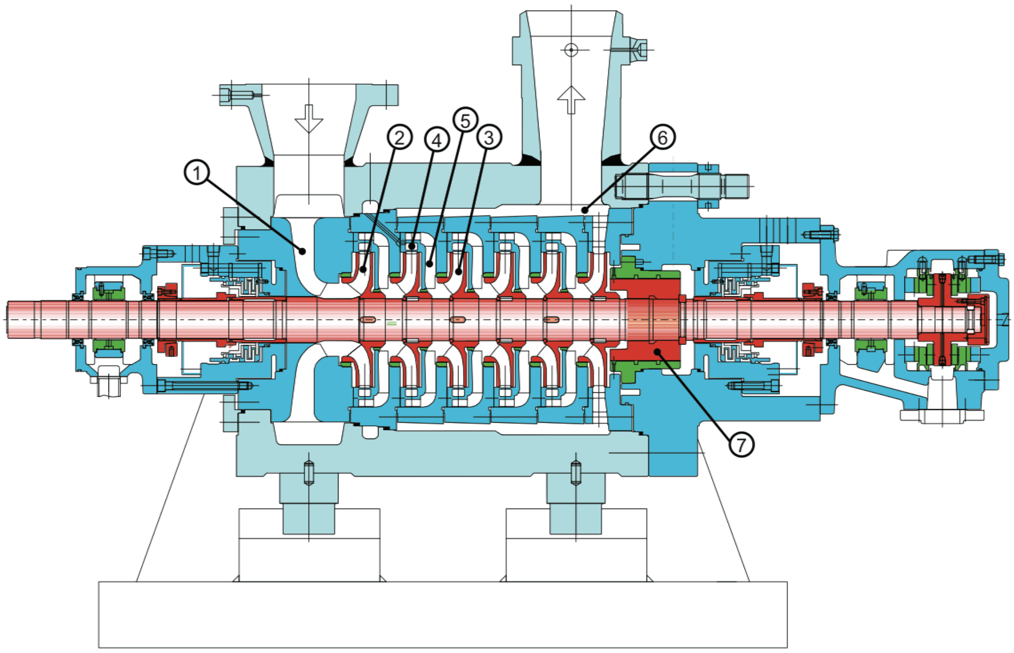

Figure 2.1: Multistage high pressure barrel pump [56]

forces being the result of the interaction of rotating and stationary pressure distributions and variations in the pressure distribution in different parts of the machine, at off-design operation additional forces appear. These forces are the result of hydrodynamic phenomena, which exclusively occur at flow rates apart from the design flow rate and include recirculation and the formation of stationary or progressing zones of flow separation.

Flow separation is inevitable during the operation of rotating machinery at off-design conditions. A vast number of research projects related to rotating flow separations, referred as rotating stall have been performed in the domain of centrifugal compressors as these phenomena have been identified as precursor to surge, which limits the operating range of centrifugal compressors. In centrifugal pumps, this limitation doesn't exist, so the definition of operating limits for centrifugal pumps is to be based on other criteria. The most strictly defined part-load limitation is the thermal minimum flow, which is limiting the temperature increase due to part-load recirculation. For high energy pumps, this lower limit is found at flow rates between 15 and 25 % of the best efficiency flow rate. This criterion is not suitable for long term operation, as the flow inside the hydraulic components is highly unsteady, three-dimensional and characterized by recirculation in the impeller and the diffuser. Therefore, the operating limits for long-term operation are rather defined based on the level of vibrations observed at different pump components, mainly the bearing housings and the pump shaft. Acceptable vibration levels are imposed by different international standards as ISO 10816-7 or API 610, a review of vibration levels and its suitability can be found in [97].

Case studies on rotating machinery internal faults, rather rarely published in open literature ([96], [105], [33], [123]) suggest, that high vibration levels of internal pump components or even mechanical failures may occur without being detected by external measurements of shaft or bearing housing vibrations, making its analysis or the definition of preventive measures difficult.

This makes the knowledge of internal pressure fluctuation and deformation levels at different operating conditions mandatory in order to assess the mechanical integrity of a centrifugal pump, especially at very high specific energy levels and at off-design conditions. Therefore, the presented experimental investigation has been undertaken to perform a thorough analysis of the most important flow regimes and its impact on mechanical deformations and vibrations at flow rates ranging from design conditions towards part-load operation within typical operational limitations for high-energy centrifugal pumps. The investigation is focussed on hydrodynamic phenomena found exclusively at part-load operation, specifically stationary and rotating stall, and its signature, found in the spatially distributed transient pressure fluctuations.

In order to obtain the necessary insight into part-load hydrodynamic phenomena and the related mechanical deformations of a high-speed pump impeller, a test pump, modeling the last stage of a high-energy multistage centrifugal pump, operating with rotational speeds as found in industrial applications has been instrumented with pressure sensors, strain gauges and accelerometers in the stationary and rotating domain. Additionally, the axial and radial shaft motion relative to the pump casing has been monitored and analyzed. While the pressure constraints did not allowed optical access to the hydraulic passages of the test pump, the pressure fluctuation, deformation and vibration data, acquired at various rotational speeds, operating points and different locations, will be used to obtain sufficient informations for the definition of mechanical load conditions for the impeller operating at different relative flow rates and rotational speeds.

2.2 Document Organisation

The performed experiments and the analysis of the obtained results are outlined in the present document in three main parts, following to this introduction, in which the operational principles and the available literature on part-load flow phenomena and mechanical excitations in centrifugal pumps have been summarized.

- In **Part I** the test case, the available measurement technology and the applied analysis methods are outlined. **Chapter 3** is dedicated to the description of the experimental facilities and the test pump, used to perform the experimental investigations. **Chapter 4** presents the instrumentation of the test pump, the different sensor types and their locations and the data acquisition systems used for the measurements performed in the stationary and rotating components of the test pump. In **Chapter 5** the analysis definitions and methods applied in the time and frequency domain are outlined.
- In **Part II** the results of the performed experiments along with analyses and conclusions are presented. In **Chapter 6** the time averaged results are presented. This includes global performance values as well as pressure distributions in different components and their consequences on the operational forces, acting on the pump impeller. **Chapter 7** is devoted to the RSI pressure fluctuations at the best efficiency point. The analysis is performed for rotating and stationary components and comprises the identification of rotating pressure waves resulting from the interaction of impeller and diffuser pressure fluctuations. **Chapter 8** presents the analysis of pressure fluctuations at part load and focalizes on the occurence of stationary and

rotating zones of flow separation. **Chapter 9** presents an analysis of the impellers mechanical response to the pressure fluctuations at design and off-design conditions, showing a significant quantitative and qualitative change in the observed impeller deformation pattern. Finally, in **Chapter 10** an analysis of axial and radial shaft vibration measurements is presented, highlighting the impact of flow separations on the rotor behaviour.

- **Part III** summarizes the presented work and suggests future directions of investigations in order to improve the operational safety of high energy centrifugal pumps.

Part I

Experimental and Analysis Tools

Chapter 3

Experimental Setup

3.1 Test Loop

The intended experiments at operating conditions, which are supposed to be as similar as possible to the operating conditions typically found in industrial applications of high energy centrifugal pumps, made the design and manufacturing of a specific test loop at the test site of SULZER Pumps necessary. The main constraints were given by the pressure levels at the pump inlet (30 bar) and outlet (100 bar), the power consumption of the pump and the requirement to perform experiments at various rotational speeds.

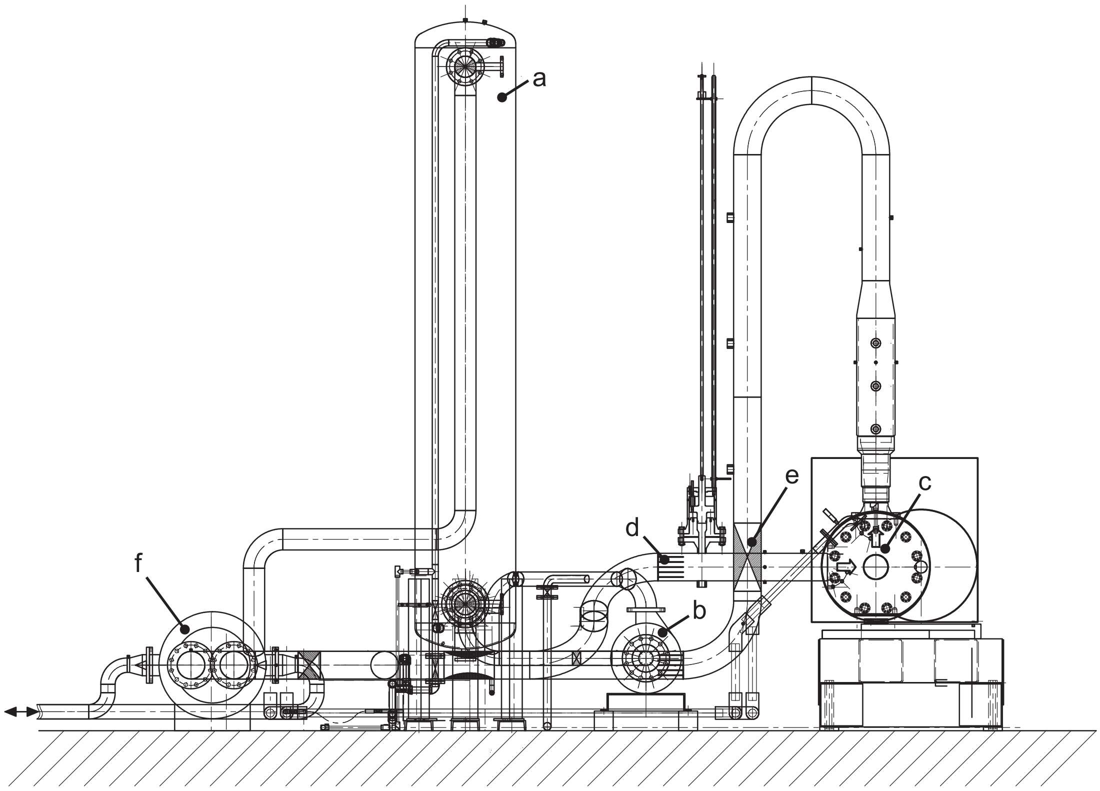

Figure 3.1: Test loop

Figure 3.1 presents the closed circuit, which has been used for the experiments. The test loop is equipped with a high pressure reservoir (a) in order to provide the necessary suction pressure for a cavitation free operation of the test pump at all tested flow rates of interest. In order to control the onset of cavitation, the test loop has been carefully degassed before performing the experiments. For the protection of the sensors during the degassing process, an auxiliary pump (b) has been installed, which has been used as a circulation pump.

The water is entering the pump (c) after passing a flow straightener (d). Downstream of the model pump, a high pressure control valve (e) is installed for the adjustment of the flow rate and to reduce the pressure to the suction pressure level. After passing another flow straightener and an inductive flow meter, the flow can be diverted into a heat exchanger (f), which is connected to an external cooling tower in order to keep the water temperature in the test loop at a constant level.

The model pump is driven by a variable speed electrical motor with a power of 1.2 MW. Between the motor and the pump, a gear is installed to increase the rotational speed to a maximum value of 6000 rpm. The main operating parameters of the test loop are summarized in Table 3.1.

$p_{s,max}$ $[bar]$	$p_{d,max}$ $[bar]$	Q_{max} $[m^3/s]$	P_{max} $[MW]$	n_{max} $[rpm]$
30	100	0.21	1.2	6000

Table 3.1: Test loop parameters

The operating conditions of the pump were controlled by the adjustment of the discharge pressure drop in the high pressure valve and the rotational speed of the pump. The operational parameters have been acquired using a designated data acquisition system provided by SULZER Pumps.

3.2 Model Pump

The experiments have been performed using a pump model, which represents the last stage of a high head multistage centrifugal pump having a specific speed of $n_q = 21.5$. Figure 3.2 depicts the sectional drawing of the pump model, Table 3.2 summarizes the hydraulic and geometrical main parameters of the model pump used for the experiments.

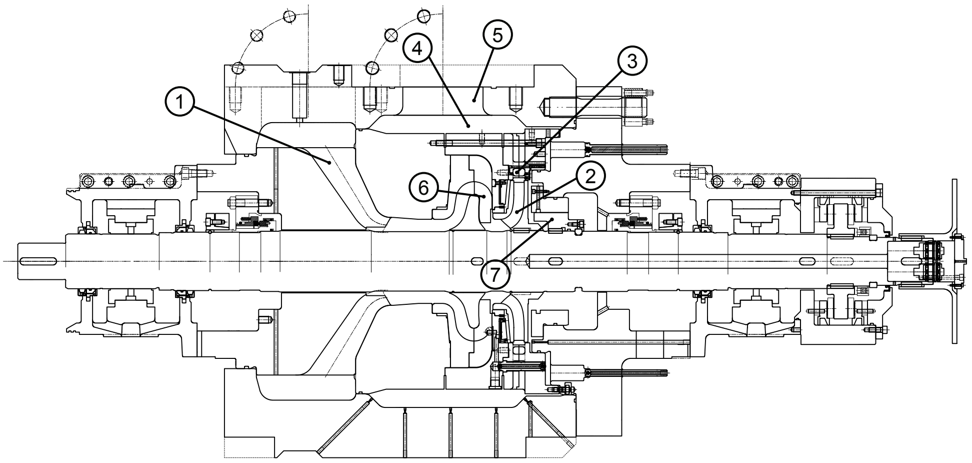

Figure 3.2: Model pump sectional drawing

Hydraulic Main Parameters				
n_{nom} $[rpm]$	Q_{nom} $[m^3/s]$	H_{nom} $[m]$	P_{nom} $[kW]$	n_q $[-]$
5000	0.198	573	1400	21.5
Impeller geometry				
D_2 $[mm]$	D_1 $[mm]$	b_2 $[mm]$	β_2 $[°]$	z_B $[-]$
346	184.4	22.7	25	7
Diffuser geometry				
D_3 $[mm]$	D_4 $[mm]$	b_3 $[mm]$	b_4 $[mm]$	z_V $[-]$
366.2	550	26.3	26.3	12

Table 3.2: Test pump hydraulic main parameters

The pump model consists of an inlet casing (1), the impeller (2), equipped with seven blades and the vaned diffuser (3), having twelve vanes, followed by an annular ring (4) guiding the flow to the discharge pipe (5). The relative radial gap between the impeller trailing edge and the diffuser leading edge was 5.8%. Between the inlet casing and the impeller, a return section has been placed in order to simulate the inlet conditions of the last stage of a multistage pump (6). This return section consists of nine guide vanes, pointing radially inwards in order to ensure an axial inflow into the impeller eye. The axial thrust is reduced using a balance piston (7), the balance flow is guided back into the suction casing.

The pump shaft is equipped with a long bore from the impeller seat to the shaft non-drive end. This bore is used to pass the cables from the sensors, embedded in the impeller to two LEMO connectors, integrated in the shaft end, which are used to establish a proper electrical connection between the embedded sensors and the onboard data acquisition system.

Chapter 4

Instrumentation

4.1 Transient Pressure Measurements

4.1.1 Piezoresistive Pressure Transducers

The utilized dynamic pressure sensors were specifically designed piezo-resistive miniature pressure transducers made by UNISENSOR AG. These sensors are capable to measure both, unsteady and steady static pressure applied to the sensor surface. They consist of piezo-resistive gauges arranged in a Wheatstone bridge under a silicone membrane having a diameter of 3 mm. The pressure sensors have been integrated in specific housings which have been glued in the prepared positions in the impeller and the diffuser. After the sensor embedding, the cables were passed through grooves to a central bore in the shaft leading to the the non-drive end of the pump, where they are connected to two rugged circular connectors having a total of 96 contacts. The cable grooves have been covered with a ceramic composite in order to protect the sensors back face and cables from ingress of moisture (see Figure 4.1).

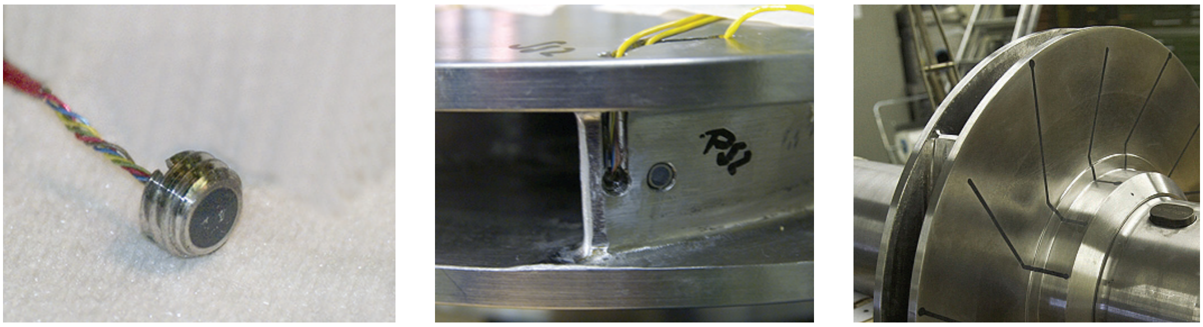

Figure 4.1: Pressure sensor and cable passage in the impeller

4.1.2 Sensor Calibration

Prior to the installation in the impeller and the stationary pump components, the pressure sensors have been statically calibrated in a specific test stand (Figure 4.2). During the calibration process, the pressure has been gradually increased to 100 bar and then reduced to 0 bar. The reference pressure has been measured with a high precision reference pressure transducer.

The linear relation between the applied pressure p_{cal} and the measured voltage is expressed by

$$p_{cal} = a \cdot U + b \tag{4.1}$$

The slope a and the intersection b are estimated with a linear regression scheme, where

$$a = \bar{p}_{cal} - b \cdot \bar{U} \tag{4.2}$$

and

$$b = \frac{\sum\limits_{i=1}^{n} \left(U_i - \bar{U}\right)\left(p_{cal,i} - \bar{p}_{cal}\right)}{\sum\limits_{i=1}^{n} \left(U_i - \bar{U}\right)^2} \tag{4.3}$$

with

$$\bar{p}_{cal} = \frac{1}{n}\sum_{i=1}^{n} p_{cal,i} \qquad \text{and} \qquad \bar{U} = \frac{1}{n}\sum_{i=1}^{n} U_i \tag{4.4}$$

The error is calculated using

$$\epsilon = \frac{p_{ref} - p_{cal}}{p_{ref,max} - p_{ref,min}} \tag{4.5}$$

The maximum error of the static pressure was estimated to be less than 1% of the measurement range of the pressure sensor. For the sensors, mounted in the impeller blade suction and pressure surface close to the trailing edge, the influence of the rotation has

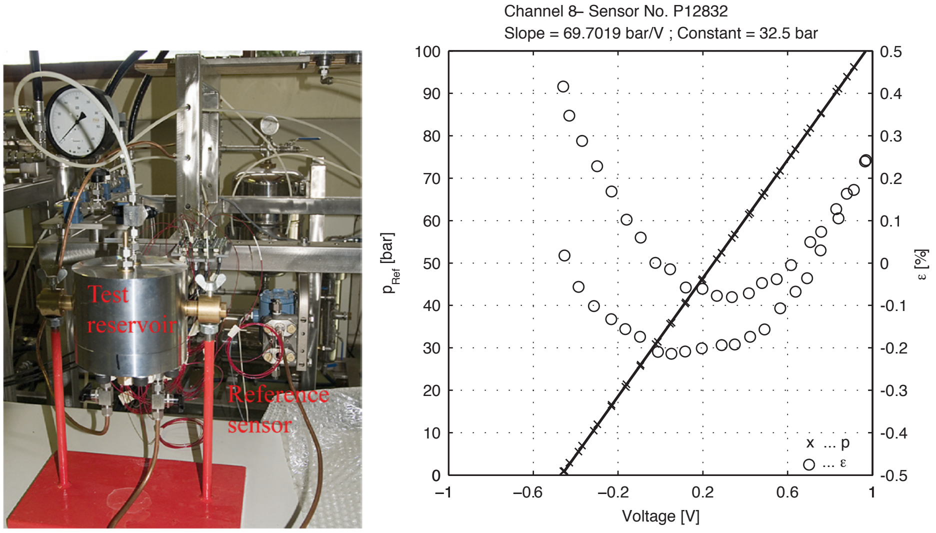

Figure 4.2: Sensor calibration test stand and typical calibration curve

been analytically evaluated and found to be less than 0.2% of the expected pressure levels. The static calibration has been repeated on site with the sensors embedded in their final position in order to verify the influence of the sensor mounting on their behavior. The calibration curves obtained in situ showed good agreement with the original calibration. The piezo-resistive pressure sensors used for the experiments show a drift of their offsets. This drift has been corrected prior to each test by re-estimating the offset of each sensor with the help of a reference pressure sensor. The dynamic response of this sensor type has been validated with a sensor identical in construction ([39],[102]. The frequency response to different kinds of excitations expressed an excellent coherence between 0 and 25 kHz.

4.2 Strain Gauges

Strain gauges are used to measure deformations by the change of its resistance. Deformation of the strain gauge and its resistance change are proportional to each other

$$\frac{\Delta R}{R} = \frac{\Delta L}{L} = \epsilon \tag{4.6}$$

Hookes law relates deformation directly to stress

$$\sigma = \epsilon \cdot E \tag{4.7}$$

The change in resistance is measured using a Wheatstone bridge having one active element (the strain gauge) arranged in a so-called quarter bridge. No temperature compensation has been foreseen, as the temperature variation during the experiments is limited by a cooling system for the test loop water. The wiring (see Fig. 4.3) is optimized in order to reduce the influence of cable losses, for further details see [66]. The measured output voltage is related to the deformation applied to the strain gauge through

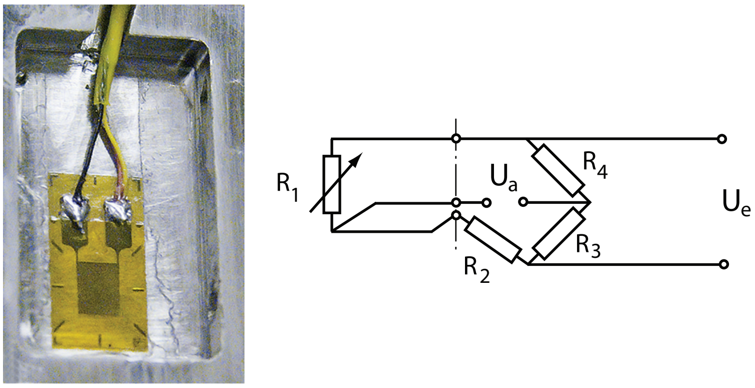

Figure 4.3: Wheatstone bridge for strain measurements

$$\epsilon = \frac{4}{k}\frac{U_a}{U_e} \tag{4.8}$$

Since an in-situ calibration of the strain gauges was not possible, the strain gauge factor k provided by the strain gauge manufacturer has been used (k=2.04) to evaluate the deformation values.

4.3 Accelerometers

The impeller vibrations have been measured using piezoelectric miniature accelerometers, embedded in the impeller shroud.

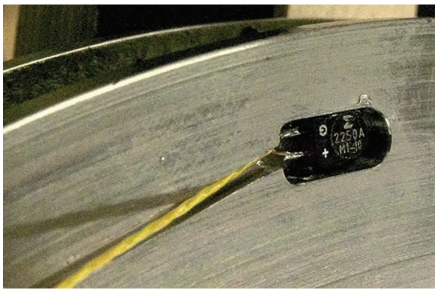

Figure 4.4: Embedded accelerometer

Piezoelectric accelerometers consist of a weight and piezoelectric element. When an acceleration is applied, the resulting force deforms the piezoelectric elements, generating an electric charge. The used embedded accelerometers (Endevco 2250 AM-1) are capable to measure accelerations within a range of ±500 g at frequencies between 2 Hz and 15000 Hz.

4.4 Proximity Sensors

The relative motion between shaft and pump casing is measured using eddy current proximity sensors. The measurement principle is based on electromagnetic induction and reaction. According to Faradays induction law, an induced eddy current flows in an electrical metal conductor, if the conductor is located in a time changeable magnetic field. The magnetic field is generated by an alternating current flowing in a wire coil. The eddy current generates an opposite magnetic field, which superimposes the exciting magnetic field and consequently, the impedance of the sensor coil changes. The used proximity sensors (Bently Nevada 3300 XL) are calibrated using a target of the same material as the shaft. The output is a voltage, proportional to the shaft distance, the error is typically less than 5%.

4.5 Data Acquisition

4.5.1 Stationary Domain Data Acquisition

The stationary domain pressure fluctuation data, the shaft vibrations and the reference signal for shaft angular position and rotational speed have been acquired using a VXI (VME Extensions for Instrumentation) HP1432A data acquisition system. With this modular 48-channel data acquisition system it it possible to acquire transient voltage data with sampling frequencies up to 51.2 kHz and a resolution of 16 bit. The memory is sufficient to store 1'048'576 samples per channel. The system is equipped with appropriate pre-amplifiers and anti-aliasing filters.

The data acquisition control and storage is achieved by a software system, based on NI-Labview data acquisition toolboxes, running on a personal computer.

4.5.2 Rotating Domain Data Acquisition

Based on available experiences at the EPFL-LMH ([10],[38]), a new onboard conditioning and data acquisition system has been developed in close collaboration with the EPFL-LEG in order to perform pressure fluctuation, strain and acceleration measurements at high rotational speeds. To fulfill this requirement, it was necessary to miniaturize and optimize the mechanical components, as well as the electronic devices being part of the onboard data acquisition system. The new onboard system consists of 32 measurement channels mounted on 4 circular multilayer boards. The positioning of the electronical components has been optimized to account for the high mechanical load due to the centrifugal forces at the intended rotational speeds. The onboard data acquisition system is capable to acquire voltage data with sampling frequencies up to 100 kHz. The resolution of the digitalization is 12 bit. The memory of the onboard system allows the storage of 450'000 samples for each of the 32 channels.

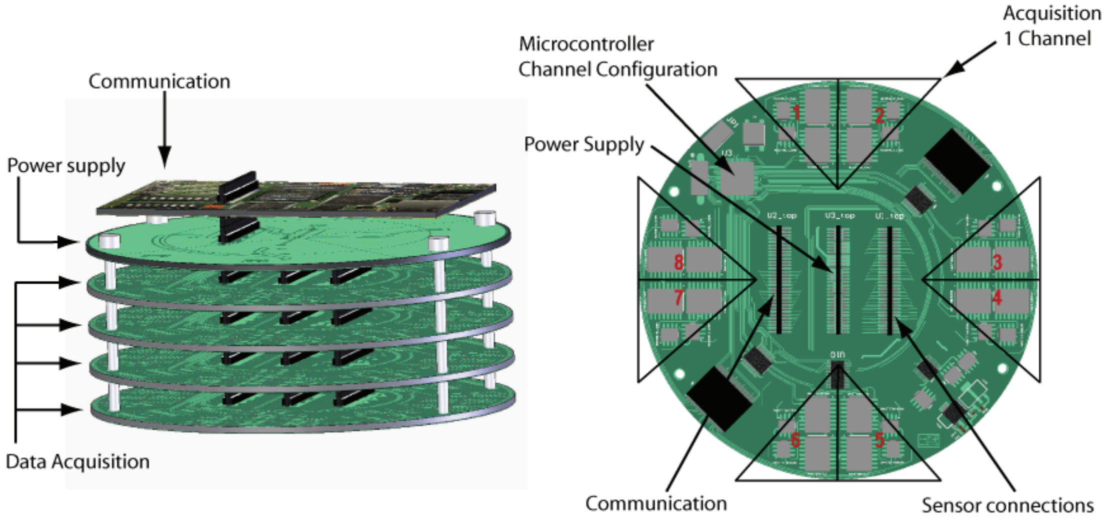

Figure 4.5: Data acquisition system for rotating domain measurements

The conditioning electronics, consisting of preamplifiers, anti aliasing filters and a second amplifier are also integrated on the acquisition boards. The amplification factors can be selected between 10 and 800. Software controllable offsets before the preamplifiers and after the anti aliasing filters allow the centering of the signal for an optimal use of the digitalization range.

Eight channels were specifically adapted for the acquisition of the strain gauge data, 4 channels were modified to perform the conditioning and acquisition of accelerometer data.

The control and communication is performed with a FPGA card using the USB2 protocol, ensuring a reliable high speed communication between the host computer and the onboard data acquisition system. Power supply, communication with the computer controlling the measurements and external triggering has been realized using a high speed slip ring.

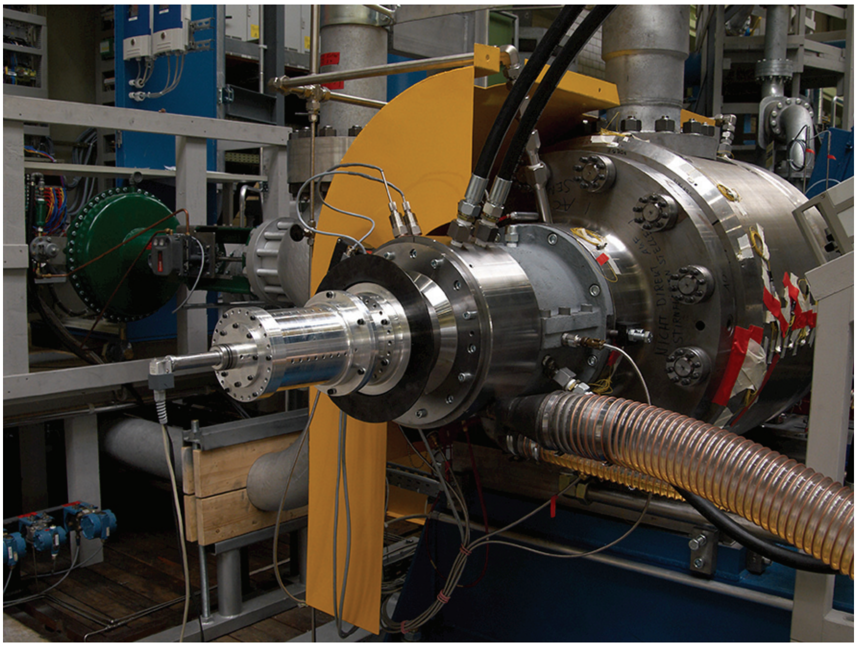

Figure 4.6: Onboard data acquisition system installed at pump shaft

The onboard data acquisition system has been mounted into a cylindrical casing made of aluminum in order to reduce the system mass. After precision balancing of the whole data acquisition system, it has been fixed overhung on the non-drive end of the pump shaft. The influence of the additional mass on the shaft end on the rotodynamic behavior of the pump has been validated during the design process at SULZER Pumps. During the experiments, a protection cover has been installed around the rotating data acquisition system.

The data acquisition control and storage is achieved by a newly developed software system, based on NI-Labview data acquisition toolboxes, featuring the same functionality and using the same binary data storage format, as the already available data acquisition software used in the stationary domain.

4.5.3 Synchronisation and Final Data Archiving

The data in the stationary and in the rotating domain have been acquired synchronously by simultaneous triggering of both data acquisition systems using the keyphasor signal.

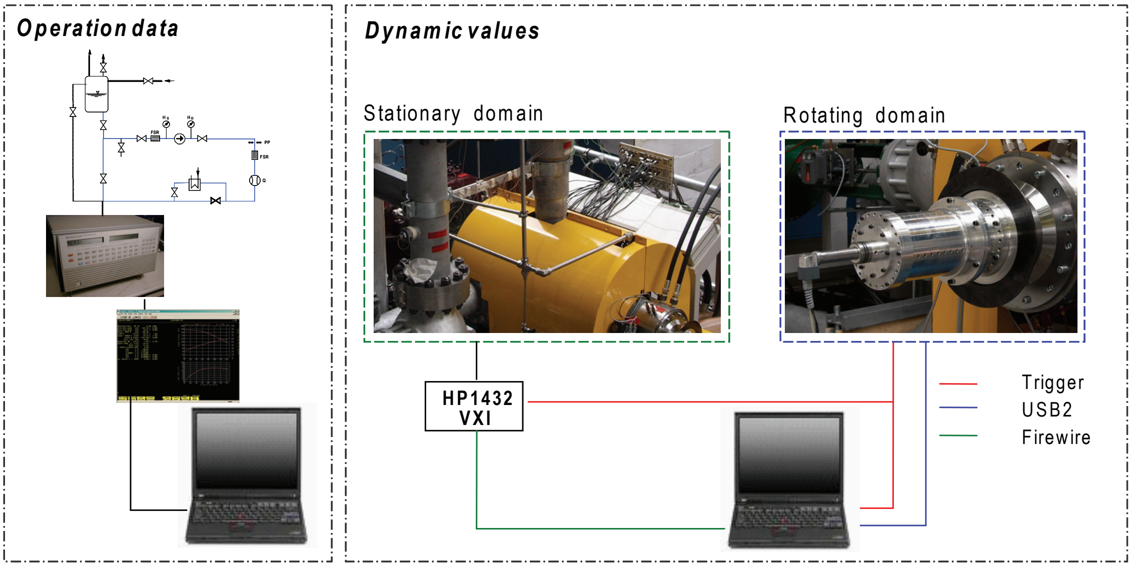
Operation data
Dynamic values
Stationary domain
Rotating domain
HP1432
VXI
Trigger
USB2
Firewire

Figure 4.7: Schema of data acquisition

After finishing the experiments, the acquired rotating and stationary domain data for each measurement point have been archived in a single file, using a common file format (HDF5, Hierarchical Data Format), intended for the storage and organization of large amounts of numerical data.

4.5.4 Angular Reference and Rotational Speed

Figure 4.8 depicts the determination of the angular reference. The impeller angular position is determined using an eddy current proximity probe (a). At a defined angular position the shaft is equipped with a bore (b).

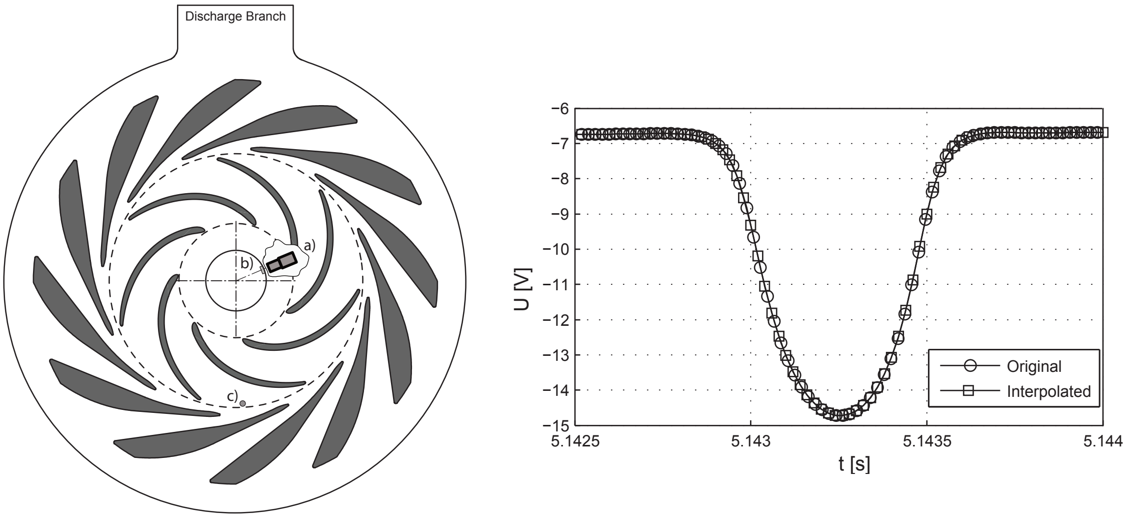

Figure 4.8: Angular reference position determination

Each time, the bore passes the stationary pickup, the measured output voltage of the eddy current sensor is significantly reduced. The impeller rotation start is defined as the location of the minimum voltage per revolution, which occurs, when the bore center passes the proximity sensor. With the known position of the reference pressure sensor (c), the obtained signals can be related to the relative position of impeller and diffuser. The keyphasor signal is registered only in the stationary data acquisition system. The sampling frequencies in both data acquisition systems were usually different, therefore the trigger position for the rotating domain has been re-estimated by linear interpolation in the time domain.

4.6 Sensor Locations

4.6.1 Embedded Sensors in the Rotating Domain

The impeller has been equipped with 17 pressure sensors. Each impeller channel outlet has been instrumented with pressure sensors in the hub between 2 blades (BRSI). Two impeller channels were instrumented with pressure sensors in the hub at impeller inlet (BCH1, BCH3), in the channel between inlet and outlet (BCH2, BCH4) and in the shroud at the impeller inlet (BCS1, BCS2). Two consecutive impeller blades were instrumented in the blade surface close to the trailing edge (BLPS1, BLPS2), one was instrumented in the impeller suction surface close to the trailing edge (BLSS2). Figure 4.9 presents the impeller pressure sensor locations. The pressure sensor cables were passed through a hollow shaft to the non-drive end of the pump, where the onboard data acquisition system processed the data and transferred them to the stationary domain. Additionally to the pressure sensors, 8 strain gauges (SG1 to SG8) and 3 piezoelectric accelerometers (Acc1 to Acc3) have been installed in the impeller. The sensor locations are presented in Figure 4.9.

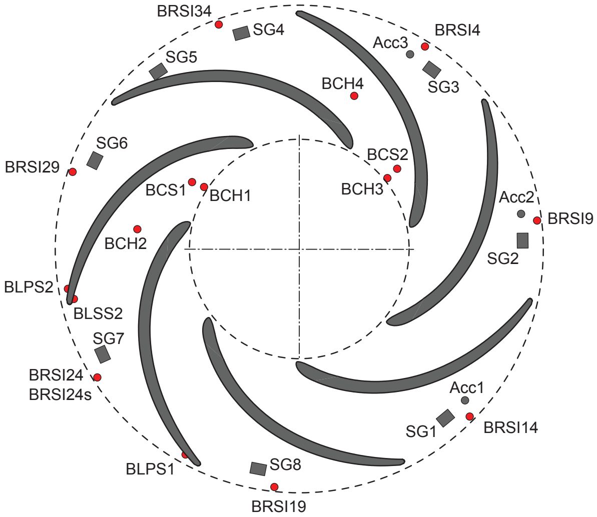
BRSI34
SG4
SG5
Acc3
BRSI4
BCH4
SG3
SG6
BRSI29
BCS2
BCS1
BCH1
BCH3
Acc2
BRSI9
BCH2
SG2
BLPS2
BLSS2
SG7
BRSI24
BRSI24s
Acc1
SG1
BRSI14
BLPS1
SG8
BRSI19

Figure 4.9: Pressure sensors embedded in impeller

4.6.2 Pressure Sensors in the Stationary Domain

The stationary domain has been equipped with 64 flush mounted pressure sensors distributed in the different stationary main components of the model pump stage.

The diffuser has been equipped with pressure sensors in each diffuser throat (VTC) and each diffuser outlet (VOC). Additionally, 2 channels were equipped with pressure sensors in the channel at a position half of the channel length (VCD) and one pressure sensor was installed close to the rotor stator interface (VRSI). The impeller side room at hub (RSRHUB) has been equipped with 6 pressure sensors at a diameter of 354 mm (which is equal the center diameter of the gap between the impeller side walls and the diffuser side walls). The shroud side room was instrumented with 6 sensors at a diameter of 344 mm. Design constrains did not allow to distribute the sensors at the same diameter as the sensors at the impeller hub side room. The hub and the shroud side room pressure sensors are located at the same angular positions. Two pressure sensors are located in the shroud side room at a diameter of 260 mm, rotated by 90 degrees. The annular exit chamber has been instrumented with 14 pressure sensors at the pumps non-drive end (SCR), at the position of the sensors SCR8 and SCR11, pressure sensors are also installed at the pump drive end. 3 pressure sensors were axially distributed in the annular chamber along the angular position of the pressure sensor SCR8. Figure 4.10 outlines the different sensor positions in the stationary domain.

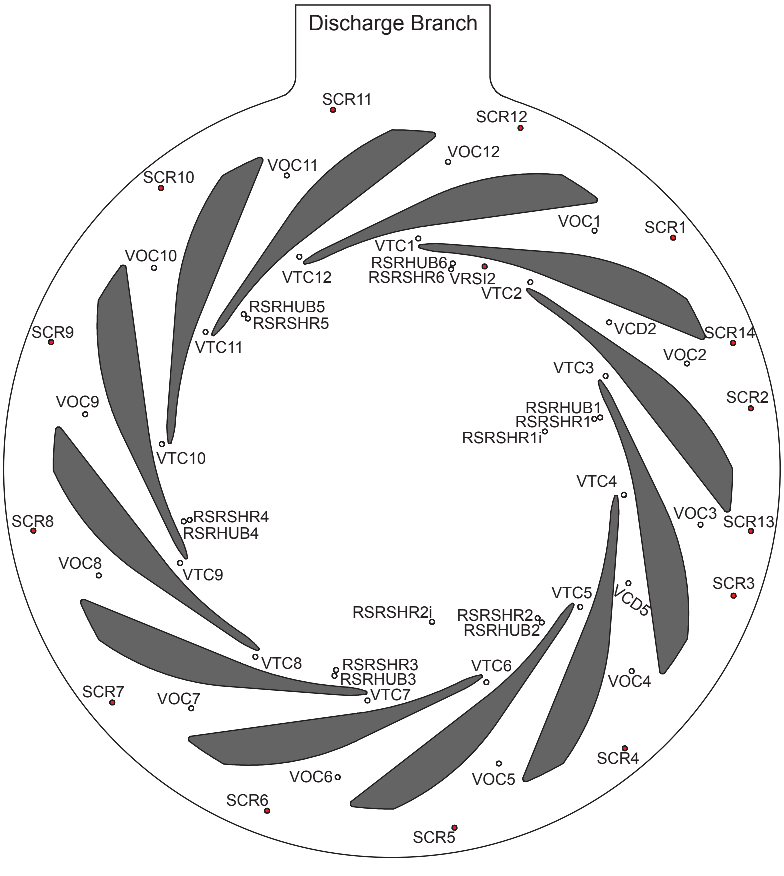
Discharge Branch
SCR11
SCR12
VOC12
VOC11
SCR10
VOC1
SCR1
VTC1
RSRHUB6
RSRSHR6
VRSI2
VTC2
VTC12
VOC10
RSRHUB5
RSRSHR5
VTC11
SCR9
VCD2
SCR14
VOC2
VTC3
SCR2
VOC9
RSRHUB1
RSRSHR1
RSRSHR1i
VTC10
VTC4
VOC3
SCR13
SCR8
RSRSHR4
RSRHUB4
VOC8
VTC9
SCR3
VTC5
VCD5
RSRSHR2i
RSRSHR2
RSRHUB2
VTC8
RSRSHR3
RSRHUB3
VTC7
VTC6
VOC4
SCR7
VOC7
VOC6
VOC5
SCR4
SCR6
SCR5

Figure 4.10: Pressure sensors embedded in the diffuser, side rooms and annular exit chamber

4.6.3 External Pressure Sensors

The suction pipe and the discharge pipe have been equipped with piezoelectric pressure sensors of the type Kistler 701. This type of pressure sensors is capable of measuring only transient pressures. Fig 4.11 depicts the locations and designations of the external dynamic pressure sensors. The test loop parameters have been measured using Rosemount transducers. The data have been acquired separately by a data acquisition system provided by Sulzer Pumps.

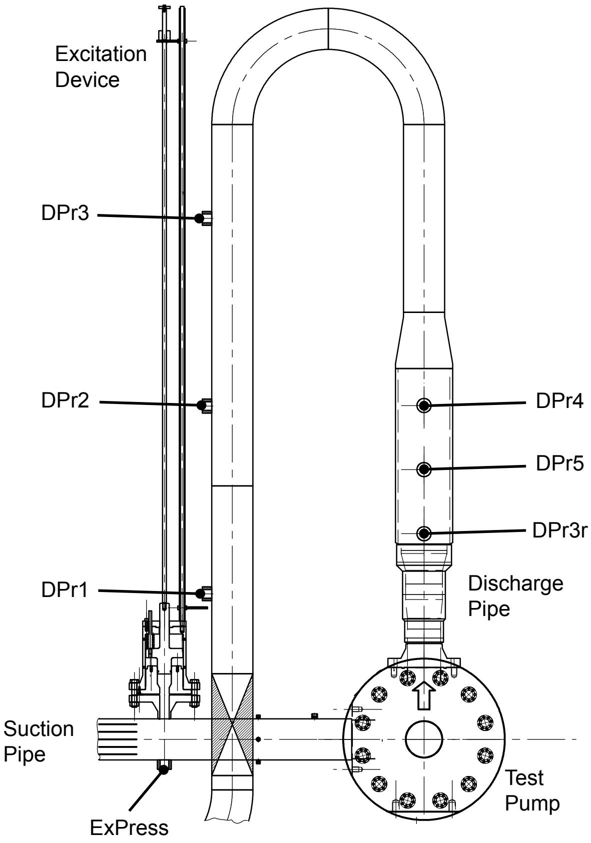
Excitation Device
DPr3
DPr2
DPr1
DPr4
DPr5
DPr3r
Discharge Pipe
Suction Pipe
ExPress
Test Pump

Figure 4.11: External pressure sensor locations

4.6.4 Eddy Current Shaft Proximity Probes

Figure 4.12 shows the axis definition of the radial proximity sensor coordinates. The radial proximity sensors are arranged under an angle of 90°, which allows the reconstruction of the shaft orbits.

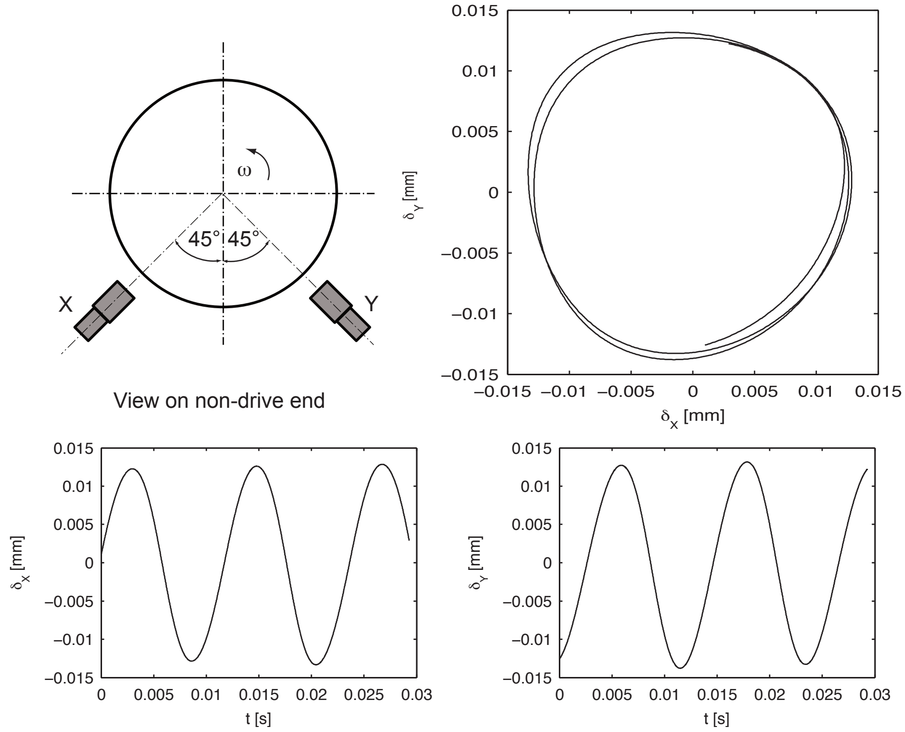

Figure 4.12: Coordinate system definition for radial proximity probes

The axial shaft movements are measured using a proximity sensor and a disk mounted on the casing of the onboard data acqusisition system. The positive z-axis is defined in the direction of the non drive end, thus pointing into the impeller eye (see Figure 4.13).

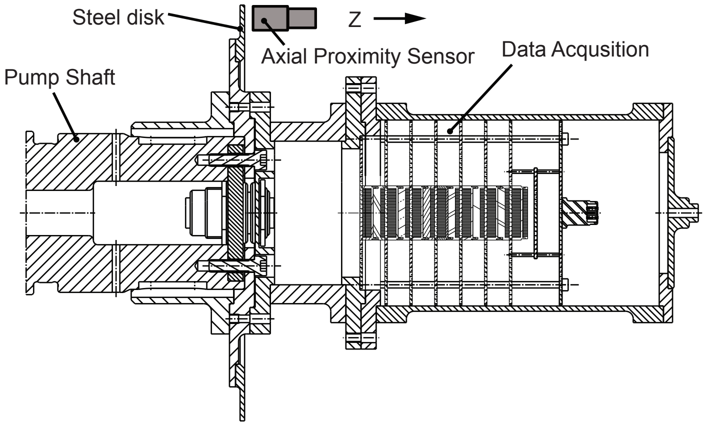

Figure 4.13: Coordinate system definition for axial proximity probe

Chapter 5

Analysis Definitions and Methods

5.1 Time Domain Definitions

5.1.1 Mean Value and Normalization

The mean value $\bar{x}$ of a quantity $x(t)$ is the time average of the quantity for an appropriate averaging time T

$$\bar{x} = \lim_{T\to\infty} \frac{1}{T} \int_0^T x(t)dt \tag{5.1}$$

For discrete pressure values and a sufficiently large number of samples, the mean value gets

$$\overline{p} = \frac{1}{N} \sum_{i=1}^{N} p(i) \tag{5.2}$$

In rotating machinery, usually a normalization of the obtained pressure values based on the dynamic pressure in the impeller outlet $(\rho \frac{u_2^2}{2})$ is performed:

$$c_{\tilde{p}} = 2 \cdot \frac{p - \overline{p}}{\rho \cdot u_2^2} \tag{5.3}$$

Geometrical similarity provided, these normalized values would be independent of rotational speed and impeller diameter.

5.1.2 RMS Value

The RMS-value of a quantity $x(t)$ is defined as

$$x_{RMS} = \sqrt{\lim_{T\to\infty} \frac{1}{T} \int\limits_0^T x^2(t)dt} \tag{5.4}$$

and with discrete pressure values the RMS value gets

$$p_{RMS} = \sqrt{\frac{1}{N} \sum_{i=1}^{N} p^2(i)} \tag{5.5}$$

5.1.3 Phase Averaging

The measured signal consists of three components:

1. a steady-state average
2. periodically fluctuating components
3. random noise

Gostelow [49] proposed the so called "phase-lock average" in order to seperate the ergodic random signal from the periodically fluctuating one. The phase average permits the reduction of noise. The phase average is defined as

$$\bar{p}(t) = \lim_{k \to \infty} \frac{1}{K} \sum_{k=1}^{K} p(t + kT) \tag{5.6}$$

The obtained signal is split in a number of n_d intervals (where the interval length defines the lowest frequency remaining in the averaged signal). Ideally each interval contains the same number of samples m. Phase averaging is acting as an ideal comb filter [86] which eliminates all frequencies except the averaging base frequency (given by the interval length) and its harmonics.

5.2 Frequency Domain Methods and Definitions

5.2.1 Sampling Frequency and Filtering

The sampling frequency should fit the frequency range of interest in a way, that Shannons sampling theorem [116] is not violated. This theorem states, that a function $f(x)$, which contains no frequencies higher then ω_{max}, is determined completely, when its ordinates are given at a series of points with a distance $T = \pi/\omega_{max}$. This theorem is applicable only for bandwidth limited signals (finite maximum frequency), for real applications, the maximum frequency of the signal will be filtered at the upper frequency of interest and the signal will be sampled with sampling frequencies above twice the filter cut-off frequency. If no filtering is done, or the sampling frequency is too low, aliasing would occur, pretending peaks in the frequency domain, which are not real. For some analyses it is useful to filter the acquired signal further. This filtering is done in this work using a numerical 5th order Butterworth filter.

5.2.2 Fourier Transform

Definition

The Fourier transform X(f) of a quantity x(t) is a complex-valued function defined as

$$X(f) = \int_{-\infty}^{\infty} x(t) e^{-i2\pi f t} dt \qquad -\infty < f < \infty \tag{5.7}$$

Measured quantities have always a finite length, therefore the finite Fourier transform is calculated as

$$X(f, T) = \int_{0}^{T} x(t) e^{-i2\pi f t} dt \tag{5.8}$$

Since the measured quantity is acquired as a series of discrete samples, the discrete Fourier transform (DFT) is applied:

$$X(f,T) = \Delta t \sum_{n=0}^{N-1} x_n e^{-i2\pi f n \Delta t} \tag{5.9}$$

The discrete Fourier transform is calculated using the Fast Fourier Transform proposed first by Cooley and Tukey [25].

Spectral Leakage

One of the basic assumptions of the FFT is the presence of a periodic signal captured in the sample. If start and endpoint of the sample don't match - which is always the case for a real signal containing stochastic components - the FFT leads to aliases, falsifying the obtained spectrum. In order to avoid this effect, the data in the time domain are multiplied with a so-called window function, being 0 at the sample boundary and 1 in the middle of the interval. Although various window functions exist, one of the oldest and still most commonly used window function in engineering practice is the Hanning window ("von Hann" window), defined by the function

$$w(t) = \frac{1}{2} \cdot \left(1 - \cos\left(\frac{2\pi t}{T}\right)\right) \qquad \text{with} \qquad 0 \leq t \leq T \tag{5.10}$$

The use of the Hanning window is introducing some error to the sample by suppressing the signal close to its beginning and end. This is compensated by a statistically estimated correction factor of $\sqrt{\frac{8}{3}}$.

Averaging

A significant improvement of the estimated spectra can be obtained by an averaging of several single spectra. The total data set is split in a number of blocks having a constant length. The amplitude spectrum for each block is calculated and finally the average of all blocks is calculated.

5.2.3 2D FFT

If $x(t;s)$ is a function of two discrete variables such as time t and length, s, the 2D analysis formula could be expressed as multiplication of two separate functions in two dimensions, time t and length s.

$$X(f;g) = X(f) \cdot Y(g) = \int_{-\infty}^{\infty} x(t)e^{-j2\pi ft}dt \cdot \int_{-\infty}^{\infty} y(s)e^{-j2\pi gs}ds \tag{5.11}$$

Thereby, 2D Fourier transform is written as a 1D transformation in t direction followed by a 1D transformation in the s direction.

$$X(f;g) = \int_{-\infty}^{\infty} \left\{ \int_{-\infty}^{\infty} x(t,s)e^{-j2\pi ft}dt \right\} e^{-j2\pi fgs}ds \tag{5.12}$$

$$X(f;g) = \int_{-\infty}^{\infty} \int_{-\infty}^{\infty} x(t,s)e^{-j2\pi(ft+gs)}dtds \tag{5.13}$$

Working with the Fourier transform usually involves the discrete Fourier transform (DFT). A discrete transform is a transform, whose input and output values are discrete samples, making it convenient for computer manipulation. The DFT is usually defined for a discrete function that is nonzero only over the finite region. The two-dimensional M-by-N DFT and relationship is given by:

$$X(f;g) = \sum_{m=1}^{M} \sum_{n=1}^{N} x(t,s)e^{-j2\pi\left(\frac{mt}{M}+\frac{ns}{N}\right)} \tag{5.14}$$

and its inverse is given by

$$x(t;s) = \frac{1}{MN} \sum_{t=1}^{M} \sum_{s=1}^{N} X(f,g)e^{-j2\pi\left(\frac{mt}{M}+\frac{ns}{N}\right)} \tag{5.15}$$

The 2D-FFT is decomposing the signals into a sum of waves of a given frequency and an associated wave number k. This allows the identification of rotor-stator interaction modes as well as other irregular phenomena.

5.3 Important Parameters of Single-Input / Output Relationships

5.3.1 Correlation

The cross-correlation function of two quantities $x(t)$ and $y(t)$ is the defined as

$$R_{xy}(\tau) = \frac{1}{T}\int_0^T x(t)y(t+\tau)dt \tag{5.16}$$

and allows the identification of time delays or phase differences between periodic and non-periodic events. A special case is given, when a signal is multiplied by a shifted version of itself, this is called autocorrelation

$$R_{xx}(\tau) = \frac{1}{T}\int_0^T x(t)x(t+\tau)dt \tag{5.17}$$

which allows the identification of periodicities in a signal.

Fourier transformation of the cross- and autocorrelation yields the cross- and auto-spectral density functions.

5.3.2 Coherence

Coherence can be interpreted as a measure of a linear relation between an input signal $x(t)$ and an output signal $y(t)$. The coherence is calculated using the relation

$$\gamma^2_{xy}(f) = \frac{|\overline{S_{xy}}(f)|^2}{\overline{S_{xx}}(f)\overline{S_{yy}}(f)} \tag{5.18}$$

The coherence is one for a constant-parameter linear system with a clearly defined input and output and it is zero for two non-related signals. For real signals, coherence can be smaller than one due to one or all of the following reasons

- Noise present in the measurement
- Relation between $x(t)$ and $y(t)$ is not linear
- $y(t)$ is related to $x(t)$ and other inputs

The coherence provides a mean to identify direct relations between pressure excitation and vibration response.

5.4 Instantaneous Phase Based Signal Processing

In the absence of a dedicated angular reference signal with very high precision, the calculation of phase averages may yield inaccurate or completely misleading results ([77], [50]).

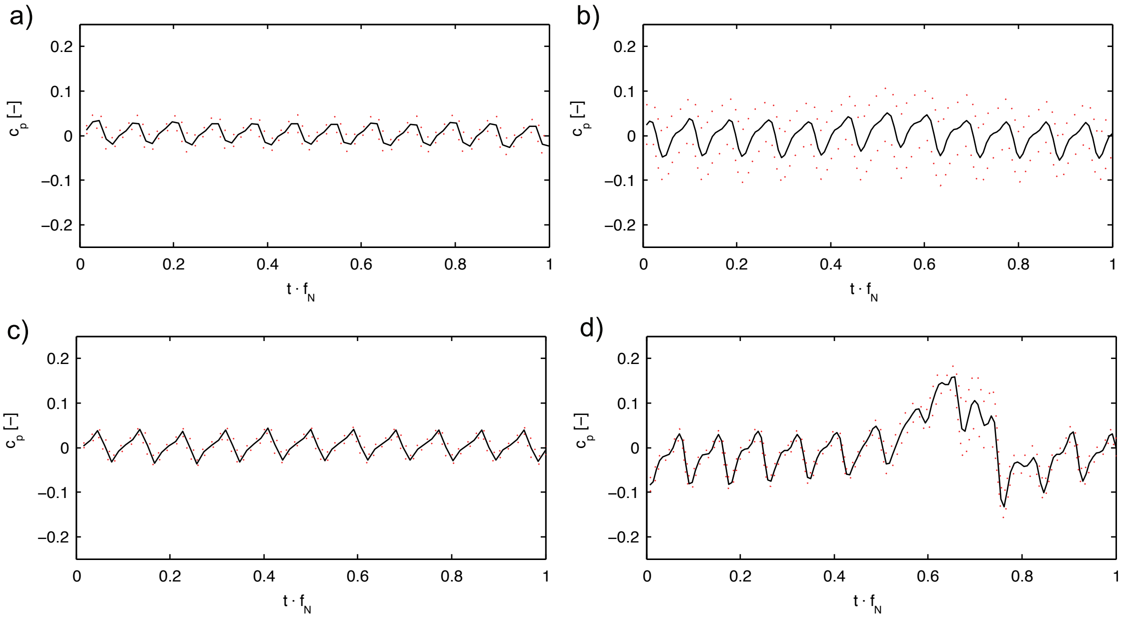

Figure 5.1: Phase averaged pressure fluctuations without and with sub-synchronous signal component

Figure 5.1 illustrates the problem arising from an improper angular reference: in Figure 5.1a a small deviation of the resampled angular reference signal yields an increased standard deviation for the phase averaged signal. Figure 5.1b depicts the situation in the presence of a strong component non-synchronous to the rotational speed. This part of the signal gets completely lost and the standard deviation drastically increases. Figure 5.1c and Figure 5.1d show the corrected phase averages for both cases. The instantaneous phase of an analytic signal (Figure 5.2b), calculated from a band-pass filtered auto-correlation of a signal $\tilde{p}_{BP}(t)$ (Figure 5.2a) as

$$P(t) = \tilde{p}_{BP}(t) + i\mathcal{H}(\tilde{p}_{BP}(t)) \tag{5.19}$$

can be obtained from

$$\phi(t) = arg(P(t)) \tag{5.20}$$

The amplitude is

$$a(t) = abs(P(t)) \tag{5.21}$$

The instantaneous phase takes values between $-\pi$ and π, the angular reference point is defined at $\phi(t) = 0$.

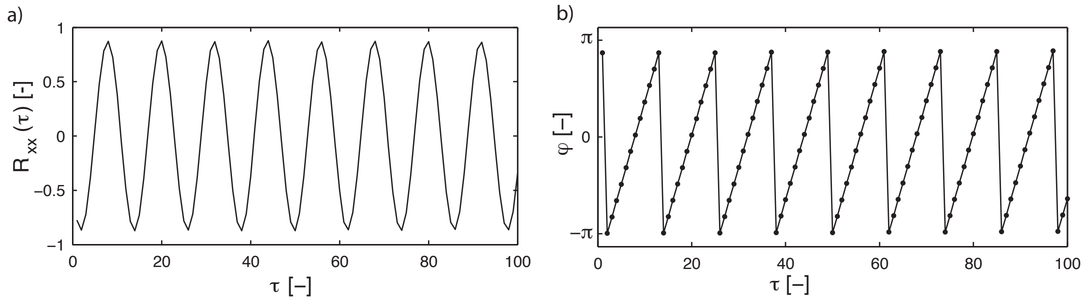

Figure 5.2: Analytic signal and instantaneous phase for pressure fluctuation signal obtained in rotationg domain

The main periodicities in the signal can be detected by the autocorrelation R_{XX}. The auto-spectrum can be used to select the base frequency of the angular reference detection algorithm. For the pressure fluctuations at design conditions, this would be the vane respectively blade passing frequency. After performing band-pass filtering in order to eliminate all other frequencies in the signal, the angular reference points are estimated using eq. 5.19 and the signal is rearranged according to the expected temporary distribution. In the next step, the result is improved by shifting the rearranged ensembles in order to maximize the cross-correlation between the first (reference) revolution and the actual revolution.

Part II

Results and Analysis

Chapter 6

Observed Pressure Pulsations and Global Performance Values

6.1 Global Performance and Associated Pressure Pulsation Patterns

The experiments have been performed at relative flow rates between q* = 0.6 ... 1.25 and at rotational speeds between 1500 and 5300 rpm. This range represents a fair approximation of the typical operational scope of high energy centrifugal pumps. Figure 6.2 depicts the measured performance curve and Figure .. the observed pressure fluctuation patterns in the impeller blade trailing edge pressure surface for different operating conditions.

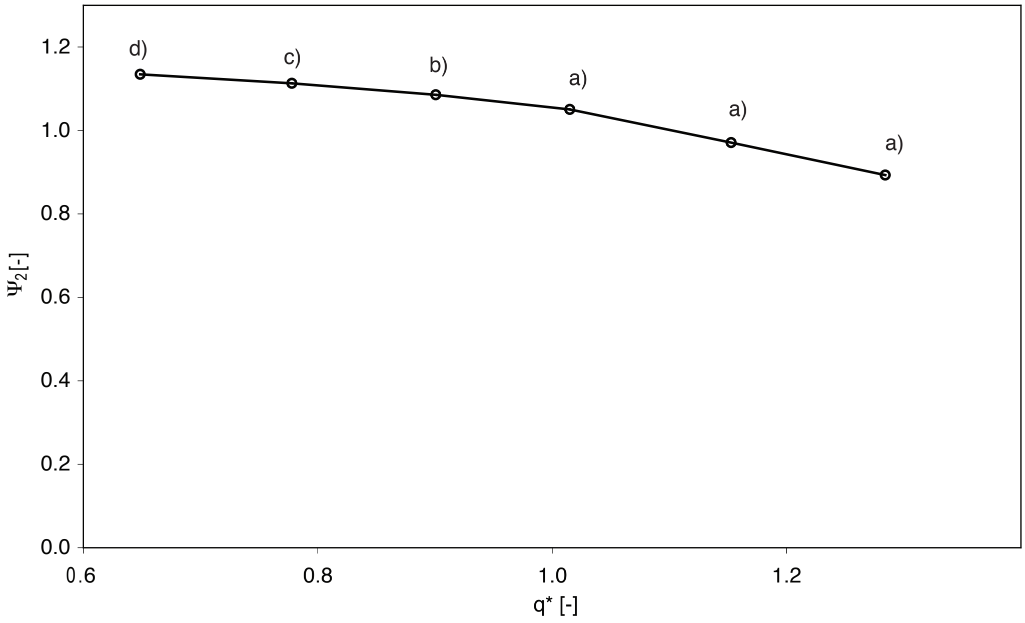

Figure 6.1: Performance cure and analyzed operating points

The global performance curve, acquired using pressure transducers in the suction pipe and discharge pipe did not exhibit an unstable behavior within the analyzed flow range but a steadily rising curve from overload to part load.

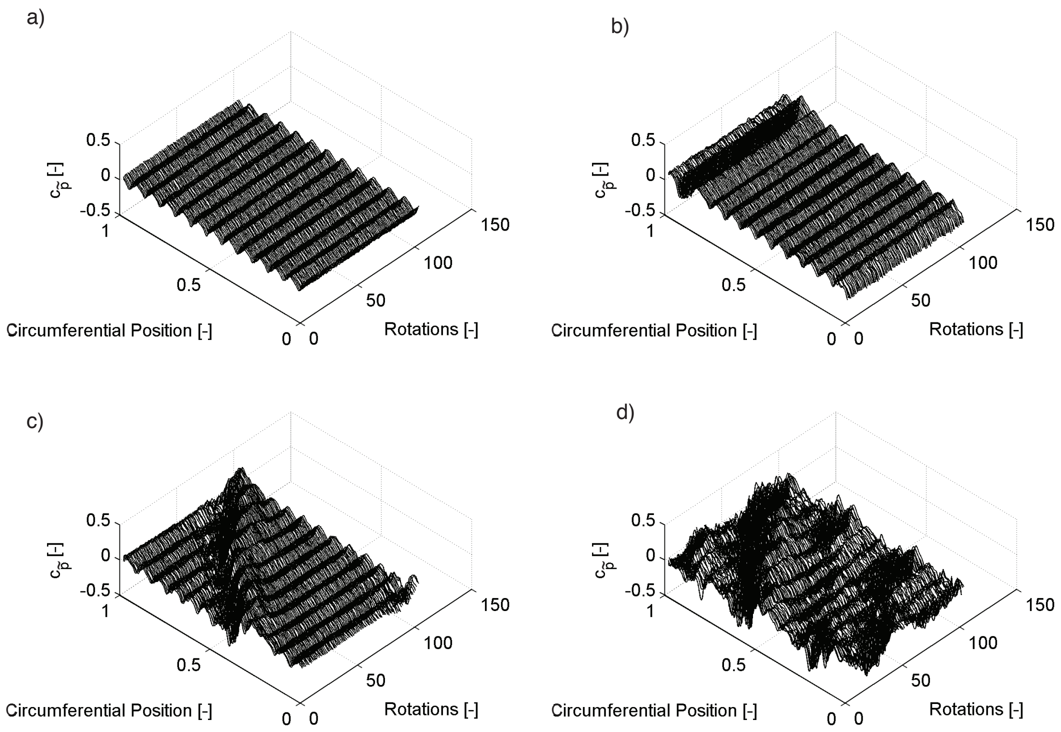

Figure 6.2: Performance curve and observed pressure pulsation patterns at impeller outlet

At flow rates close to the design point and above (a), a regular pattern of the pressure fluctuations due to the passage of the diffuser vanes can be identified. Already at high part-load operation (b), a locally fixed high pressure zone arises in the rotor-stator interface which is attributed to flow separation in the diffuser. A further decrease of the flow rate (c) yields a rotation of this high pressure zone with a very low rotational speed. At the lowest analyzed flow rate (d), the number of high pressure zones increases and their rotation becomes very irregular.

Figure 6.3 presents the evolution of pressure fluctuations in the impeller and in the diffuser in function of the relative flow rate. With reducing flow rates, the pressure fluctuations increase in the rotating domain as well as in the stationary domain.

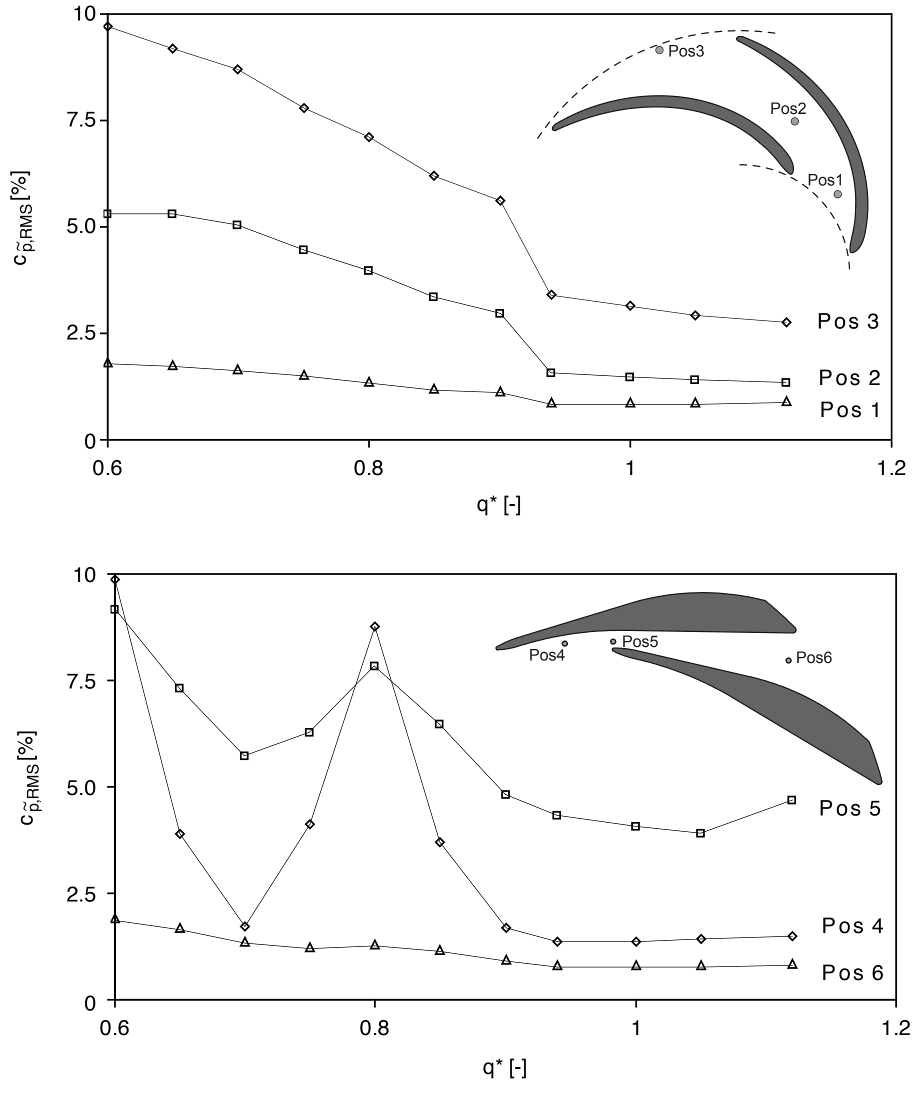

Figure 6.3: Pressure fluctuations at different positions and flow rates

The impeller pressure fluctuations increase while approaching the Rotor-Stator interface and show a change in slope between q*=0.94 and q*=0.9. This sudden increase in the impeller pressure fluctuations coincides with the appearance of flow separation in the diffuser.

In the stationary domain, the minimum pressure fluctuations are found at the design flow rate. Below this design flow rate, the pressure fluctuations in the Rotor-Stator interface as well as in the diffuser throat reach a maximum at q*=0.8; this is the flow rate, where the stall cell starts to rotate. The pressure fluctuations are attenuated towards the diffuser outlet. The spatial distribution of pressure fluctuations will be analyzed more detailed in the following chapters.

6.2 Influence of Rotational Speed on Observed Pressure Fluctuations

Guelich and Bolleter [57] postulated an approximately square dependence of pressure fluctuations on the rotational speed. Figure 6.4 depicts the dependence of the dimensionless pressure fluctuations obtained at different positions in the pump on the rotational speed.

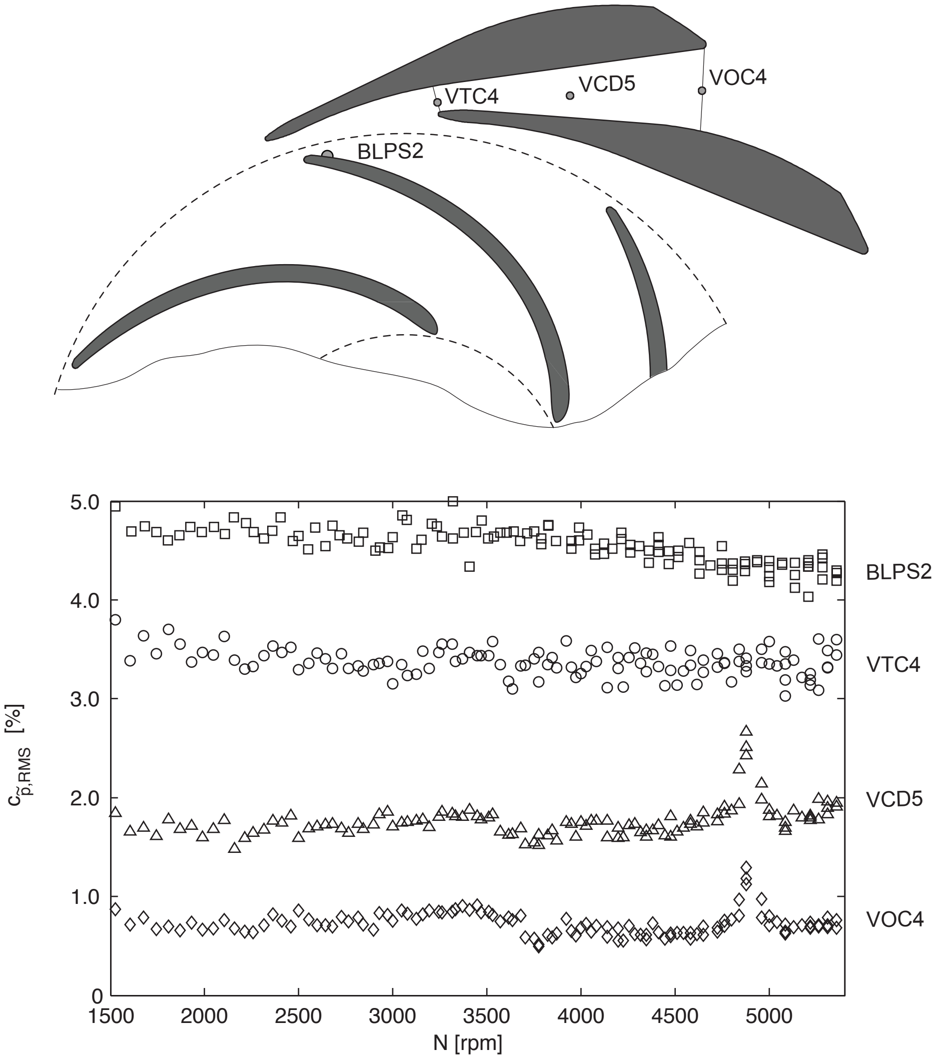

Figure 6.4: Pressure fluctuations at different positions and flow rates

While in the region of the impeller blade trailing edge and the diffuser throat, the dimensionless pressure fluctuations are nearly constant, thus follow a square function of the circumferential impeller outlet velocity, a local peak around 4900 rpm can be noticed in the diffuser channel and the diffuser outlet.

Figure 6.5 presents the pressure fluctuation amplitudes inside the diffuser channel at the impeller blade passing frequency and its harmonics. While until the third harmonic frequency the pressure fluctuation amplitudes roughly depend on the square of the ro-

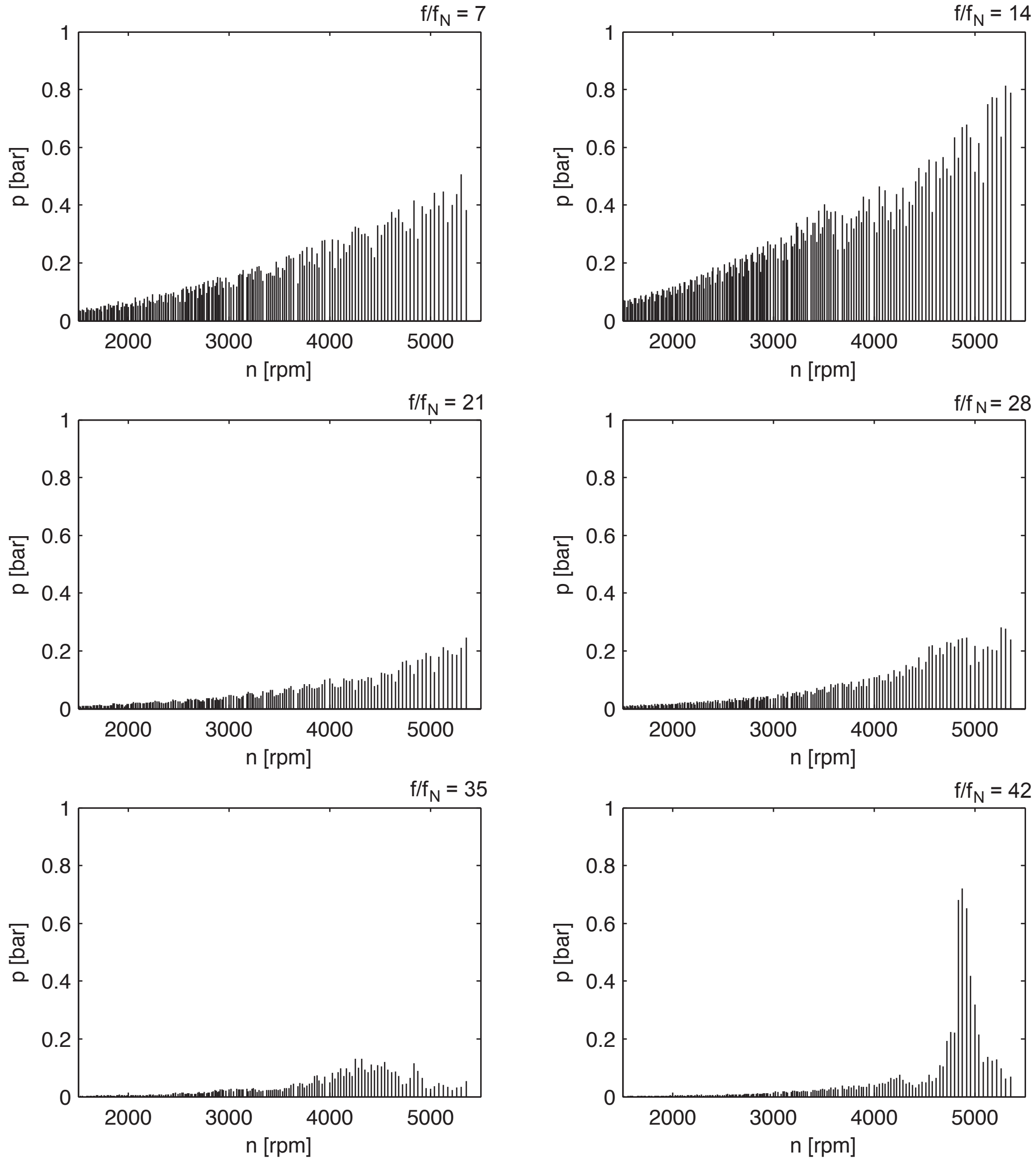

Figure 6.5: Pressure fluctuations at different positions and flow rates

tational speed, this is not anymore the case for the fourth and fifth harmonic. At a rotational speed of 4878 rpm a sharp peak appears in the amplitude plot for $f/f_N = 42$. This peak is predominant for this particular rotational speed.

Frequency and amplitude analysis shows that this sharp peak is the result of the excitation of an acoustic eigen frequency of the diffuser channel by pressure fluctuations due to Rotor-Stator-Interaction.

Figure 6.6 depicts the pressure fluctuation amplitude spectra at three different positions of the analyzed diffuser channel obtained during the operation of the pump at 4900 rpm and Figure 6.7 presents the pressure fluctuations phase at the frequency $f/f_N = 42$, calculated from averaged cross-spectra between the pressure sensors in these three positions.

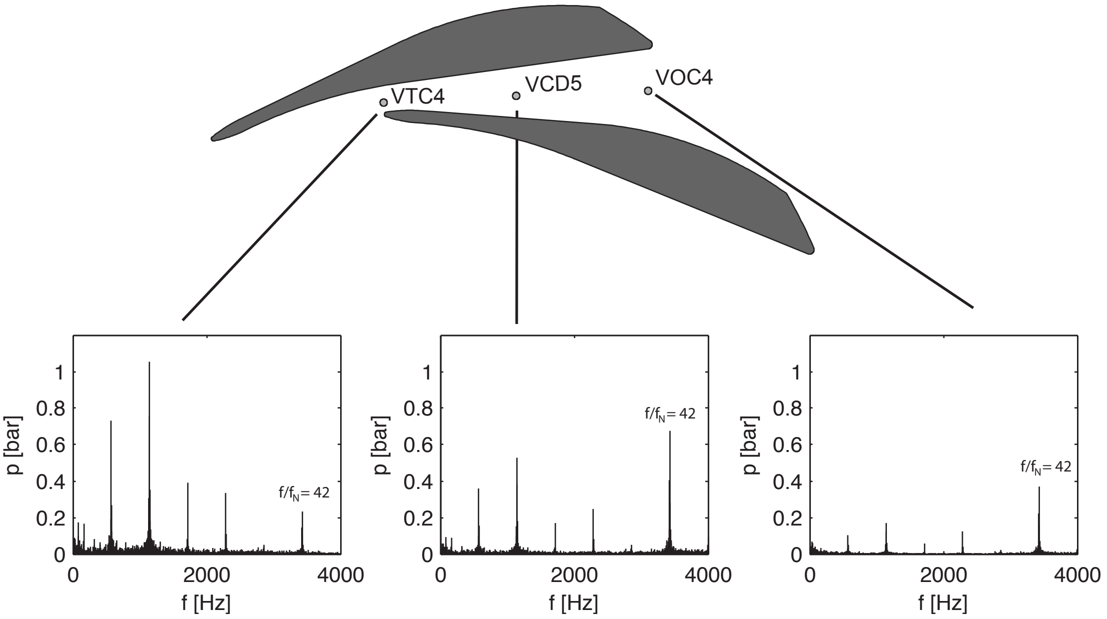

Figure 6.6: Pressure fluctuation amplitudes at different positions and flow rates

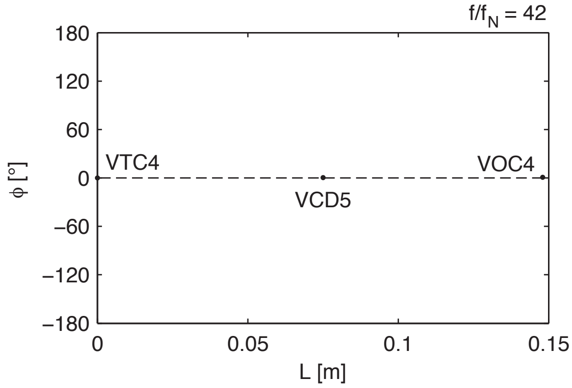

Figure 6.7: Phase relations at $f/f_N = 42$

No phase shift can be detected between the diffuser throat and the diffuser outlet.

The amplitude and phase information in these three positions allows the estimation of the first acoustic mode shape as a standing wave with pressure nodes at the diffuser throat and outlet as shown in Figure 6.8.

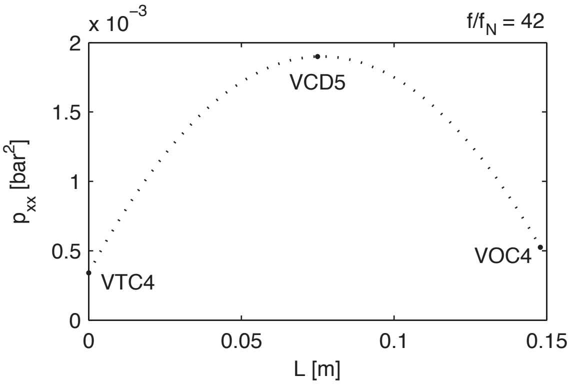

Figure 6.8: Estimated acoustic mode shape at $f/f_N = 42$

An estimation of the wave speed inside the diffuser channel using equation (6.1), which defines the eigenfrequencies for a pipe with two open ends, yields for the first acoustic eigenfrequency a wave speed of 1030 m/s, which is comparable to the wave speed estimated using the results of the analysis of the diffuser deformation [13].

$$f_k = k \cdot \frac{a}{2L} \qquad ; \qquad k = 1, 2, 3, \ldots \tag{6.1}$$

It is of some importance to notice, that the passage of an acoustic natural frequency in a diffuser channel in this particular geometry does not affect the pressure fluctuations experienced by the impeller, since at the diffuser throat, close to the Rotor-Stator Interface, a pressure node is located, the same is the case for the diffuser outlet channel. The energy transfer through the existence of a velocity maximum at the location of the pressure node appears not to affect the impeller pressure fluctuations. Therefore, the passage through an acoustic natural frequency may occur completely unnoticed from outside of the diffuser.

6.3 Side Room Pressures and Flow Rotation

The side room is connected to the main flow through a small gap. The pressure drop in this gap is small, the observed mean pressure in the side chambers at hub and shroud was nearly equal to the mean wall pressure inside the impeller close to the rotor stator interface. Figure 6.9 presents the pressure fluctuations in the impeller side rooms at different flow rates compared to the pressure fluctuations acquired in the impeller outer diameter at hub. The small gap between the impeller side walls and the diffuser side walls causes a strong attenuation of the pressure fluctuations observed in the side rooms at hub and shroud. At flow rates close to the design point, both side rooms experience nearly the same level of pressure fluctuations.

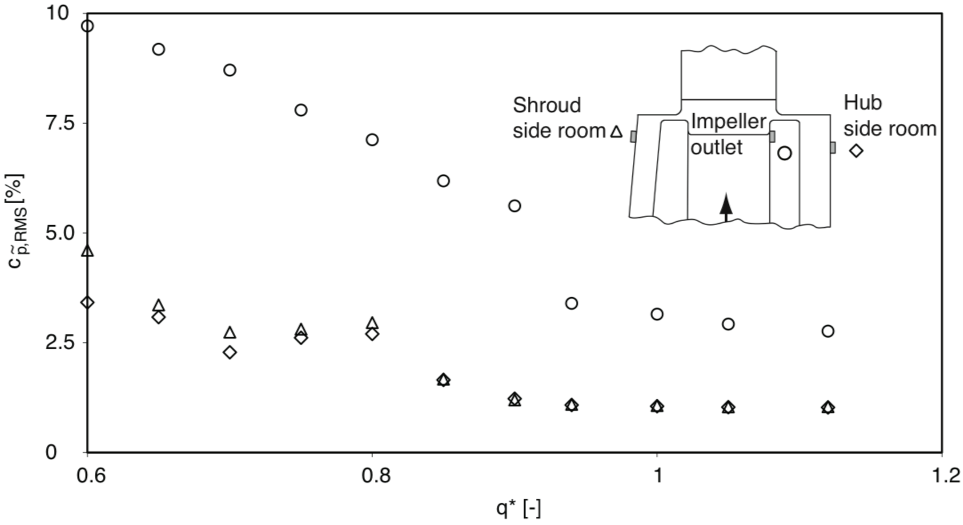

Figure 6.9: Evolution of pressure fluctuations in hub and shroud side room

At the occurrence of a rotating flow separation, a significant increase of the pressure fluctuations can be observed. This increase is more pronounced in the shroud side room than in the hub side room. At q* = 0.6, the pressure pulsations in the shroud side room are 35% larger than in the hub side room. An impeller outlet flow recirculation pattern as shown in Figure 1.6b might provide an explanation of the differences in the pressure fluctuations, observed at hub and shroud.

In the shroud side room, where additional pressure sensors are arranged at the side room inner diameter, the mean rotation in the side room can be determined using the relation

$$\bar{k} = \sqrt{\frac{2 \cdot (\bar{p}_a - \bar{p}_i)}{\rho \cdot u_2^2 \cdot \left(1 - \frac{r_i^2}{r_a^2}\right)}} \tag{6.2}$$

The rotation is reduced with reduced flow rates. When flow separation appears in the diffuser, a steep drop in the side room rotation can be observed. This indicates an interaction of the side room rotation with the high pressure zone in front of the detached diffuser channel. The strong reduction of the fluid rotation in the side room at the

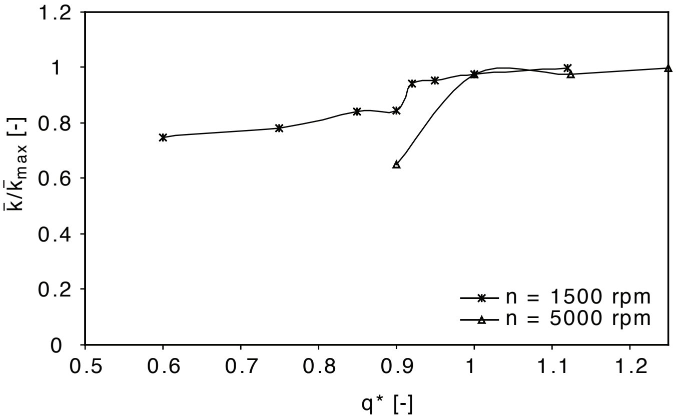

Figure 6.10: Mean rotation of fluid in shroud side rooms at different flow rates

presence of stall might be explained by the fact, that from the stall cell, fluid with very low circumferential velocity enters the side chamber, which yields a deceleration of the side room flow rotation due to the mixing of the entering fluid with the rotating liquid. The reduction was largest in the case of the synchronous pressure fluctuations provoked by the simultaneous passage of two impeller blades through the stator high pressure zones (n = 5000 rpm in Figure 6.10).

Chapter 7

Analysis of Hydraulic Phenomena for Design Conditions

7.1 Impeller Pressure Fluctuations

7.1.1 Estimation of Reference Pressure and Evaluation of Pressure Fluctuations at Impeller Inlet

The four pressure sensors located in the impeller inlet hub and shroud (see Figure 7.1) are used to determine the reference pressure for the calculation of static pressure coefficients. The reference pressure is defined as the average of the steady mean pressures of these four sensors.

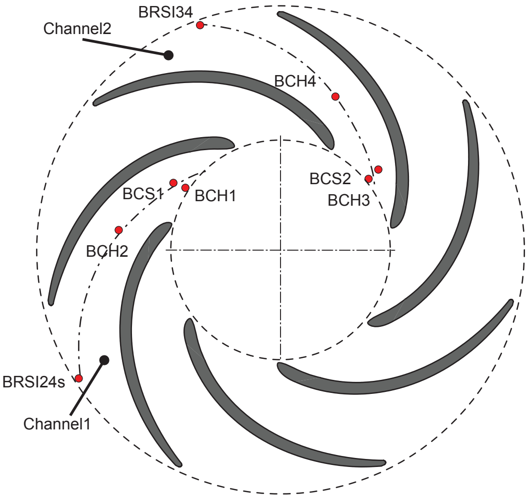

Figure 7.1: Analyzed sensor positions in the impeller

The mean pressures obtained in these four positions did not express large variations depending on the relative flow rate, even at flow rates, where part-load recirculation in the impeller inlet would be expected to impose a significant pressure difference between hub and shroud.

The pressure fluctuation spectra in the impeller eye (see Figure 7.2) show contributions at the impeller rotational speed, at nine times of the impeller rotational speed and at twelve times of the impeller rotational speed (Figure 7.3).

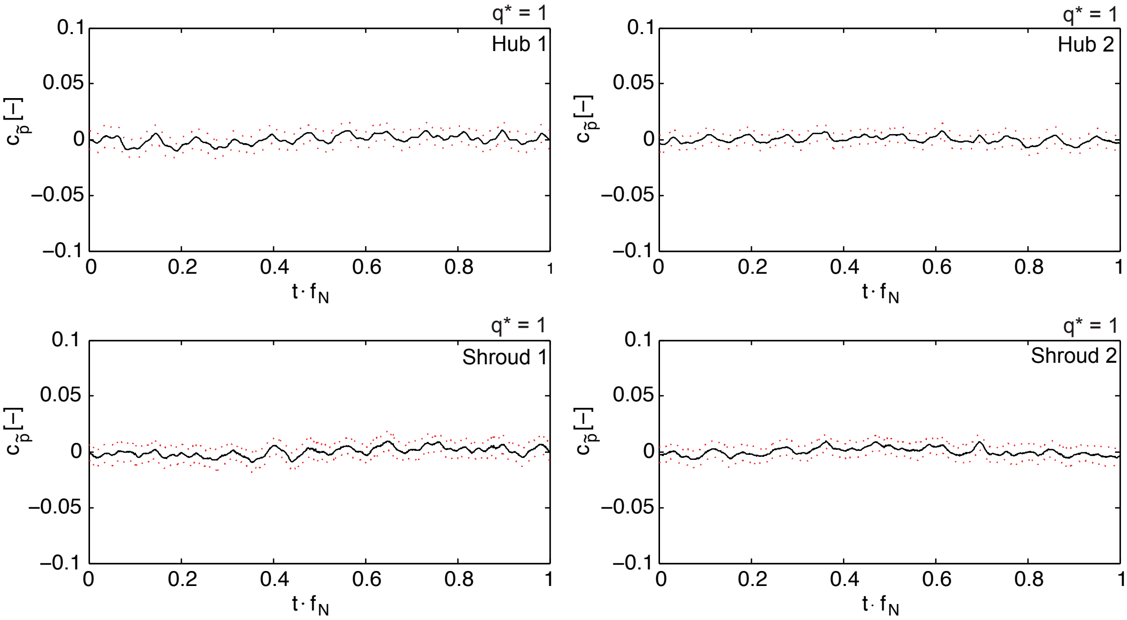

Figure 7.2: Phase averaged pressure fluctuations at impeller inlet

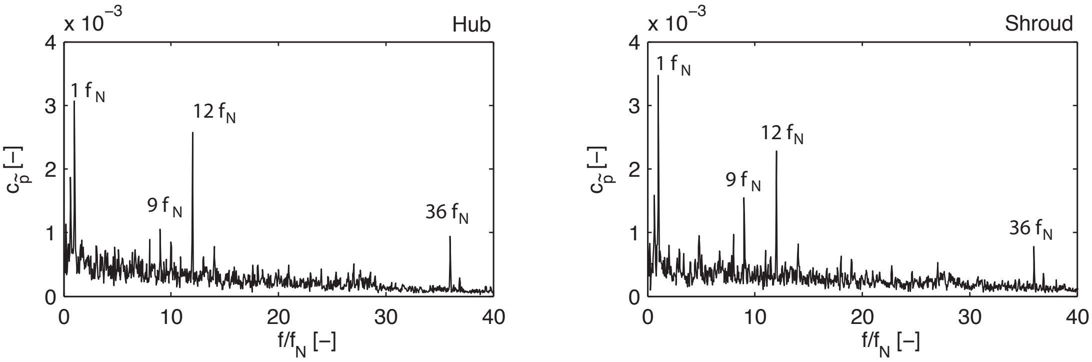

Figure 7.3: Amplitude spectra at impeller inlet

These different peaks may be explained as follows:

- The peak observed at the impeller rotational speed can be explained by geometrical variations of the stationary components upstream of the impeller, yielding a variation in the circumferential distribution of the inflow velocity.
- The peak at nine times rotational speed is related to the passage of the impeller inlet through the wakes of the nine return vanes of the artificial stage arranged upstream of the impeller.
- The peaks at twelve and thirty six times of the impeller rotational speed are the result of the Rotor-Stator Interaction, as it will be shown in the following section.

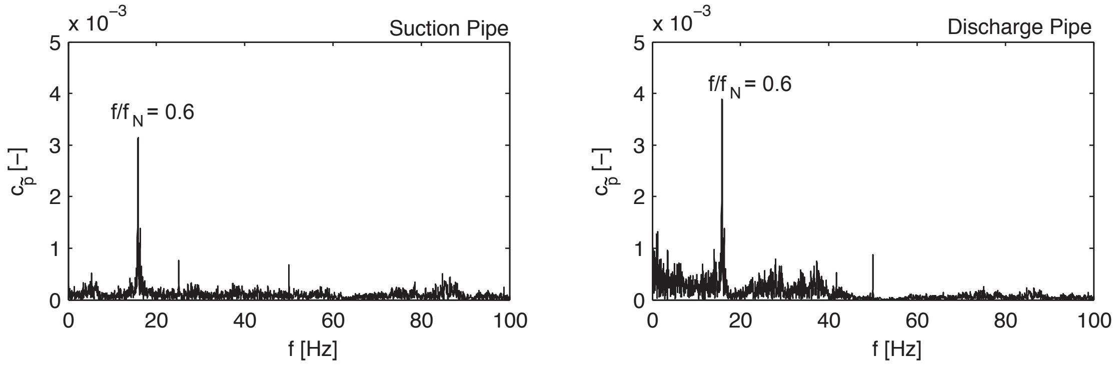

Figure 7.4: Amplitude spectra at pump inlet and outlet

Another subsynchronous peak can be identified around 16 Hz (see Figure 7.4). A spectral line at this frequency is found at all flow rates and rotational speeds (with minor variations due to the operating pressure in the test loop) and throughout the suction pipe, impeller, diffuser, annular casing and discharge pipe and has been identified as the first acoustic natural frequency of the test loop by the response of the piping system to a pressure pulse, created by a piston, integrated into the suction line (see Figures 4.11, 7.5 and 7.6).

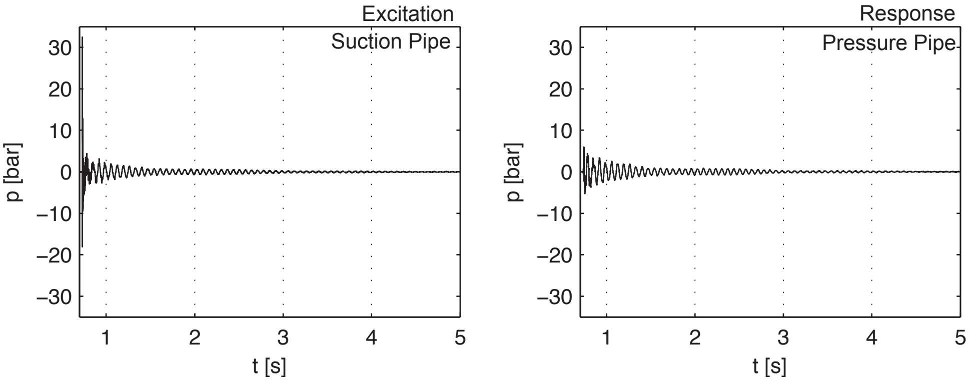

Figure 7.5: Pressure pulse excitation and systems response

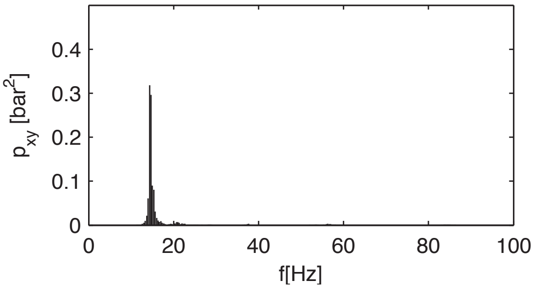

Figure 7.6: Cross-power spectrum between suction pipe and pressure pipe

7.1.2 Evolution of Pressure fluctuations in Impeller Channel

The pressure sensors, distributed in the impeller channels (see Figure 7.1) are used to examine the evolution of the pressure fluctuations from the impeller inlet to the impeller outlet. Figure 7.7 presents the phase averaged pressure fluctuations, as they evolve during the passage through the impeller channels.

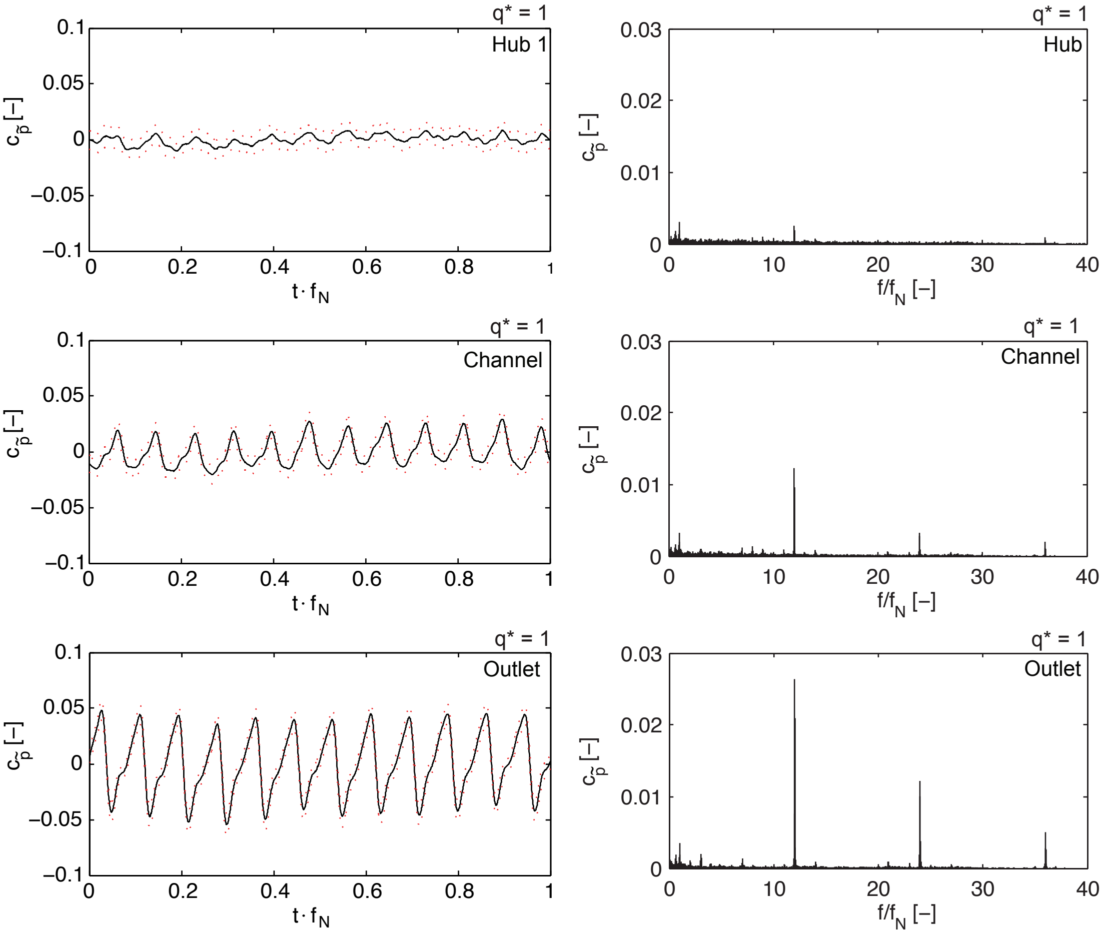

Figure 7.7: Phase averaged pressure fluctuations at different impeller channel positions

As already perceivable in the course of the analysis of the pressure fluctuations RMS values (Figure 6.3), a strong increase of the fluctuation amplitudes can be observed, when the impeller outlet - the Rotor-Stator interaction zone - is approached.

The pressure fluctuations measured inside the impeller channel are in phase, while the pressure fluctuations measured close to the Rotor-Stator interface, are not in phase anymore. Figure 7.8 depicts the phase relation at $f/f_N = 12$ and $f/f_N = 24$.

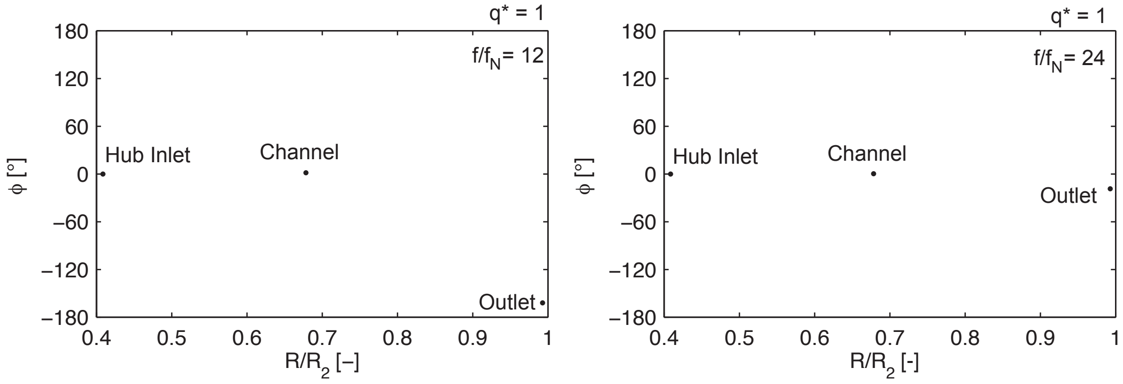

Figure 7.8: Phase averaged pressure fluctuations at different impeller channel positions

7.1.3 Spectral Analysis and Rotor-Stator Interaction Patterns in Rotating Domain

The pressure fluctuation spectra estimated from the unsteady pressure values obtained by the pressure sensors embedded in the impeller outer diameter in the center of the channels show that the impeller pressure fluctuations are dominated by the passage along the diffuser channels and its harmonics (Figure 7.9).

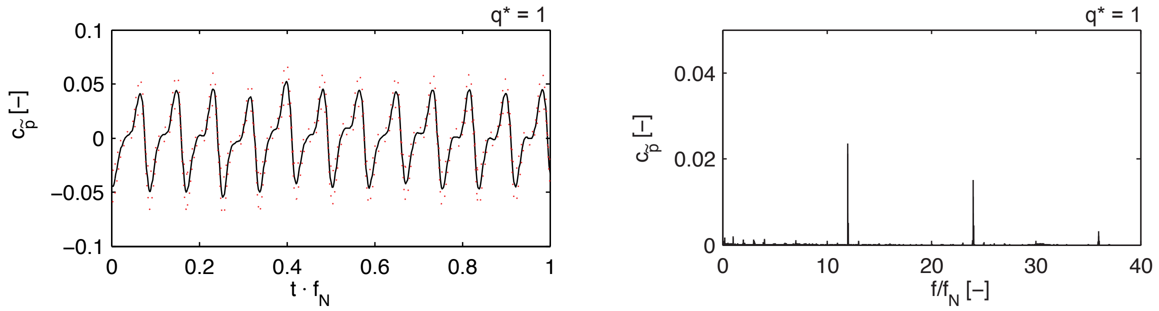

Figure 7.9: Phase averaged pressure fluctuations and amplitude spectrum obtained in impeller outer diameter

These pressure fluctuations are regularly distributed in space and time (see Figure 7.10) and are the result of the interaction of the rotating impeller pressure field and the stationary diffuser pressure field. The spatially distributed pressure fluctuations obtained in the impeller outlet are used to perform a 2D-FFT as outlined in 5.2.3.

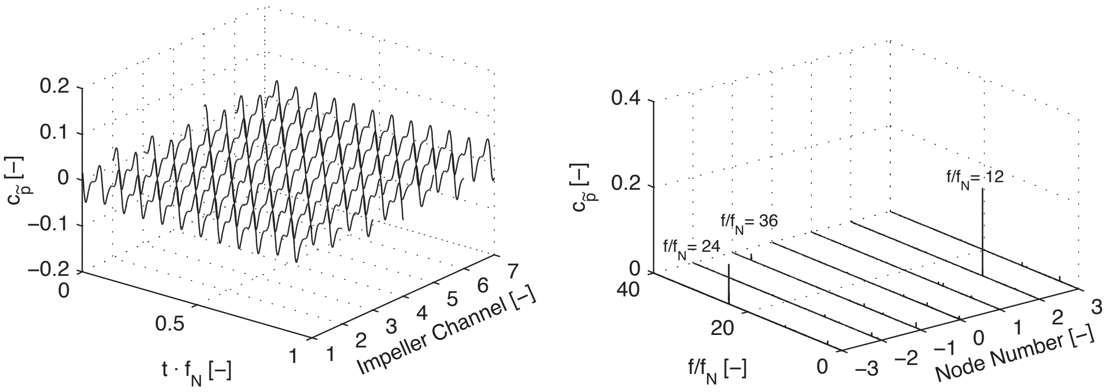

Figure 7.10: Circumferential distribution and 2D-FFT of impeller pressure fluctuations at q*=1

The 2D-FFT allows the decomposition of the acquired pressure fluctuations into three circumferential pressure waves, where the wave at $f/f_N = 12$, having 2 nodes is spinning forward, the wave at $f/f_N = 24$, having three nodes is spinning backwards and the wave at $f/f_N = 36$ is having one node and is spinning backward with respect to the impeller rotational sense.

The phase relations for the RSI frequencies, estimated from averaged cross-power spectra, unveil the number of nodes, as well as their rotational direction.

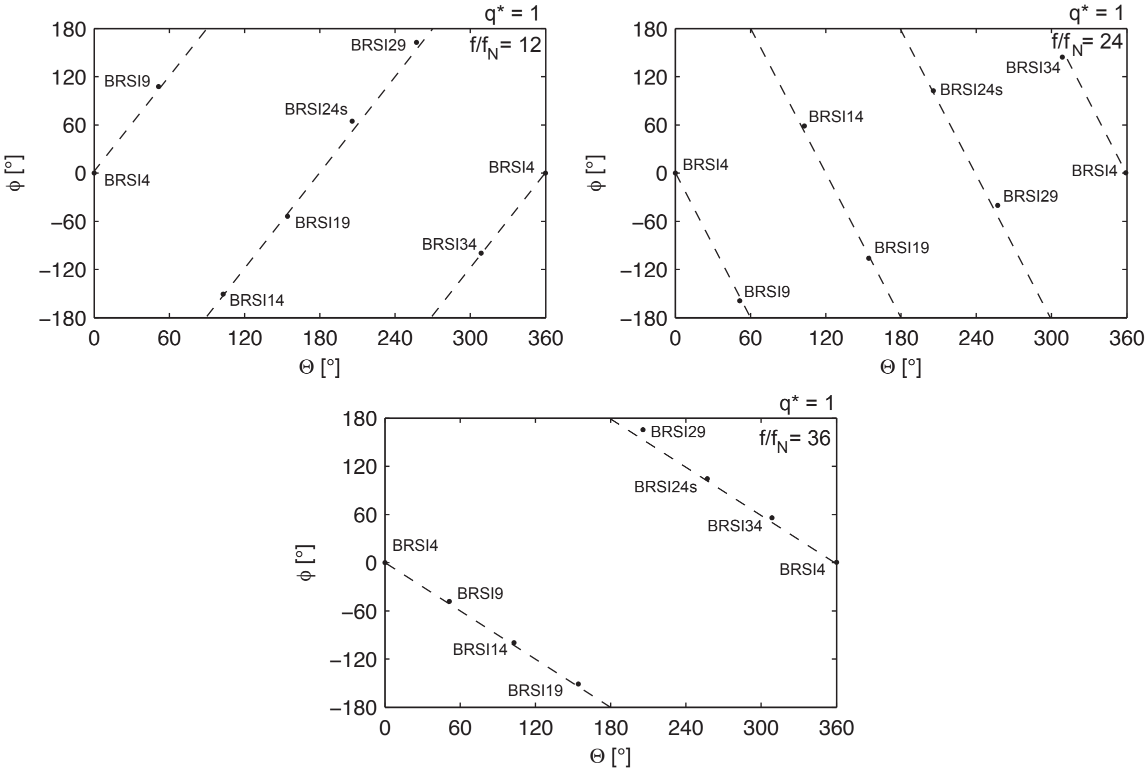

Figure 7.11: Phase relations for impeller pressure fluctuations at RSI frequencies

The pressure fluctuations, obtained by the spatially distributed sensors can be used to verify the rotor-stator interaction pressure fluctuation patterns. As described in section 1.2, the RSI-modes can be estimated using relatively simple relations. Equation 1.31 allows the prediction of the expected rotor-stator interaction patterns as presented in Tab.7.1.

			Rotating frame	
m	n	k_1	ω_1'/ω_N	f/f_N
2	1	2	6	12
3	2	-3	-8	24
4	2	4	6	24
5	3	-1	-36	36

Table 7.1: Expected rotor-stator interaction pattern in the rotating domain

The strongest expected RSI mode is the K=2 mode, having a frequency of $12 \cdot f_N$. Another mode appearing strongly is a backward rotating K=3 mode. These nodes have been identified in the measurement results. The amplitude and phase information at the RSI frequencies can now be used for the reconstruction of the predicted rotating modes (Figures 7.12 and 7.13).

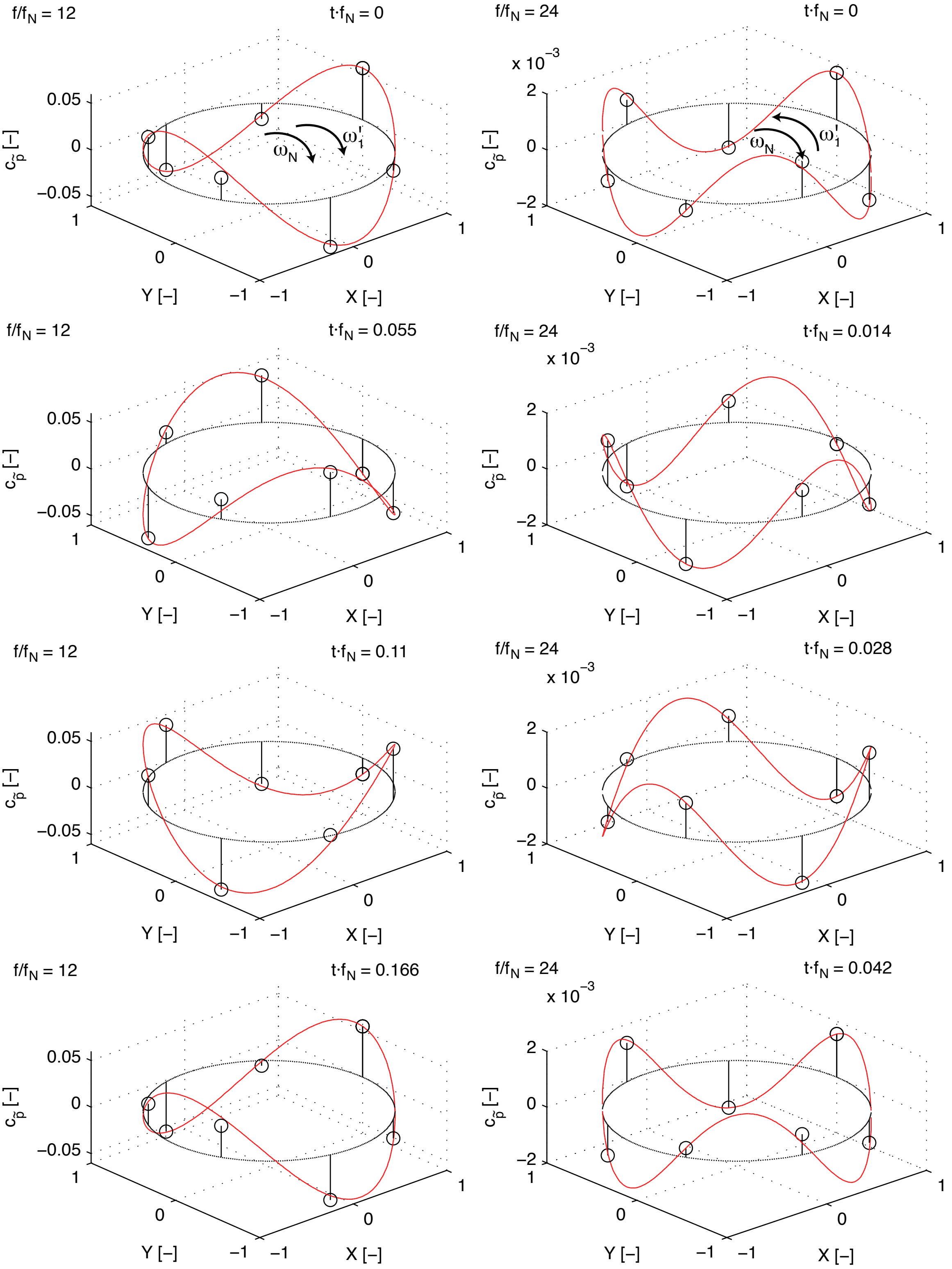

Figure 7.12: Rotating pressure waves at $f/f_N = 12$ and $f/f_N = 24$

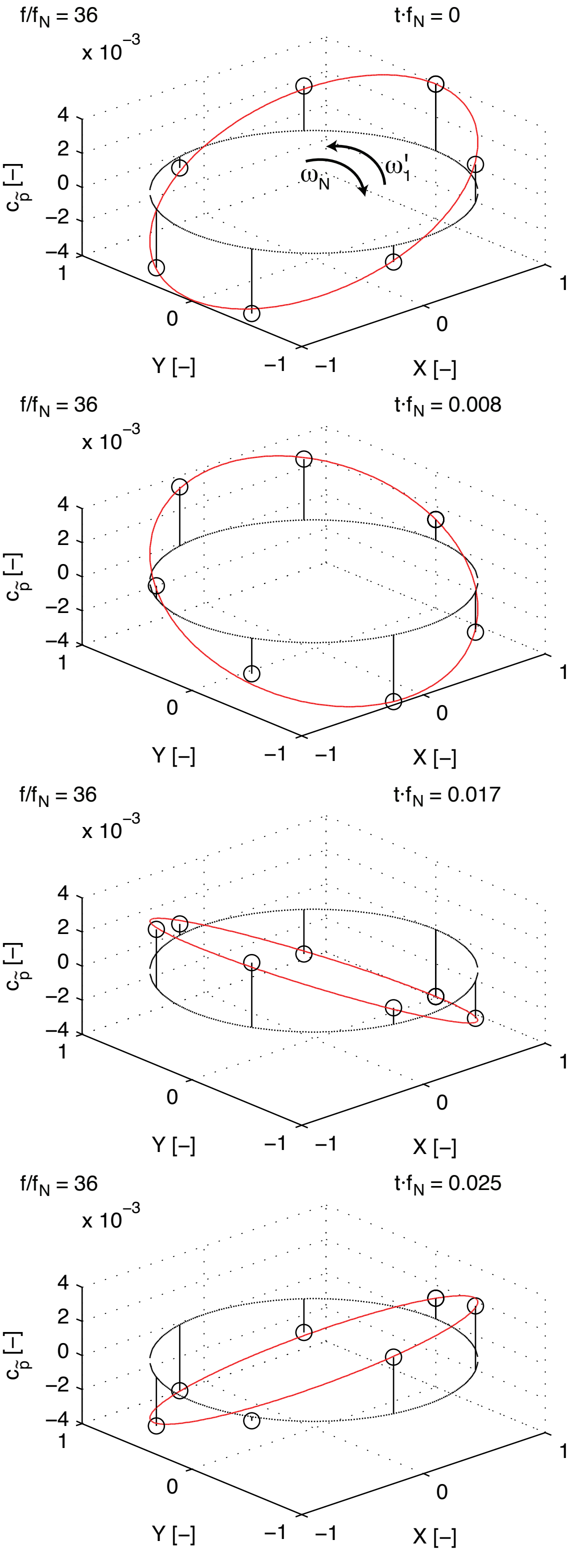

Figure 7.13: Rotating pressure wave at $f/f_N = 36$

7.2 Pressure Fluctuations in Stationary Domain

7.2.1 Pressure Fluctuations at Rotor-Stator Interface

In the diffuser throat, the phase-averaged pressure fluctuations are dominated by the passage of the impeller blade wakes (jet-wake interaction) and the passage of the high pressure zone close to the impeller pressure surface (potential interaction).

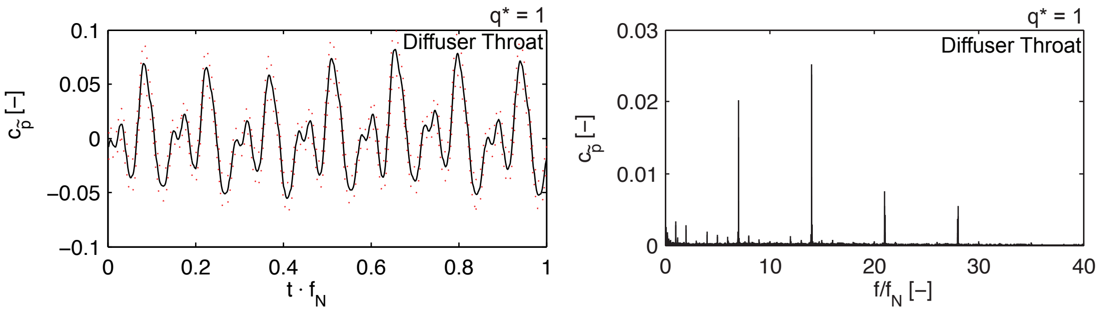

Figure 7.14: Phase averaged diffuser pressure fluctuations and associated amplitude spectrum in diffuser throat

The spatially and temporary distribution of the pressure fluctuations acquired in the twelve diffuser throats, as well the the result of a 2D-FFT analysis as described in section 5.2.3 is presented in Figure 7.15. As in the rotating domain, various rotating pressure

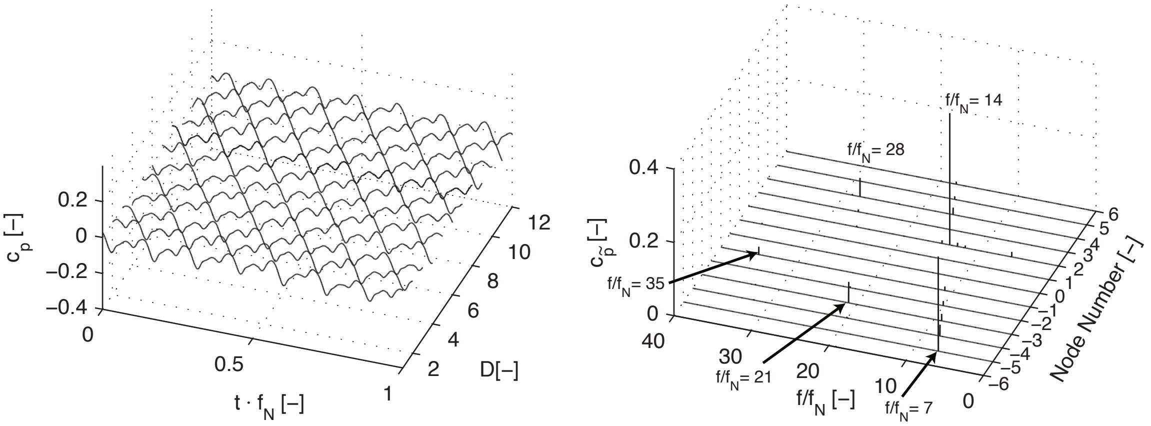

Figure 7.15: Circumferential distribution and 2D-FFT of phase averaged diffuser pressure fluctuations at q*=1

fluctuation patterns at the RSI frequencies can be identified. The most significant rotating pressure waves are found at $f/f_N = 14$ (a forward rotating pressure wave having two nodes) and at $f/f_N = 7$ (a backward rotating pressure wave, having five nodes). Apart of these, pressure waves at $f/f_N = 21$ (three nodes, backward rotating), $f/f_N = 28$ (four nodes, forward rotating) and $f/f_N = 35$ (one node, backward rotating) can be identified.

The relative phase between the RSI pressure fluctuations at the different circumferential positions estimated from average cross-spectra referring to the first diffuser channel, as shown in Figure 7.16 confirms the estimations based on the 2D-FFT in Figure 7.15.

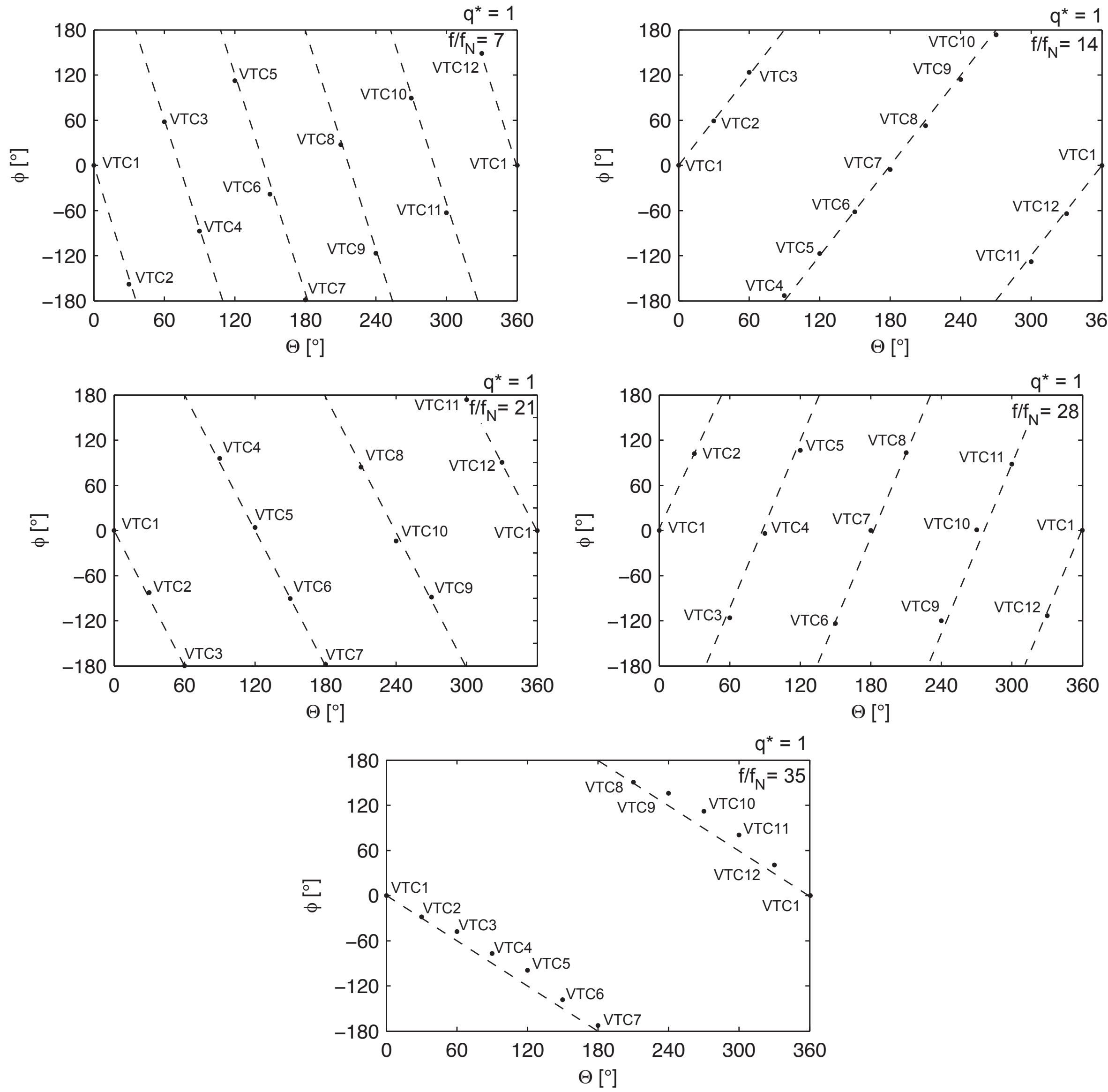

Figure 7.16: Phase relations for diffuser pressure fluctuations at RSI frequencies

An estimation of the pressure fluctuation patterns in the stationary domain according to the method presented in section 1.2 is presented in Table 7.2.

			Stationary frame	
m	n	k_1	ω_1/ω_N	f/f_N
1	1	-5	-1.4	7
2	1	2	7	14
3	2	-3	-7	21
4	2	4	7	28
5	3	-1	-35	35

Table 7.2: Expected diffuser RSI patterns for the vane number combination z_B=7 and z_V=12

In the following Figures 7.17, 7.18 and 7.19, a comparison between the rotating pressure waves predicted according to Equation 1.31 and the time dependent pressures calculated from the measured amplitudes and phase values in the different diffuser channel throat sections is outlined.

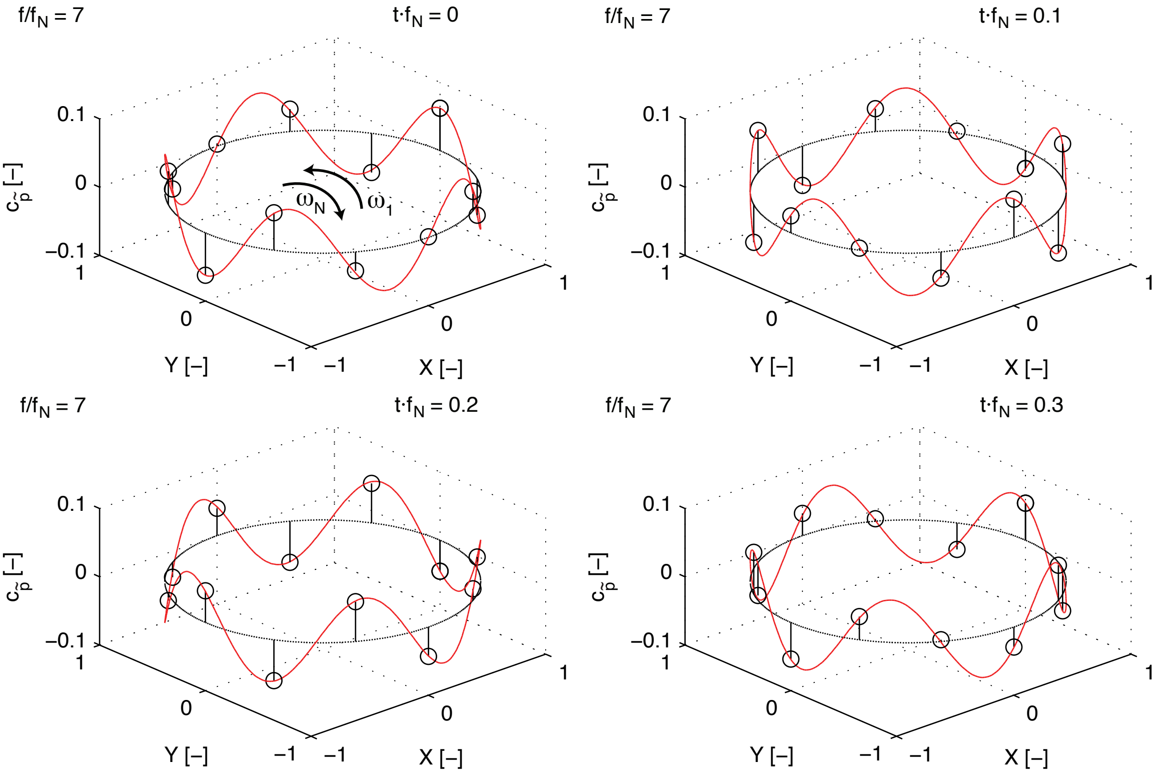

Figure 7.17: Reconstructed rotating pressure wave in stationary domain at $f/f_N = 7$

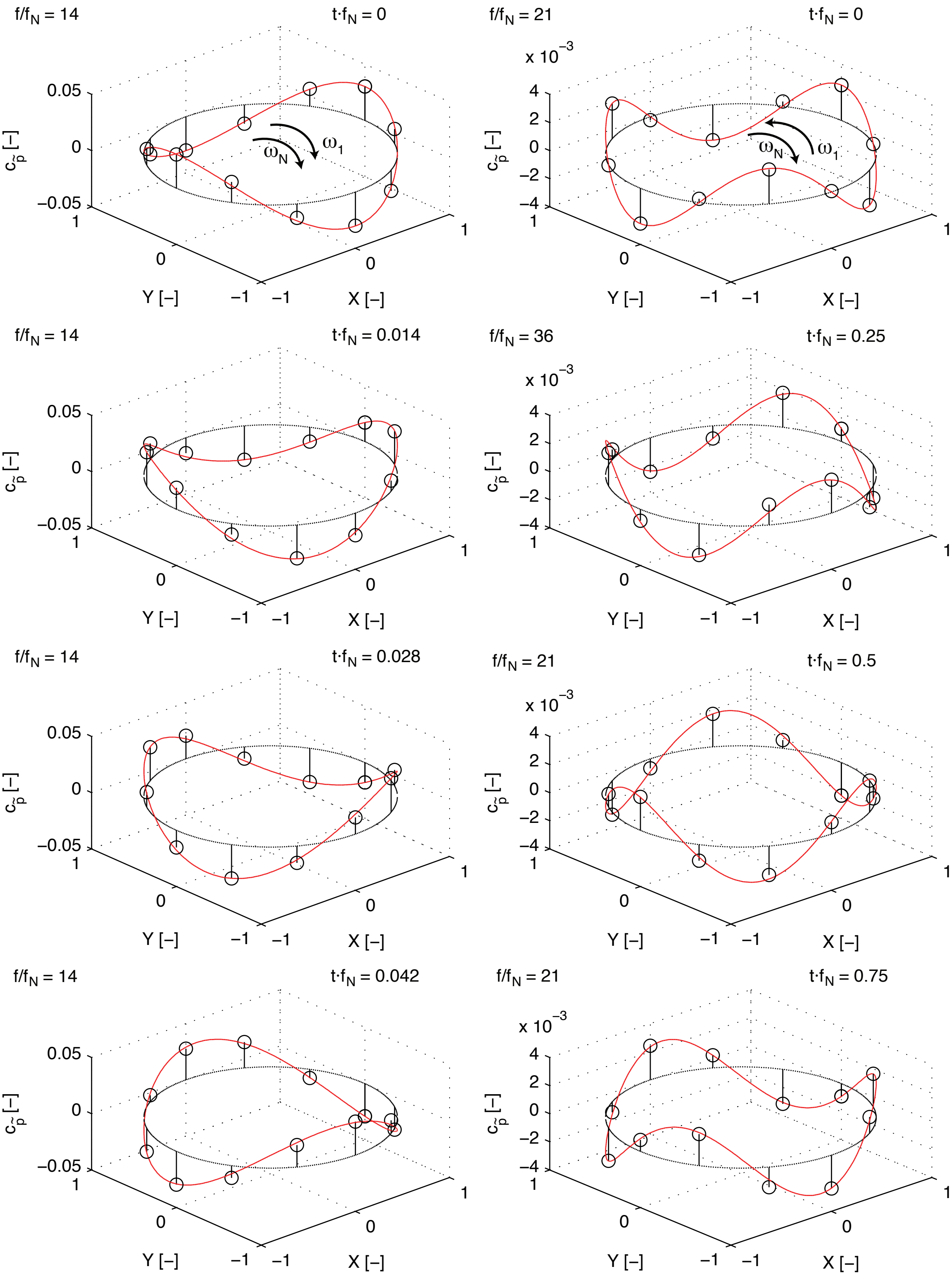

Figure 7.18: Reconstructed rotating pressure wave in stationary domain at $f/f_N = 14$ and $f/f_N = 21$

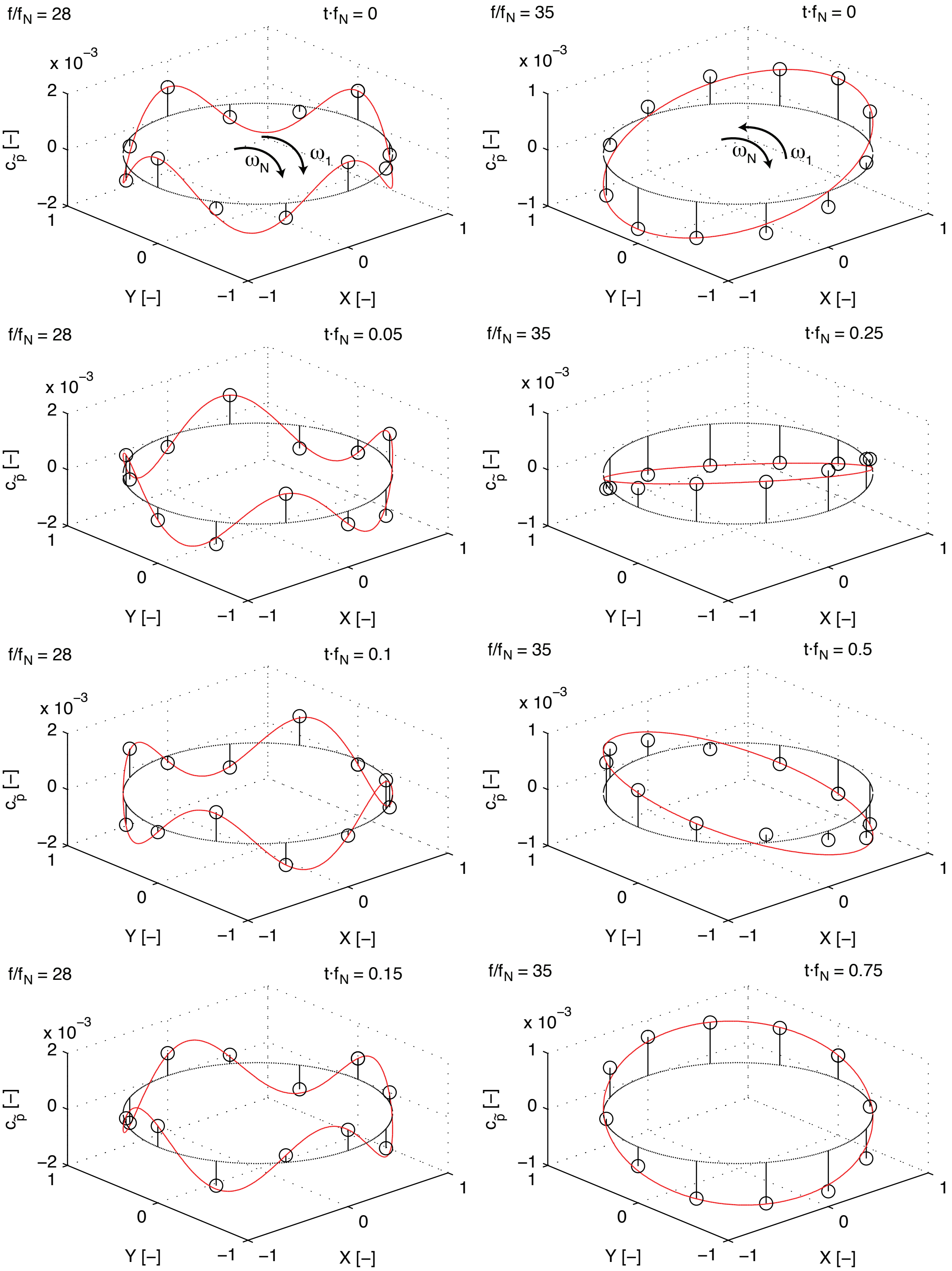

Figure 7.19: Reconstructed rotating pressure wave in stationary domain at $f/f_N = 28$ and $f/f_N = 35$

7.2.2 Evolution of Pressure Fluctuations in Stationary Domain

When no acoustic resonance in the diffuser channel is excited (see chapter 6.2), the pressure fluctuations imposed by the impeller blade passage and the Rotor-Stator interaction are attenuated during their propagation through the diffuser channel.

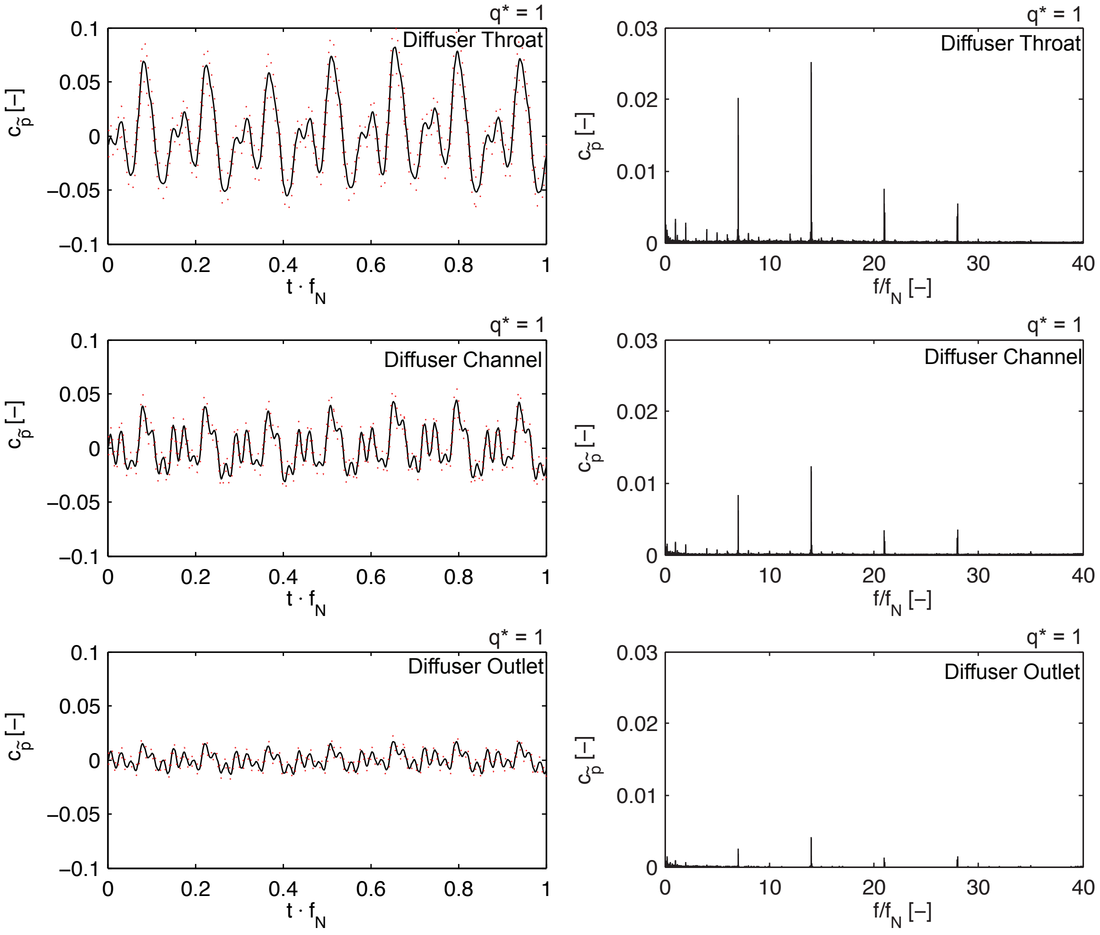

Figure 7.20: Evolution of pressure fluctuations in diffuser

Figure 7.20 presents the phase average and the associated amplitude spectra for the wall pressure fluctuations at the diffuser throat, one position in the diffuser channel between inlet and outlet and at the diffuser outlet. The positions are identical to the positions depicted in Figure 6.6.

Figure 7.21 shows the pressure fluctuation phase at the impeller blade passing frequencies and its harmonics, estimated from cross-spectra referring to the pressure sensor embedded in the diffuser throat. While at the impeller blade passing frequency, $f/f_N = 21$ and $f/f_N = 28$, the relative phase between the pressure fluctuation signals in the different diffuser channel positions is nearly zero, at $f/f_N = 14$ a clear phase shift of 30° can be observed between the diffuser outlet and the diffuser inlet.

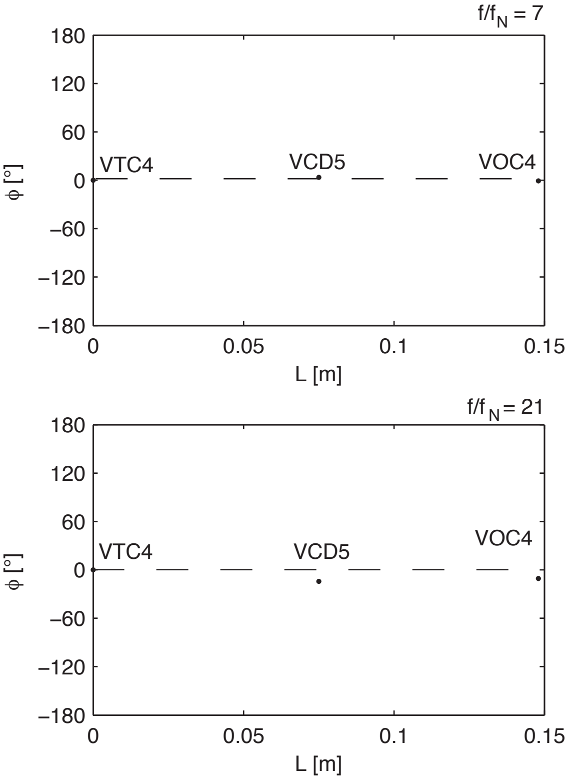

Figure 7.21: Propagation of pressure fluctuations in diffuser channel

This phase shift indicates a difference in the propagation mechanism of the pressure fluctuations at this specific frequency. While at the other RSI frequencies, acoustic propagation dominates the transmission mechanism (the distance between the sensors is so small that a phase shift is not detectable), the pressure fluctuations at $f/f_N = 14$ are convected and generate a forward rotating pressure wave having 2 nodes in the annular chamber. This pressure wave dominates the pressure fluctuations in the annular chamber, as it can be seen in Figure 7.22. At the other RSI frequencies, it was not possible to identify regular circumferential pressure fluctuation patterns indicating rotating pressure waves.

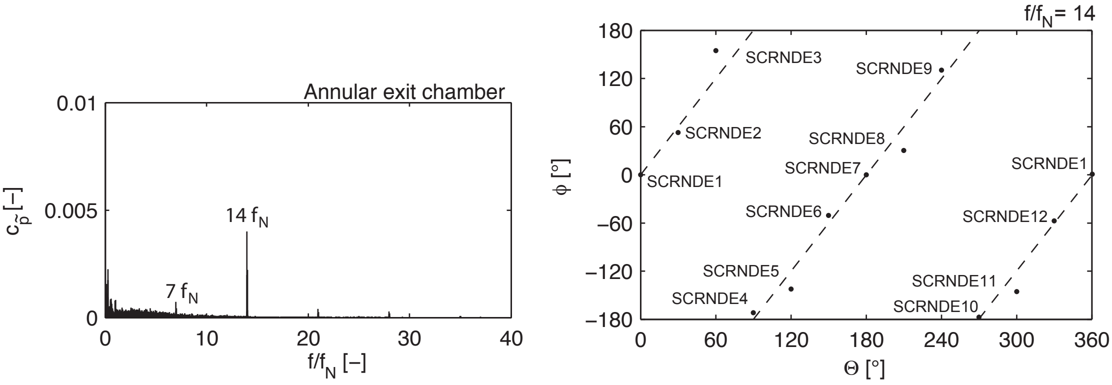

Figure 7.22: Amplitude spectrum and rotating pressure wave in annular casing at $f/f_N = 14$

7.3 Side Room Pressure Fluctuations

The pressure fluctuations due to the Rotor-Stator-Interaction are transmitted into the side rooms through the radial gap between the impeller side walls and the diffuser shrouds. Hub and shroud side rooms experience the impeller pressure fluctuations in phase but with different amplitudes. This yields a resulting pressure difference, which exhibits the RSI pressure fluctuation pattern (Figure 7.24).

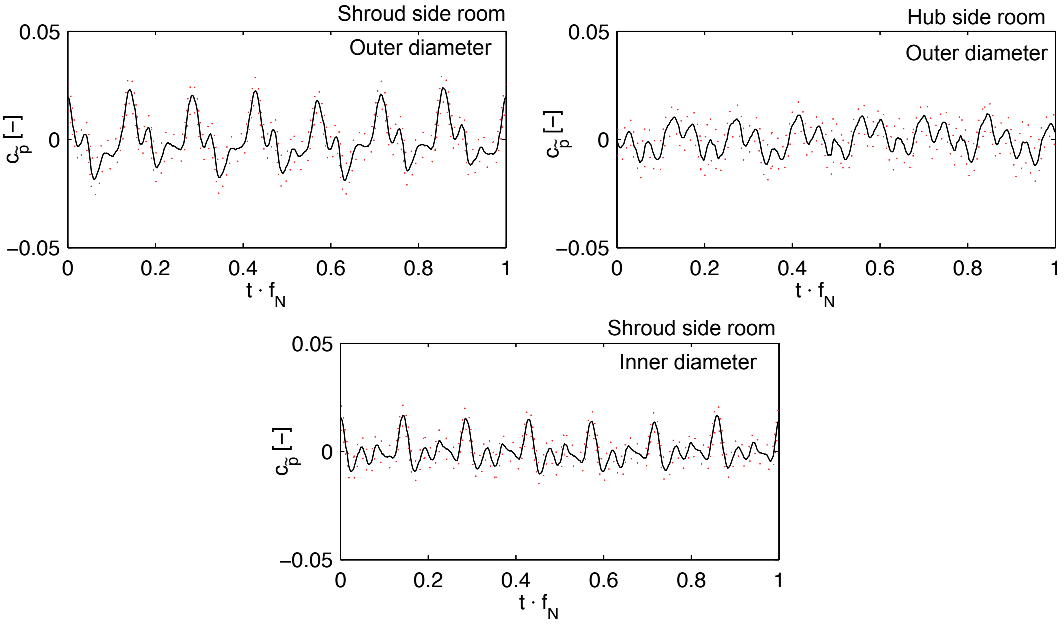

Figure 7.23: Phase averaged pressure fluctuations at different side room positions for q*=1

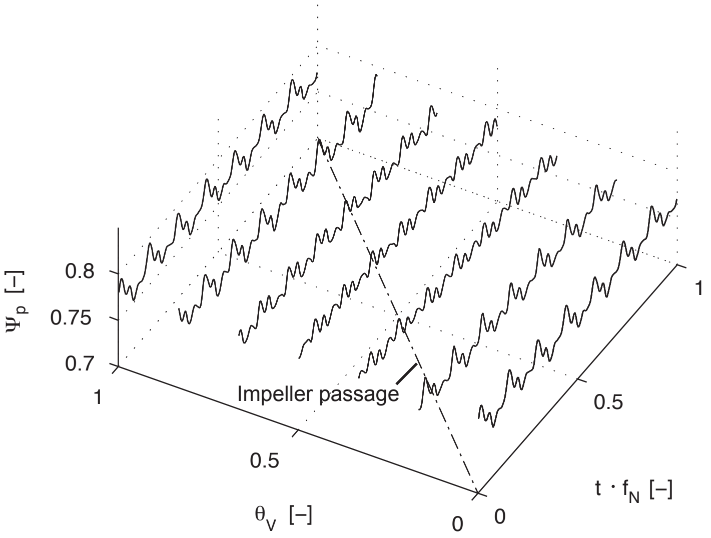

Figure 7.24: Circumferential distribution of side room pressure fluctuations

The estimation of the pressure fluctuation phase at $f/f_N = 14$ and $f/f_N = 21$, presented in Figure 7.25 unveils the same pattern as found in the analysis of the diffuser throat.

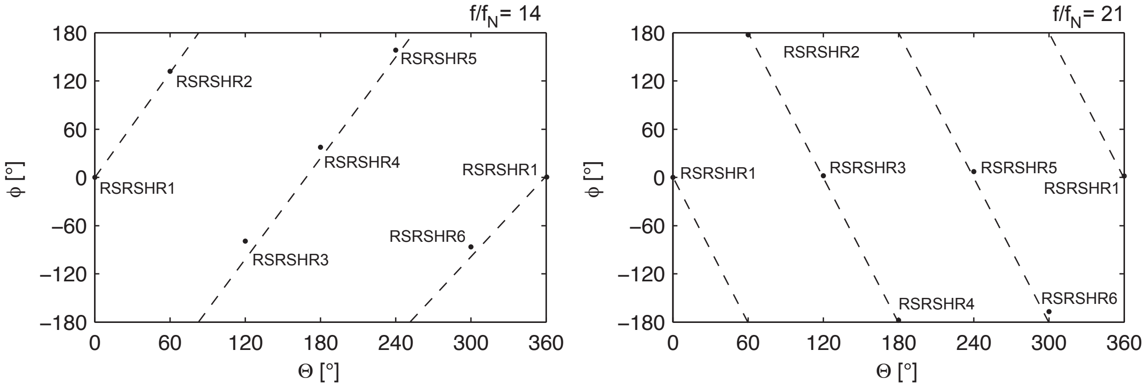

Figure 7.25: Shroud side room pressure fluctuations phase at $f/f_N = 14$ and $f/f_N = 21$

A circumferential interpolation of the phase averaged side room pressure fluctuation, using a least square fit on a sixth order polynom allows an estimation of instantaneous pressure values for all angular impeller positions at all circumferential side room positions (Figure 7.26).

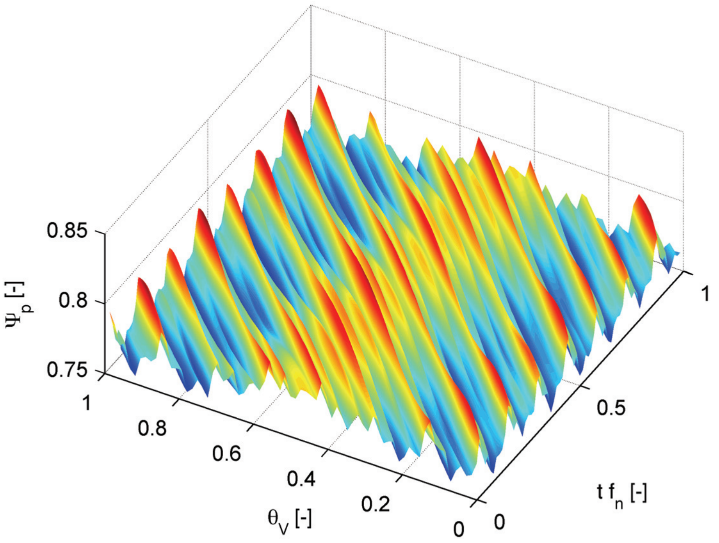

Figure 7.26: Interpolated shroud side room pressure fluctuations for q*=1

Using the interpolated side room pressure fluctuations at the design point, it is now possible to estimate the instantaneous static pressure difference between the impeller channel and the impeller side room as presented in Figure 7.27.

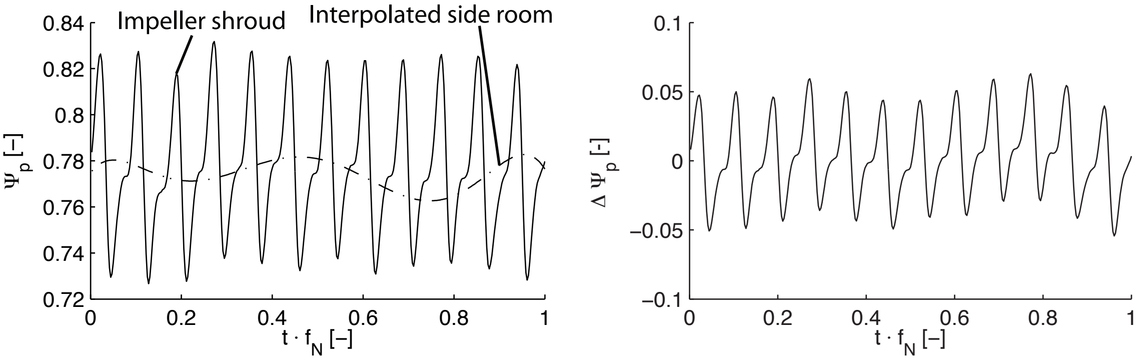

Figure 7.27: Instantaneous pressure difference between impeller channel and side room for q*=1

Recalling Figure 7.9 it can be concluded now, that the RSI pressure fluctuations, which are superposed on the steady pressure difference between the impeller channel and the side rooms yield net forces acting on the impeller side walls, which cause a deformation of the impeller having the same spatial and temporal distribution as the RSI pressure fluctuation patterns. This will be further analyzed in section 9.1 using the measured impeller shroud deformations at several circumferential locations distributed at the impeller outer diameter.

Chapter 8

Analysis of Part-Load Pressure Fluctuations

8.1 Stationary Diffuser Stall

8.1.1 Impeller Pressure Fluctuations

The stationary diffuser stall can be clearly identified using the pressure data obtained in the impeller outlet. The number of stall cells as well as their circumferential positions are irregular, no clear dependence on the rotational speed has been observed. Figure 8.1 illustrates this, showing the phase averaged pressure fluctuations in the impeller pressure surface at the trailing edge for a relative flow rate of $q^* = 0.9$, acquired at two different rotational speeds. While at 3000 rpm one stalled diffuser channel can be noticed, the number of stalled diffuser channels at 5000 rpm is increased to two, which are circumferentially separated by 150°.

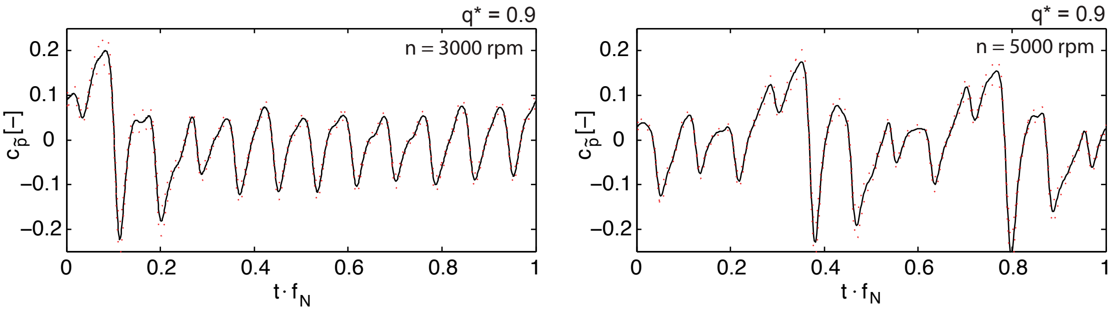

Figure 8.1: Phase averaged pressure fluctuations in impeller blade trailing edge pressure surface at different rotational speeds

The intensity of the impeller pressure fluctuations due to the flow separation in the diffuser depends on the relative flow rate. Figure 8.2 presents the normalized pressure fluctuations during one impeller revolution, obtained in the impeller outlet with the pressure sensor embedded in the blade pressure surface and one pressure sensor in the impeller shroud outer diameter between two impeller blades.

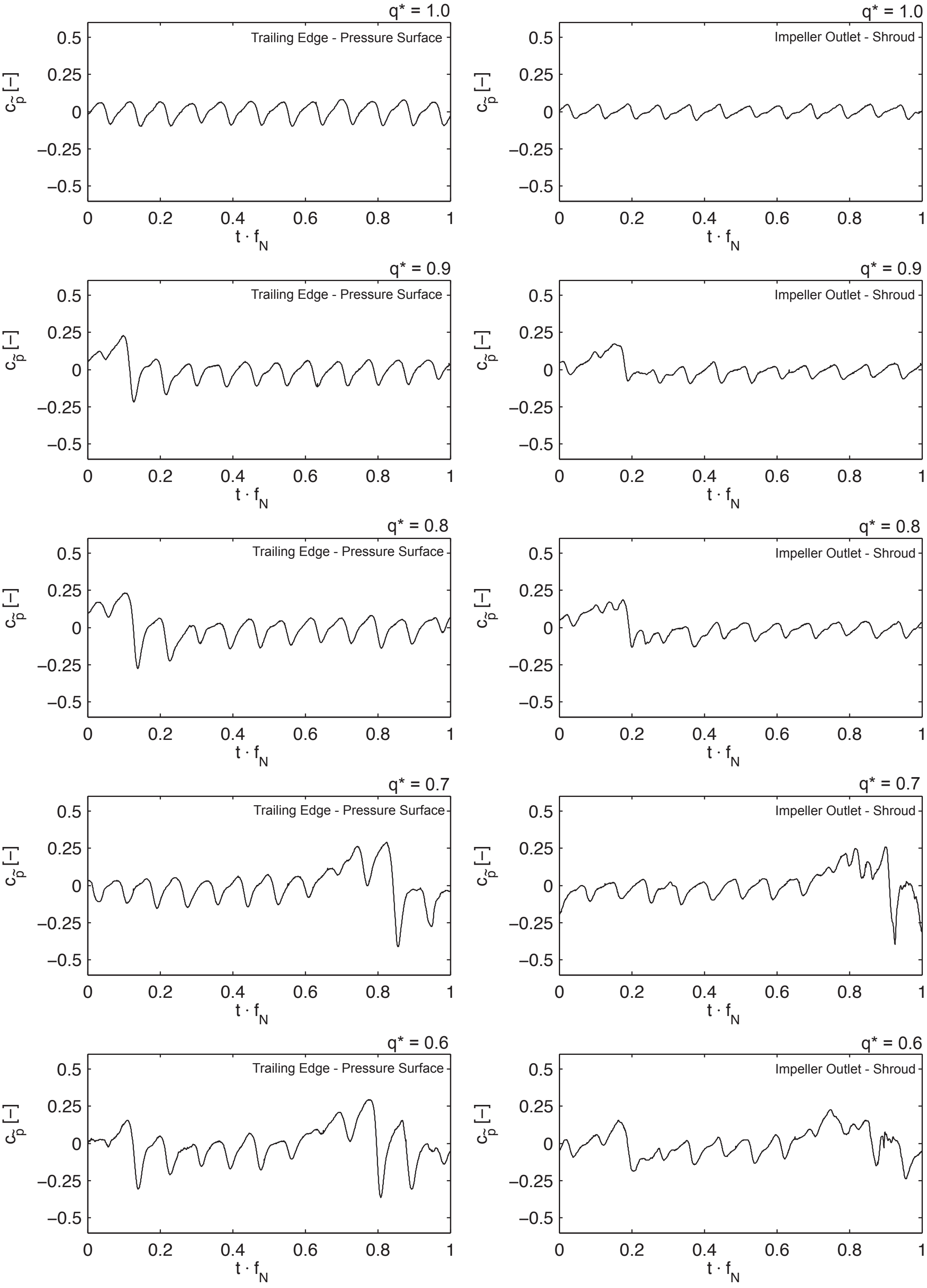

Figure 8.2: Impeller outlet pressure fluctuations at different flow rates

The pressure values have not been averaged, since during the acquisition of the pressure fluctuations for the lowest relative flow rate (q*=0.6), the stall cells irregularly appeared and disappeared at different circumferential positions.

With the appearance of flow separation in the diffuser, the normalized unsteady pressure increases during the passage of the stall cell to a maximum pressure value, followed by a sudden decrease to a minimum value. The maximum value remains nearly constant for all part load relative flow rates, but the minimum value decreases with decreasing relative flow rate.

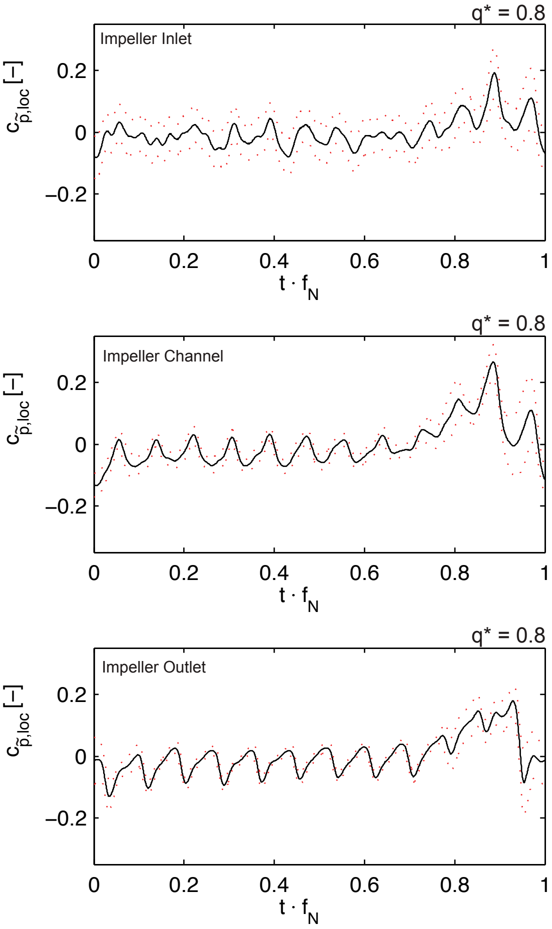

Figure 8.3: Phase averaged pressure fluctuation evolution inside the impeller, normalized with local circumferential velocity

The nearly constant pressure increase during the stall passage at all relative flow rates might be explained as follows. When one impeller channel passes a stalled diffuser channel, the liquid leaving the impeller needs to be deviated towards the following diffuser channel, which is accompanied by a local deceleration of the flow inside the impeller channel. The kinetic energy in the flow will be transformed to static pressure as the flow is decelerated. Figure 8.3 presents the pressure fluctuations in the presence of diffuser stall throughout one impeller channel, normalized to the **local** circumferential velocity, calculated with the actual sensor position. The maximum value for the normalized pressure fluctuations remains nearly constant, as it is limited by the local stagnation pressure.

The minimum pressure values, appearing directly after the stall passage, are imposed by the pressure profile around the diffuser vane leading edge. As the incidence increases due to the reduction of the outlet flow angle, the minimum pressure peak reduces further and further; this behavior is well known from measurements of pressure distributions around profiles.

Spectral analysis of the impeller pressure fluctuations unveils additional frequency lines. The additional pressure fluctuation frequency lines at the product of the cell number and the rotational frequency and its harmonics are rather obvious. Furthermore, modulation results in lines below and above the diffuser vane passing frequency.

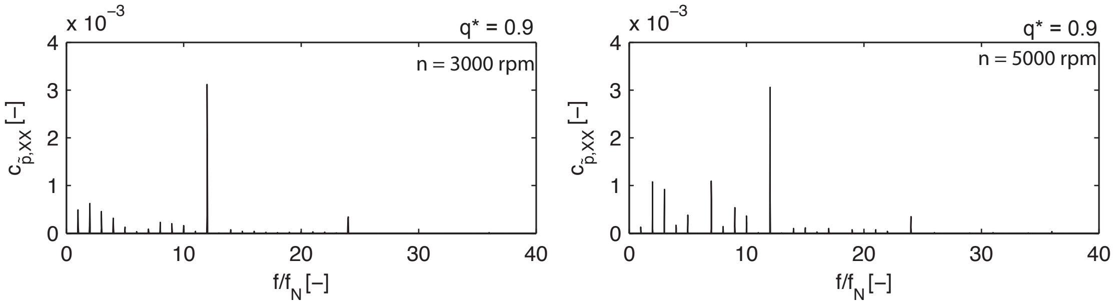

Figure 8.4: Impeller pressure fluctuations in the presence of stall

The number of stationary stall cells can be also identified with an analysis of the pressure fluctuation phase at different circumferential positions in the impeller outlet. Figure 8.5 presents the analysis for the two operating points shown in Figure 8.1.

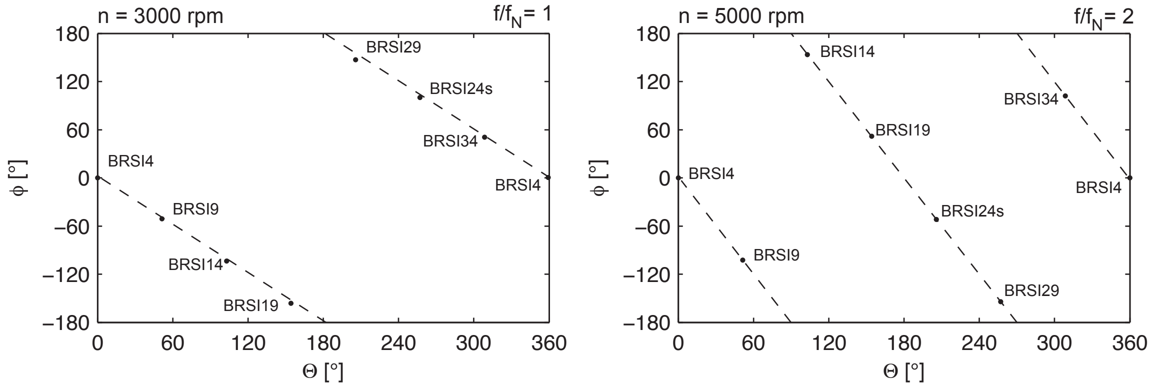

Figure 8.5: Phase relations at stall frequencies

8.1.2 Diffuser Pressure Fluctuations

The keyphasor, installed in the pump casing (see section 4.5.4), permits the angular synchronization between the unsteady pressures acquired in the impeller and in the diffuser. Figure 8.6 presents the position of the pressure sensor, embedded in the blade trailing edge pressure surface, relative to the diffuser channels at the maximum and minimum pressure within one impeller revolution. The identification of the stalled diffuser channels can now be based on this figure. The maximum pressure has been measured, while the impeller passed the diffuser channel 12 (Figure 8.6a) and the minimum pressure is observed, when the sensor is aligned with the suction surface of the subsequent diffuser vane (Figure 8.6b). Furthermore, the passage of the preceding diffuser channel (11), is associated with a significantly higher pressure than the passage of the remaining diffuser channels.

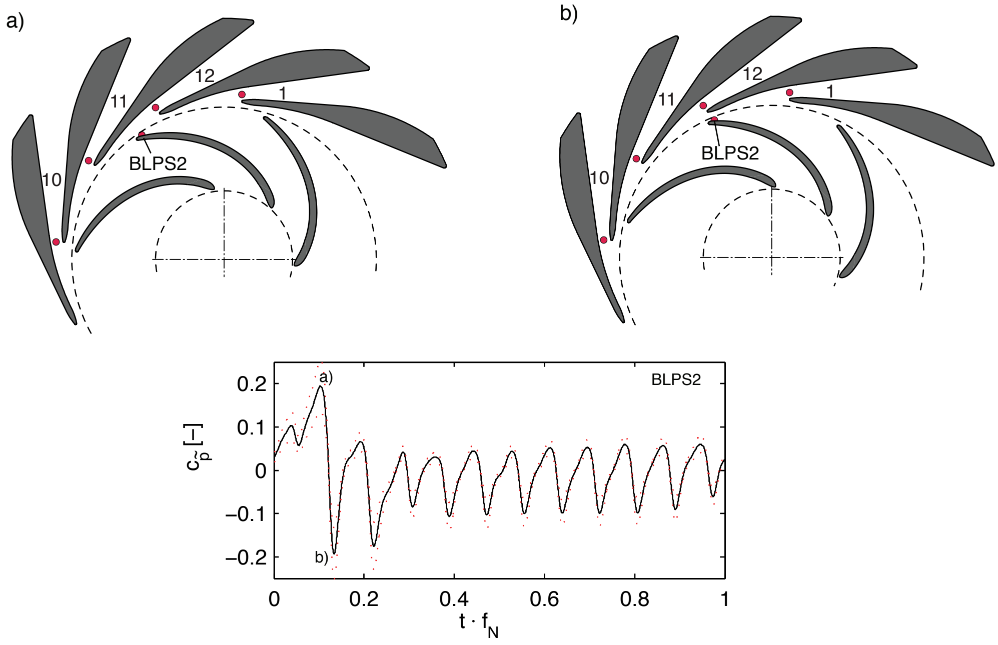

Figure 8.6: Relative position of impeller and diffuser at maximum and minimum impeller pressure

The pressure reduction due to the passage of the impeller blade along the suction surface of the diffuser vane separating the diffuser channels 11 and 12 is much less pronounced than for the other vane passages. Here, the local minimum pressure remains even higher than the maximum pressure for the diffuser channels without separation. This indicates, that only few liquid is passing the suction surface of the diffuser vane separating diffuser channel 11 and diffuser channel 12. The passage of the pressure sensor along the suction surface of the diffuser vane between diffuser channel 1 and diffuser channel 2 shows also lower pressure values than the remaining diffuser channels, indicating that the flow in diffuser channel 1 is also disturbed to some extend.

The presence of flow separation significantly affects the pressure fluctuations experienced by the diffuser throat. Figure 8.7 depicts the normalized phase average and the normalized amplitude spectra in the consecutive diffuser channels 10, 11, 12 and 1. While

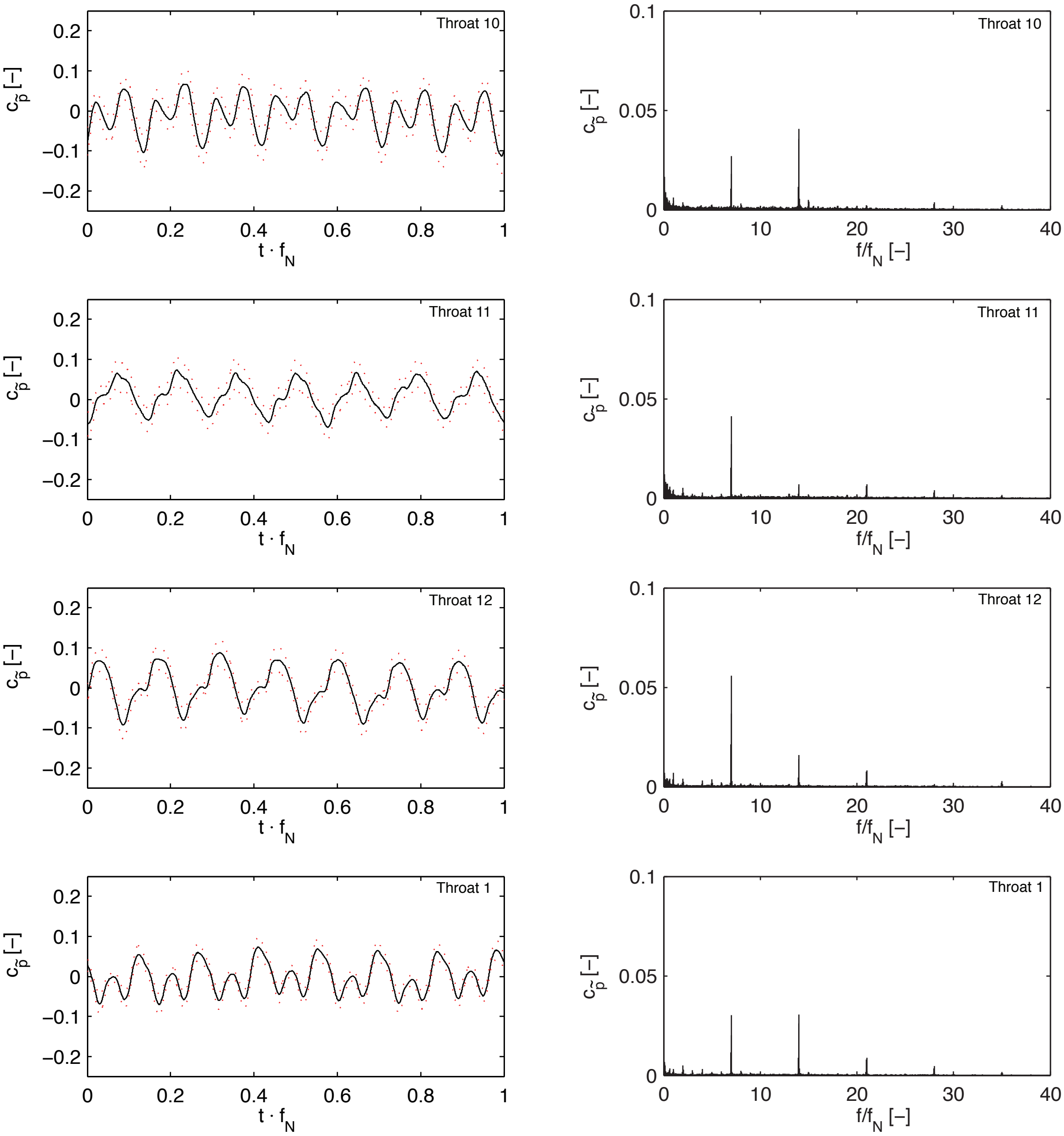

Figure 8.7: Diffuser pressure fluctuations in stalled and unstalled diffuser channels

in channel 10 and channel 1 a normal, relatively undisturbed flow yields regular pressure fluctuation patterns due to jet-wake interaction ($f/f_N = 7$) and potential interaction ($f/f_N = 14$), in the stalled channel 11 and channel 12, the pressure fluctuations due to potential interaction are nearly suppressed, while the jet-wake interaction strongly increases. This indicates a change of the pressure distribution around the diffuser vanes in the region of its its leading edges, since the local velocity here is modified by the stall cell.

8.1.3 Side Room Pressure Fluctuations

As outlined in section 6.3, the stationary stall affects the mean flow in the side rooms by a strong reduction of the flow rotation. Furthermore, close to the stall cell, the pressure fluctuation spectra are modified in a similar way as observed in the diffuser throat. Figure 8.8 presents the estimated pressure fluctuation spectra in two circumferential positions in the side room at the impeller outer diameter. While the sensor, analyzed in Figure 8.8a is located far from the stall cell, the second sensor (Figure 8.8b) is situated close to the diffuser channels exhibiting stall. Figure 8.9 compares the relative phase between the side room pressure sensors at the design point and at the presence of stall.

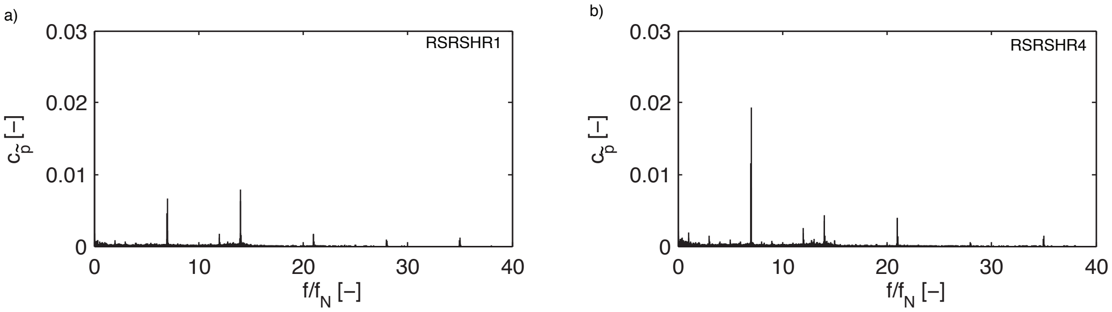

Figure 8.8: Side room pressure fluctuations at part-load and at different circumferential positions

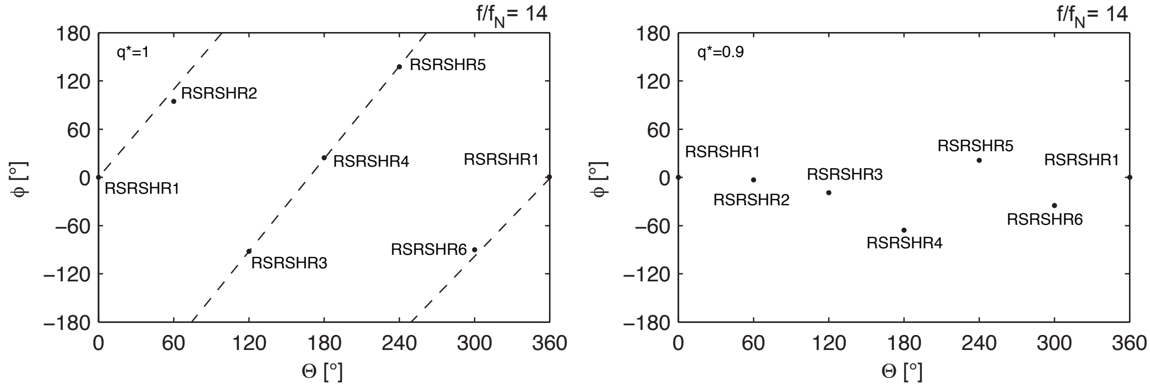

Figure 8.9: Circumferential distribution of relative phase of side room pressure fluctuations at $f/f_N = 14$

From this it can be concluded, that the presence of stall also affects the formation of pressure waves due to Rotor-Stator interaction in the side rooms and by this the pressure difference and the net force acting on the impeller hub and shroud side walls.

8.2 Rotating Diffuser Stall

8.2.1 Impeller Pressure Fluctuations

At specific part-load flow rates, the stall cells in the diffuser start to rotate. The number of stall cells depends on the relative flow rate.

The presence of stall cells, as well as their rotation can be detected using the pressure sensors embedded in the impeller outlet. Figure 8.10 depicts a waterfall plot of the pressure fluctuations, acquired in the impeller trailing edge pressure fluctuations. The stall cell, present as a local maximum of the dimensionless static pressure, slowly rotates in the direction of the impeller rotation. At further reduced flow rates ($q^* = 0.6$), an increase of the number of separated zones, accompanied by a rise of its rotational speed can be observed. Below $q* = 0.6$, the stall cells appear and disappear rather unorganized and no specific patterns are identifiable.

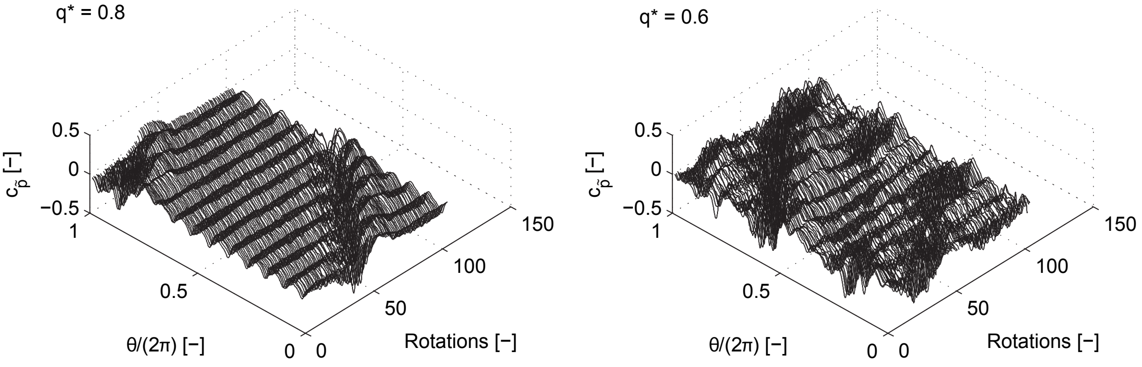

Figure 8.10: Rotating stall at different relative flow rates

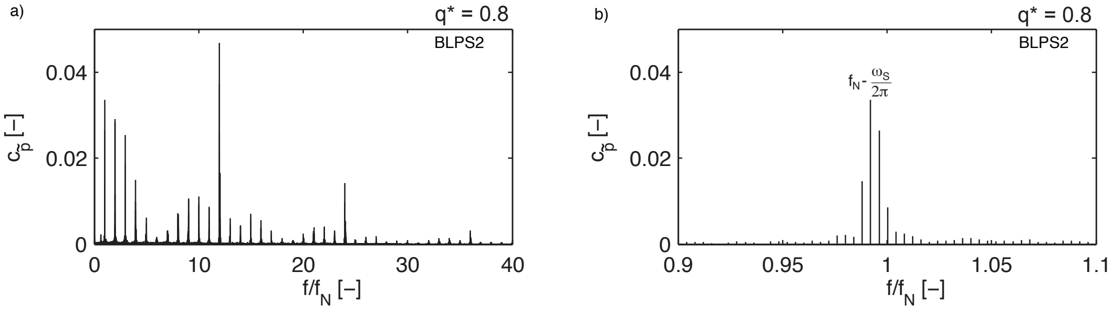

Figure 8.11: Amplitude spectrum of impeller pressure fluctuations in the presence of stall

In the frequency domain, the propagation of the stall cells yields additional pressure fluctuations at the frequency

$$f_{Stall} = f_N - \frac{\omega_s}{2\pi} \tag{8.1}$$

and its harmonics (Figure 8.11b). Furthermore, the rotating (as well as the stationary) stall yields additional frequency lines in the pressure fluctuation spectra due to a modulation with the RSI-frequencies (Figure 8.11a).

An evaluation of the pressure fluctuations using a phase lock average using the rotational frequency as a base periodicity, would yield completely misleading results, since all phenomena, having frequencies which are not integer multiples of the rotational frequencies, are suppressed by the averaging process. Therefore, the phase averaging method, discussed in section 5.4 will be applied to the pressure fluctuation data when rotating stall is present.

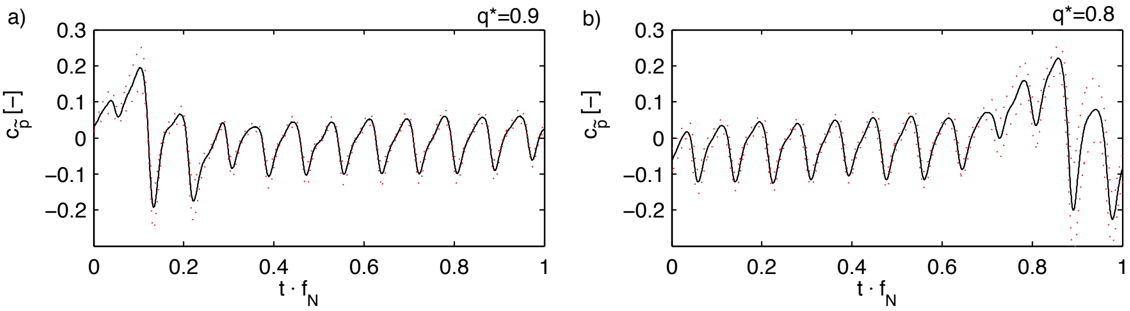

Figure 8.12: Comparison of pressure fluctuations with stationary (a) and rotating (b) stall being present.

Figure 8.12 presents a comparison between the phase averaged pressure fluctuations in the impeller trailing edge pressure surface at the presence of stationary (a) and rotating (b) stall. The maximum and minimum pressures are of comparable magnitude, again limited by the stagnation pressure. The impact of the stall cells, being it rotating or not, is comparable and the rotation of the stall cells, especially as they are rotating with a very low speed, is not changing the interaction between pressure fluctuations and mechanical phenomena in the impeller in a significant way.

8.2.2 Diffuser Pressure Fluctuations

Figure 8.13 depicts the pressure fluctuations in the vaned diffuser of the model pump at a position close to the rotor-stator interface at a relative flow rate of q*=0.8. At this flow rate, one stall cell is slowly propagating in the same direction as the impeller rotation (see Figure 8.10). The waterfall plot of the dimensionless pressure fluctuations in the diffuser clearly exhibits the passage of the stall cell as a strong increase of the pressure during 20 impeller rotations. This increase repeats after 140 impeller rotations, when the stall cell finished one revolution. Figure 8.14 shows the ensemble averaged pressure fluctuations in one of the diffuser throats.

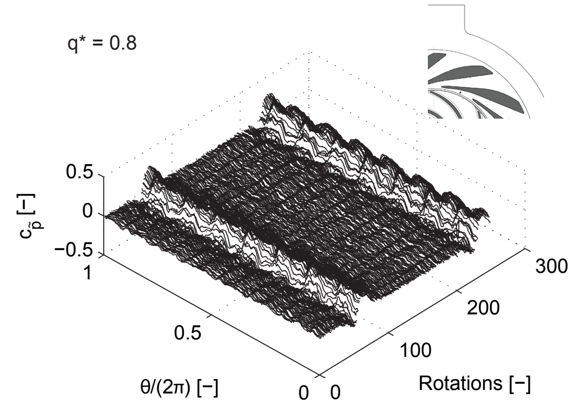

Figure 8.13: Diffuser pressure fluctuations close to Rotor-Stator interface

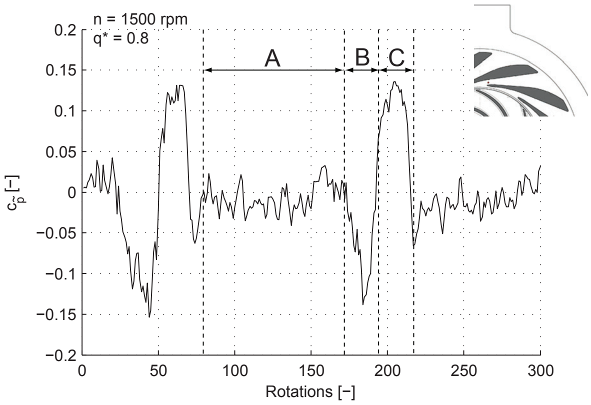

Figure 8.14: Low frequency pressure fluctuations in diffuser throat

This ensemble average has been calculated as the average of $c_{\tilde{p}}$ for each impeller revolution. Three different zones can be observed in the dimensionless pressure plot:

A Normal, undisturbed flow

B Pressure locally reduced due to the deviation of flow from the neighboring diffuser channel (in the direction opposite to the rotational direction), which increases the flow rate for the observed diffuser channel

C Pressure locally increased due to the stall of the diffuser channel (flow rate through this diffuser channel is nearly zero or even negative)

These perturbations in the pressure fluctuations extend into the rotor-stator interaction zone, affecting the frequency content of the pressure fluctuations experienced by the impeller.

Figure 8.15 shows the passage of the stall cell and the evolution of the low-pass filtered pressure fluctuations for one diffuser channel. While the diffuser channel operates in zone B, the higher nominal flow rate for this channel increases significantly the pressure difference between diffuser throat and diffuser outlet. When the diffuser channel gets stalled, the pressure difference between diffuser throat and diffuser outlet is strongly reduced, moreover, inside the diffuser channel, between the diffuser channel center (VCD) and the diffuser outlet (VOC), no pressure recovery is anymore present. This indicates, that no organized throughflow exists, when flow separation is present in the diffuser channel.

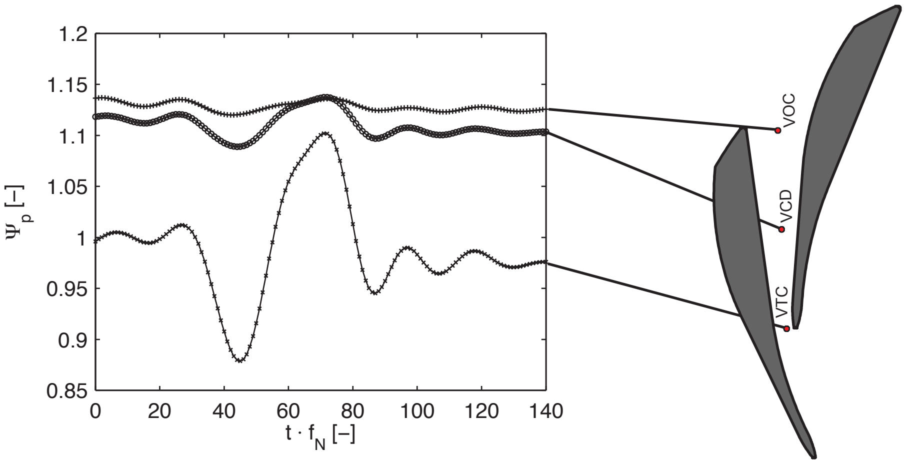

Figure 8.15: Low-pass filtered diffuser wall pressure during stall passage

8.2.3 Side Room Stall Passage Observations

The rotation of the stall cells allows an evaluation of the effect of diffuser stall on the pressure distribution in the hub and shroud side rooms. Figure 8.16 presents the low-pass filtered pressure fluctuations at two pressure sensors embedded in the hub and shroud side room at identical angular positions.

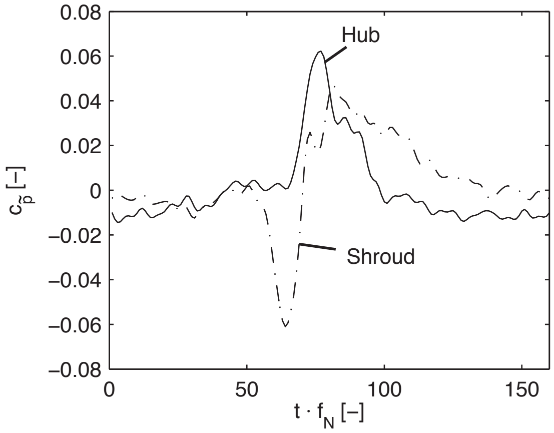

Figure 8.16: Low-pass filtered diffuser wall pressure during stall passage

While the shroud side room pressure sensor expresses the passage of a low pressure zone, followed by the passage of a high pressure zone, as it was observed in the impeller outlet, the diffuser throats and in the sensor arranged close to the Rotor-Stator interface, the hub side room pressure sensor exhibits only the high pressure zone, no reduction of pressure is distinguishable before the increase of pressure due to the presence of stall.

This can be explained by the formation of a recirculation zone at the impeller outlet as illustrated in Figure 1.6c. The recirculation zone at the impeller outlet hub changes the pressure distribution around the diffuser vane inlet, reducing the pressure drop at its suction surface, while the flow at the impeller shroud maintains it general pattern, thus leading a strong reduction of the pressure at the diffuser vane suction surface.

When the stall is fully developed in the diffuser channel, the pressure increases nearly synchronously at hub and shroud, indicating that the stall affects the whole diffuser channel from hub to shroud in a comparable way.

8.2.4 Stall Rotation in Stationary Domain

Figure 8.17 depicts the stall cell position for the case of one rotating cell as a function of the number of impeller rotation.

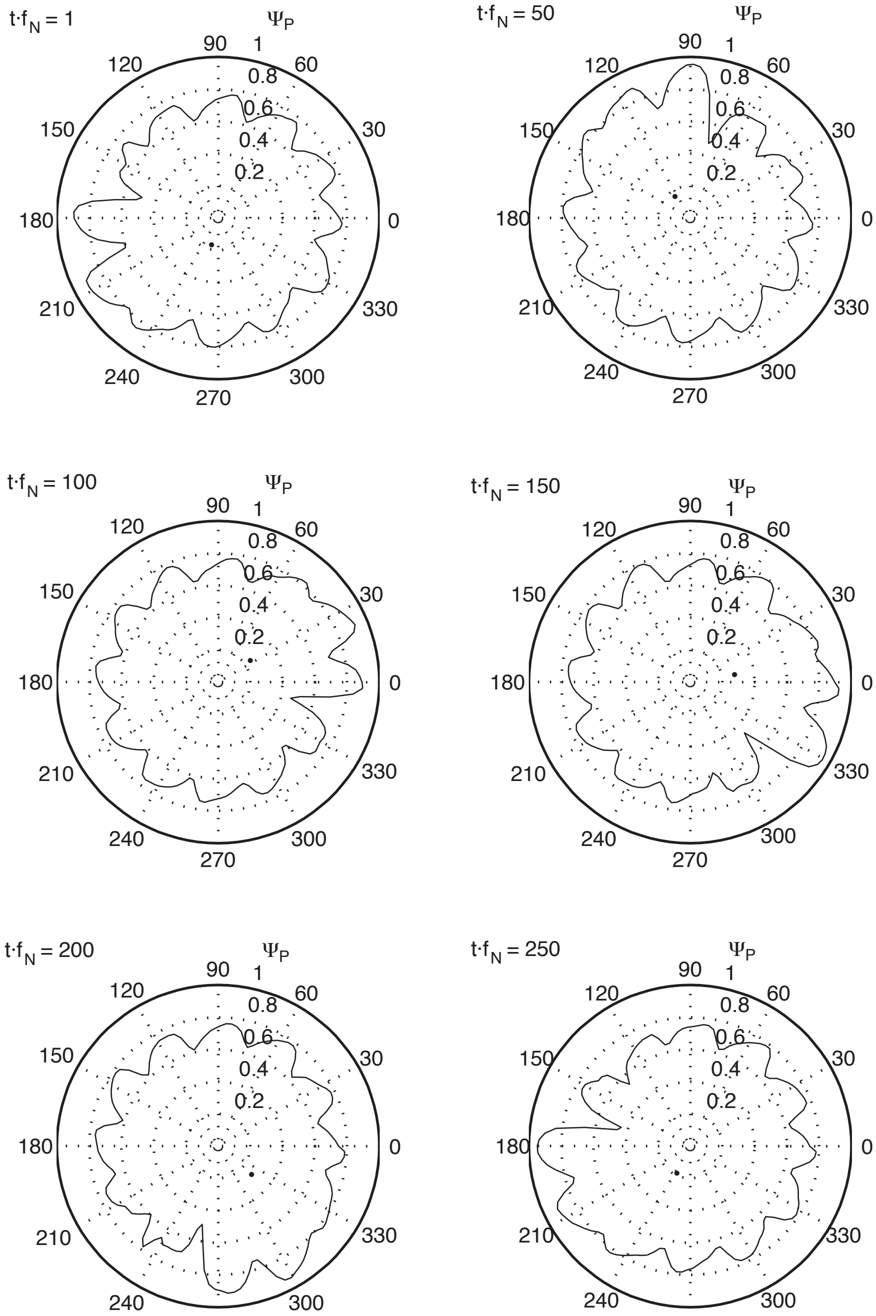

Figure 8.17: Stall cell position at different rotation numbers

The stall rotational speed can be estimated from the rotating domain pressure fluctuation measurements in the following way: as the stall expresses itself as a high pressure zone, observed during each impeller revolution, its angular velocity can be easily obtained from

$$\omega_S = \frac{d\phi_S}{dt} \tag{8.2}$$

The angular position of the stall cell can be calculated as the position of the center of gravity of a surface defined by the circumferential blade outlet pressure distribution during one revolution of the impeller using the relations

$$x_{s,p} = \frac{1}{A}\int_A x dA \qquad y_{s,p} = \frac{1}{A}\int_A y dA \qquad \phi_S = atan\frac{y_{s,p}}{x_{s,p}} \tag{8.3}$$

Figure 8.18 presents the stall cell phase angle as a function of the number of impeller revolutions for 1000 impeller rotations. While the impeller performs 1000 revolutions, the stall cell performs 5 revolutions. The stall rotational speed is not constant, a variation during each revolution of the stall cell can be observed. At certain circumferential locations the stall propagation is visibly decelerated.

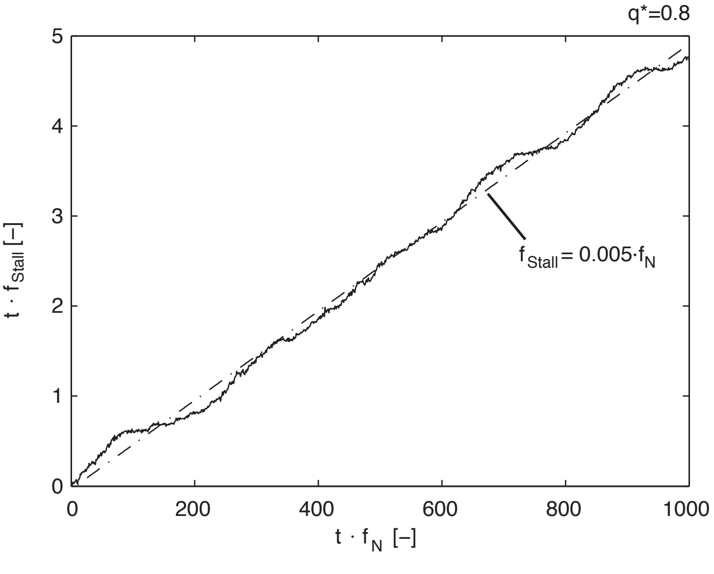

Figure 8.18: Estimation of stall rotation velocity from circumferential pressure distribution

The mean propagating speed is estimated as the slope of least square fit on a linear curve calculated for 1000 impeller revolutions, for the analyzed case at q*=0.8, where one stall cell is present. This stall cell rotates with 0.5% of the impeller rotational speed.

Figure 8.19 presents a comparison of the measured diffuser stall propagation speed with published experimental results. The data published so far show a general tendency of increasing stall propagation speed with increasing radial gaps between impeller trailing edge and diffuser leading edge. A possible explanation could be given by the flow pattern in the vaneless gap between the impeller trailing edge and the impeller leading edge. The flow leaves the impeller with an absolute velocity c_2, having an absolute flow angle of α_2. In the vane-less gap the flow is assumed to follow a logarithmic spiral having the velocity components

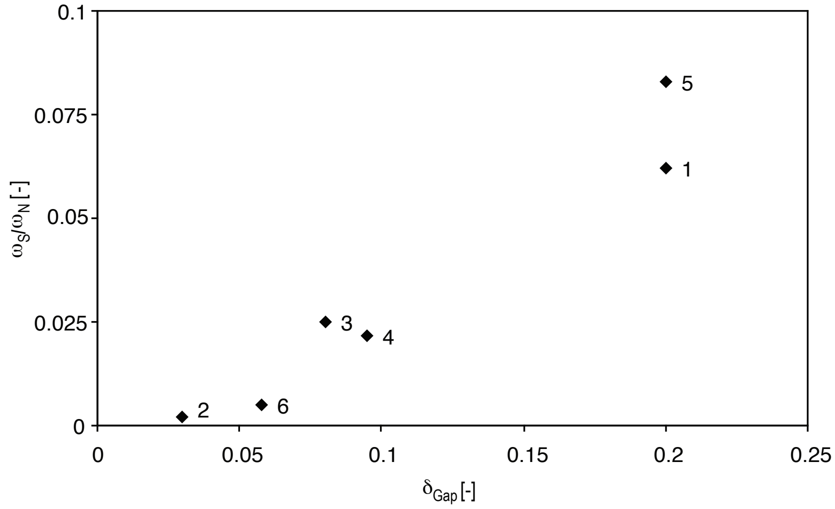

1 ... Sinha et al. [119]
2 ... Wang and Tsukamoto [136]
3 ... Yoshida et al. [139]
4 ... Braun [15]
5 ... Miyabe [90]
6 ... Present experiment

Figure 8.19: Comparison of measured stall propagation speed with published values

$$c_{u,r} = c_{u,2} \cdot \frac{r_2}{r_3} \tag{8.4}$$

and

$$c_{r,r} = c_{r,2} \cdot \frac{r_3}{r_2} \tag{8.5}$$

The flow angle at the diffuser vane leading edge is defined as

$$\alpha_{3,i} = atan\left(\frac{c_{r,3i}}{c_{u,3i}}\right) = \delta_{Gap}^2 \cdot \alpha_2 \tag{8.6}$$

This equation expresses a square relation between the impeller outlet flow angle variations and the resulting diffuser incidence angle variations and helps to explain the relation between the observed stall rotational velocities shown in Figure 8.19.

Chapter 9

Analysis of Impeller Mechanical Response to Observed Pressure Fluctuations

9.1 Impeller Deformation Due to Rotor-Stator Interaction

The RSI pressure fluctuations act as an excitation source of impeller vibrations. When no stall is present, the impeller performs forced vibrations where the frequency as well as the associated mode shape are imposed by the pressure fluctuations experienced by the impeller.

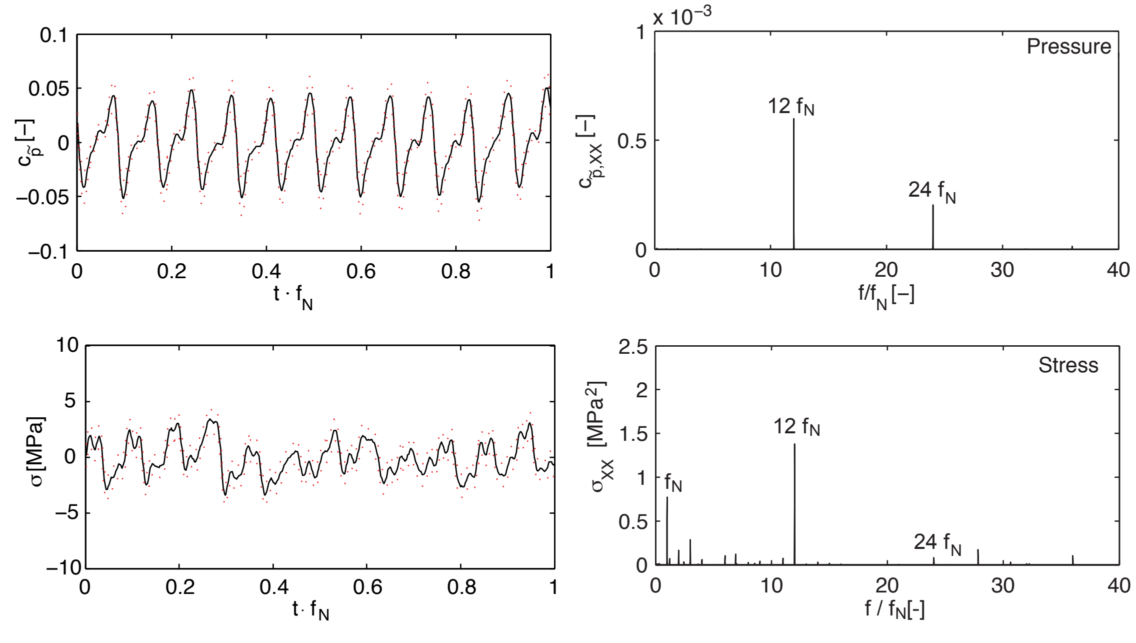

Figure 9.1: Phase average and auto-power spectrum of pressure pulsations and strain at one circumferential impeller position

Figure 9.1 depicts the phase averaged pressure fluctuations and mechanical stresses, as well the estimated associated power spectra for one pressure sensor embedded in the impeller shroud at the external diameter and its neighboring strain gauge. The measured deformations at design conditions unveiled periodic stress variations at the rotational frequency and at multiples of it, which are equivalent to the Rotor-Stator Interaction pressure fluctuation frequencies.

Figure 9.2 shows the coherence between the pressure fluctuations and strain, measured using a strain gauge close to the analyzed pressure sensor. The coherence function, which can be interpreted as a measure for the linear dependence of an output signal (here the impeller stress) on an input signal (in this case the pressure fluctuations) as a function of frequency. Very high coherence values are found at the diffuser vane passage and its harmonics, indicating that the impeller deformation is mainly caused by the RSI pressure fluctuations.

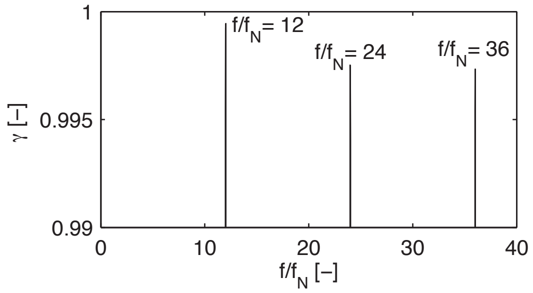

Figure 9.2: Coherence between pressure fluctuations and impeller strain

The shroud deformations at the rotational frequency are not coherent to the pressure fluctuations, these deformations are caused by the mechanical imbalance of the impeller.

An analysis of the relative phase angle of significant strain frequencies, measured at different circumferential positions distributed at the impeller outer diameter, allows the identification of rotating deformation patterns, which are generated by the rotor-stator interaction. Figure 9.3 depicts the phase analysis for the diffuser vane passage frequency.

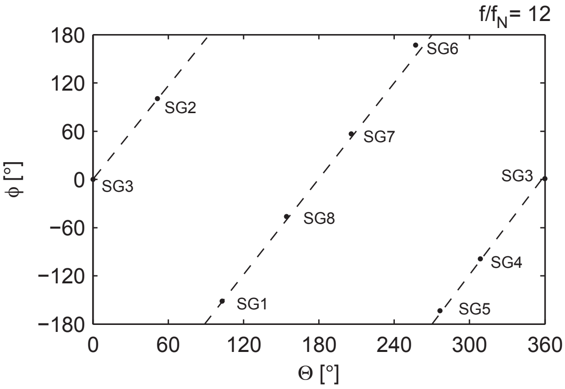

Figure 9.3: Relative phase of impeller strain at Rotor-Stator interaction frequency

Recalling Figure 7.11, which represents the phase relations for pressure sensors neighbored to the analyzed strain gauges, the direct relation between the Rotor-Stator Interaction induced pressure fluctuations and the impeller deformation gets immediately apparent.

Figure 9.4 outlines the impeller deformation at the diffuser vane passing frequency. This deformation pattern can be only induced by a periodic variation of the axial net force acting on the impeller hub and shroud.

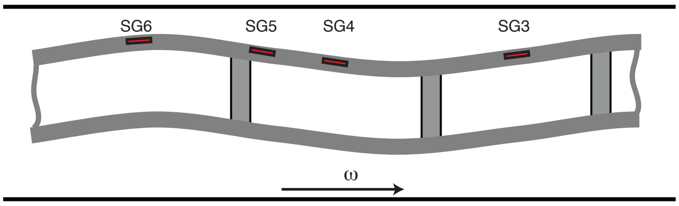

Figure 9.4: Impeller deformation pattern at diffuser vane passing frequency

This axial net force is mainly imposed by the different transmission of the RSI pressure fluctuations into the hub and shroud side rooms as well as the differences in the development of the pressure distribution in the side rooms, depending on the radial through flow (see chapter 1.2) in the hub and shroud side room.

9.2 Effect of Uneven Pressure Distribution Due to Flow Separation

The presence of flow separation in the diffuser changes the impeller deformation patterns significantly. As the impeller passes the high pressure zone due to the flow separation, a strong deformation is superposed on the RSI related deformation pattern. Figure 9.5 presents pressure fluctuations and shroud deformation at the impeller external diameter with stationary and rotating stall being present in the diffuser.

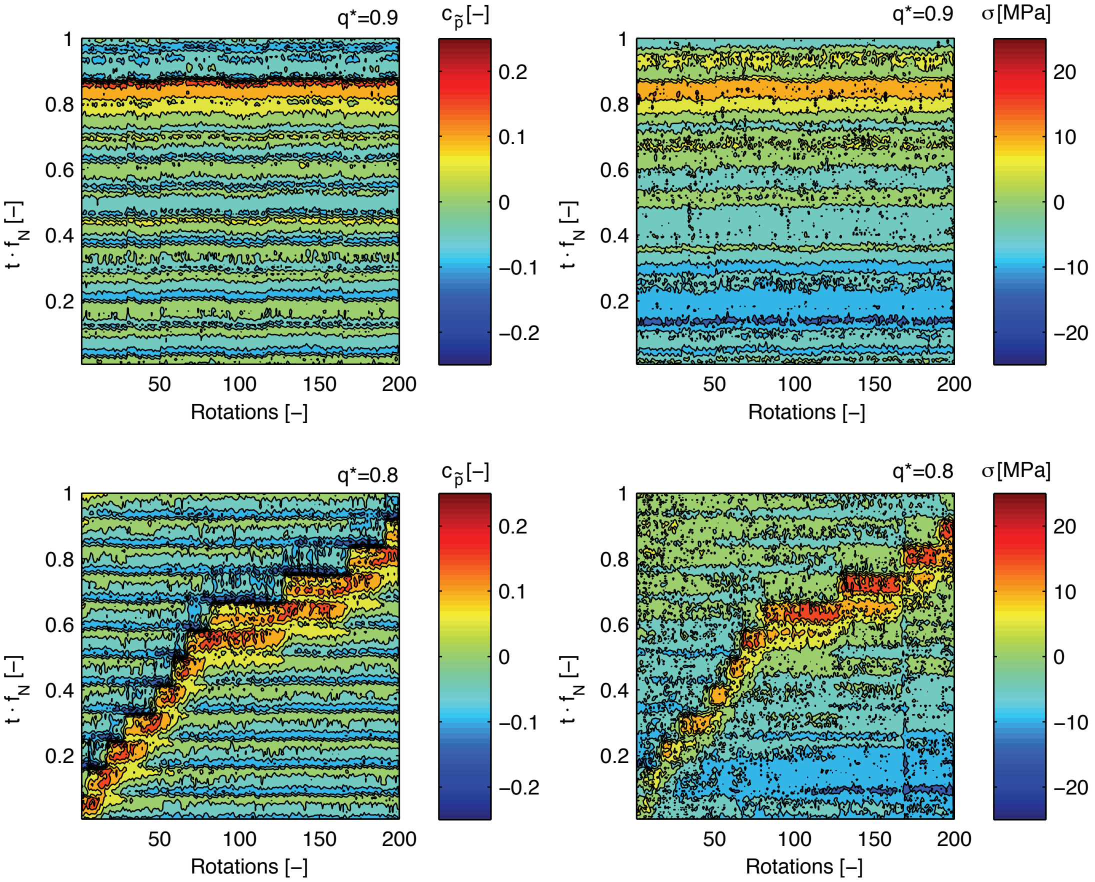

Figure 9.5: Pressure fluctuations and impeller deformations with stationary and rotating stall

The passage of the stall cell is recognizable in the pressure trace as well as in the deformation plot. Moreover, the deformation is visibly directly linked to the pressure values, obtained by the pressure sensor, located in the vicinity of the strain gauge. This illustrates, that the deformation is imposed by the locally increased pressure difference between the pressure inside the impeller and in the side room.

Figure 9.6 presents the phase averaged pressure fluctuations and the associated shroud deformations for one impeller channel. Already from this figure it can be immediately concluded, that the impeller channel is deformed individually and not following the RSI pattern imposed on the whole impeller, as it this the case for the RSI related impeller deformations.

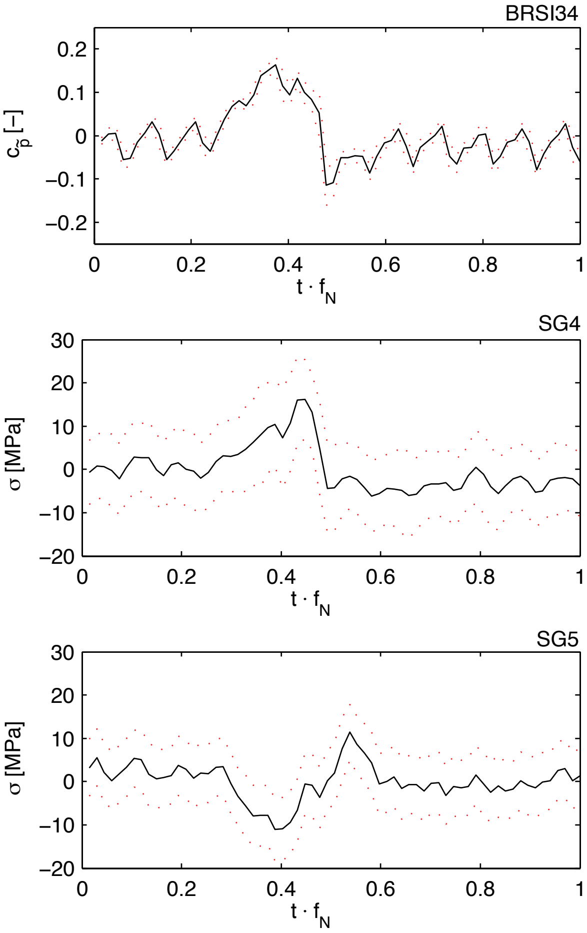

Figure 9.6: Impeller deformation in the presence of stall

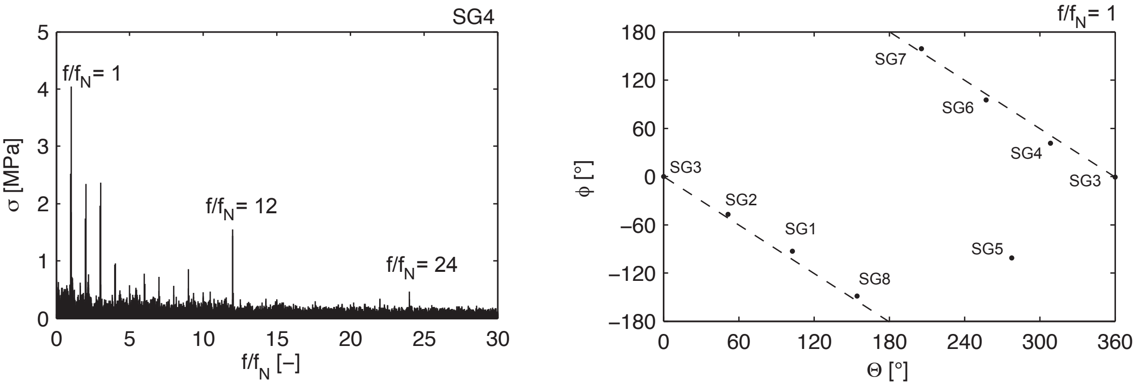

Figure 9.7: Amplitude spectrum for one strain gauge and relative phase of impeller strain at Rotor-Stator interaction frequency

An analysis of the relative phase for the circumferentially distributed strain gauges at the stall frequency (Figure 9.7) expresses exactly the same relations. As it can be seen here, the strain for the strain gauge embedded close to the impeller blade (SG5), is expressing the opposite phase as the strain gauge between two impeller blades (SG4), showing the individual deformation of the impeller shroud, channel by channel.

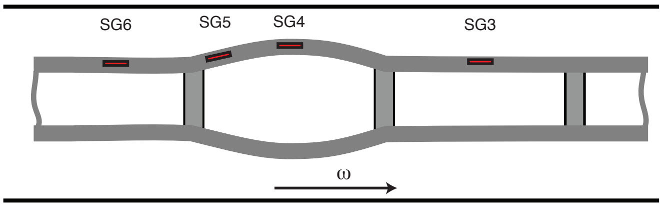

Figure 9.8: Impeller stress in the presence of stall

Finally, the deformation shape of the impeller can be estimated as shown in Figure 9.8. When the strain gauge in the center of the channel between two blades (SG4) is loaded by tension, the strain gauge arranged close to the impeller blade (SG5) is compressed. The amplitude of this deformation is significantly higher, than the deformation due to RSI pressure fluctuations and represents at part-load the main source of impeller deformations.

Chapter 10

Shaft Vibration Observations

10.1 Shaft Vibrations at Design Conditions

The model pump used for the experiments has been equipped with hydrodynamic radial and axial bearings, which have to accommodate the steady and unsteady radial and axial forces resulting from the different operational regimes of the pump.

Appendix A briefly summarizes the operating principle and important definition for hydrodynamic bearings. The shaft position during the pump operation is defined by the equilibrium between the mechanical and hydraulic forces acting on the rotor and the hydrodynamic forces in the bearing clearance between the shaft journal and the bearing wall, which depend on the eccentricity of the shaft. Therefore, any variation in the rotor forces results in a displacement of the rotor.

The hydraulic radial force in a centrifugal pump with a vaned diffuser operating at design conditions is nearly zero (see Figure 1.11). In this case the shaft centerline is displaced in function of operational regime of the bearing. Figure 10.1 presents the shaft centerline location, calculated as the averaged proximity per revolution in x and y direction as depicted in Figure 4.12.

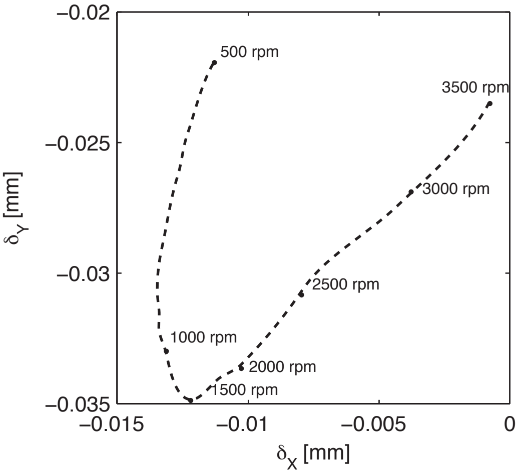

Figure 10.1: Shaft centerline position as function of rotational speed

At very low angular velocities the shaft centerline follows the bearing shape, as the shaft touches the bearing and operates in the state of boundary lubrication. With increasing rotational speed, a liquid film between shaft and bearings grows until the bearing is operating in the regime of fully hydrodynamic lubrication. Here, the shaft displacement in function of the rotational speed is the result of the increasing pressure in the gap between the shaft and the bearing due to the increasing angular velocity. The mechanical unbalance generates a constant radial force rotating with the angular velocity of the shaft, displacing the shaft journal in the bearing. This can be observed in the shaft vibration spectra (Figure 10.2), which are dominated by vibrations at the rotational frequency.

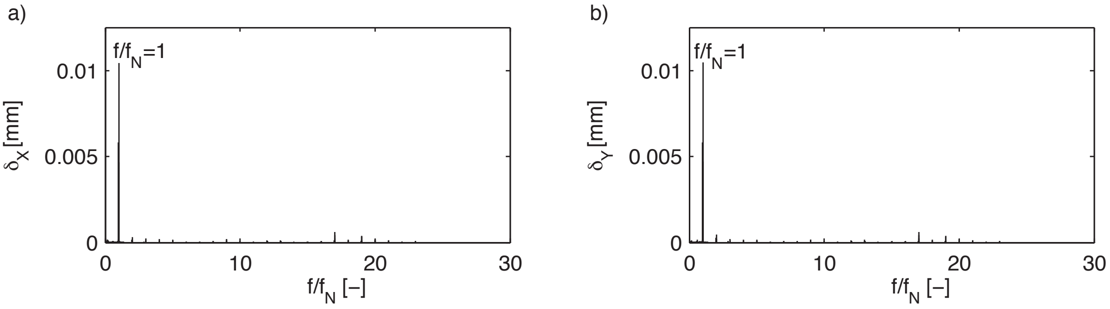

Figure 10.2: Shaft vibration spectra in X direction (a) and Y direction(b)

A constant force, rotating with the angular velocity shaft would result in a circular shaft orbit.

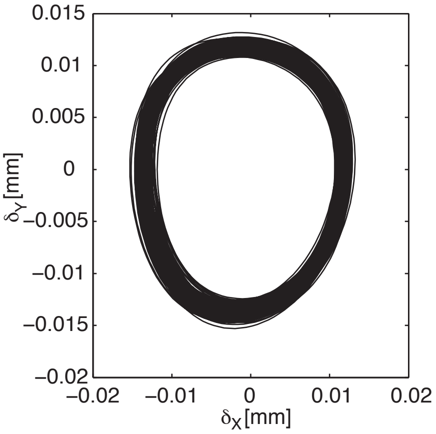

Figure 10.3: Shaft orbit at best efficiency flow rate

Circumferential anisotropy in the bearing stiffness deforms this theoretically circular orbit into an elliptic orbit as shown in Figure 10.3.

10.2 Shaft Precession due to Rotating Instability

Apart of the impeller deformations an important consequence of the rotating high pressure pattern is is a slowly rotating radial net force acting on the impeller [62]. This radial force displaces the shaft journal significantly and strongly changes the observed shaft orbit.

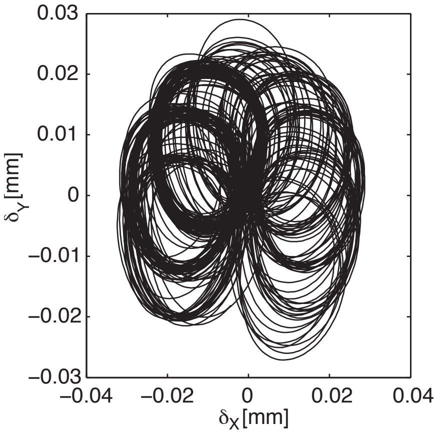

Figure 10.4: Shaft precession due to unsteady radial pressure distribution

A comparison of the shaft centerline position as a function of the number of impeller revolutions with the associated stall cell position, estimated as shown in 8.2.4 demonstrates the relation between shaft vibrations and the location of the stall cell (Figure 10.5).

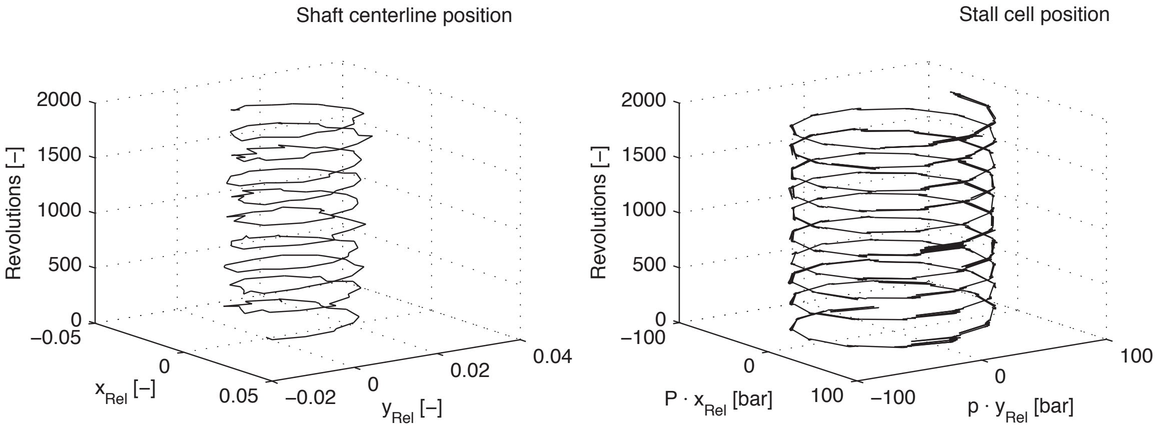

Figure 10.5: Position of shaft centerline and stall cell with rotating stall

As the stall cell propagates, the radial net force due to the high pressure zone imposes a subsequent displacement of the shaft centerline. This can be illustrated as shown in Figure 10.6, where the shaft centerline position is compared with the application point of radial force estimated as explained in Section 8.2.4.

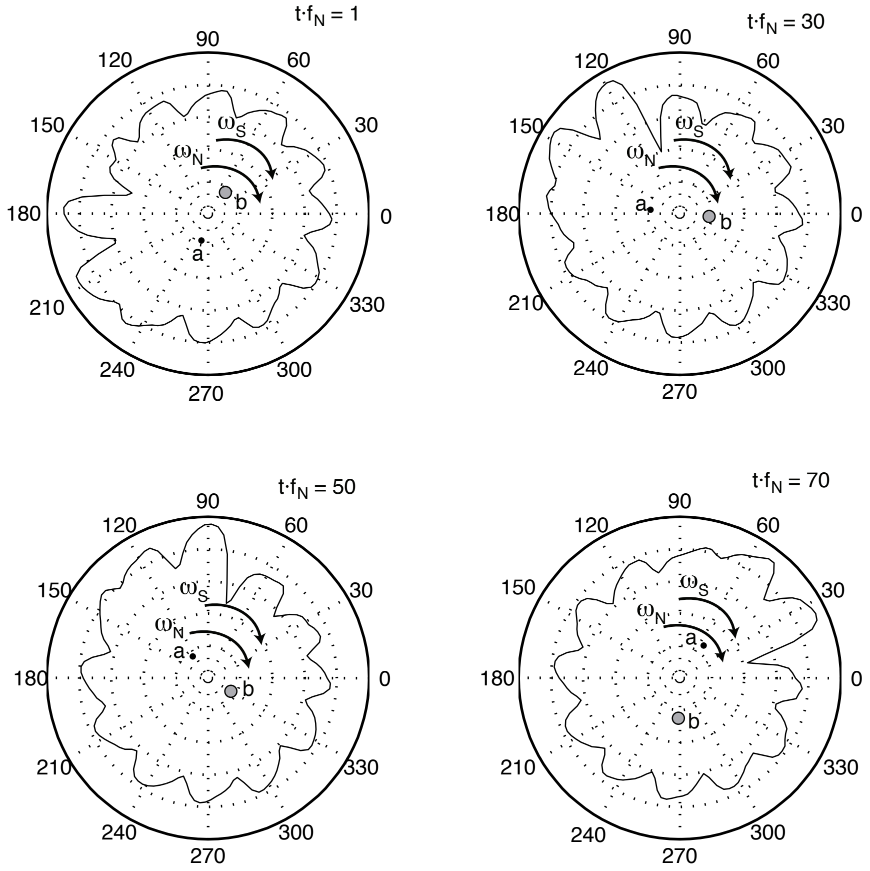

Figure 10.6: Position of point of application of radial net force (a) and shaft centerline (b) due to rotating stall

The cross-power spectrum, as well as the coherence function between a pressure sensor embedded in the impeller blade close to the trailing edge and one of the proximity sensors confirm the relation between stall rotation and shaft displacement (Figure 10.7).

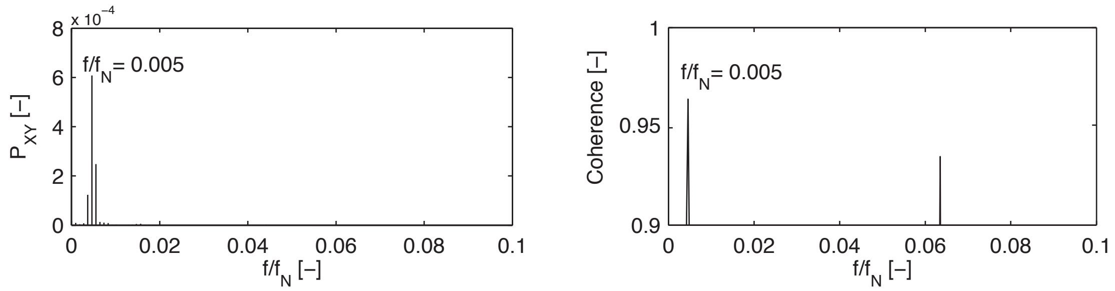

Figure 10.7: Cross-power spectrum and coherence between impeller blade pressure sensor and shaft proximity sensor

Depending on the rotational velocity of the stall cell, the sub-synchronous shaft vibration, resulting from the non-uniform circumferential pressure distribution, might harmfully affect the behavior of the entire rotor system, leading to rotordynamic instabilities.

10.3 Effect of Flow Separation on Axial Shaft Vibrations

Figure 10.8 presents the estimated amplitude spectra of the shafts axial vibrations, measured using a proximity probe at the pumps non-drive end. The spectra are dominated by an oscillation at the rotational frequency. This is not a purely axial vibration, as the shaft position has been measured as the distance between the proximity sensor and a steel disk mounted at the onboard date acquisition system (see Figure 4.13), any non-perpendicularity to the shaft axis would result in a variation of the distance between the sensor and the disk at the rotational frequency. The higher order oscillations are therefore more significant and might be related to hydraulic phenomena.

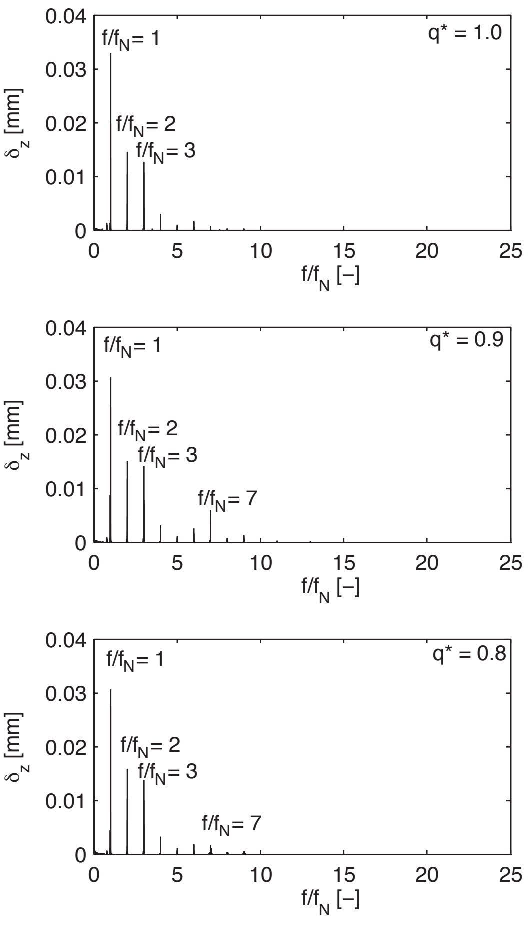

Figure 10.8: Axial shaft vibration spectra at different operating points

As it can be seen in Figure 10.8, the amplitudes up to the third harmonic of the rotational frequency are unaffected by the reduction of the relative flow rate, but with the appearance of a recirculation zone in the diffuser, additional vibrations at the impeller blade passing frequency occur. The amplitudes are largest, when the stall is stationary (at q*=0.9). When the stall cell starts to propagate, the amplitude of the axial shaft vibrations at the impeller blade passing frequency is significantly reduced.

The additional vibrations at the impeller blade passing frequency are the result of an interaction of the impeller pressure fluctuations with the stall cell and the impact of it on the side room flow. Each time an impeller blade passes the the stall cell, a change of the axial net force imposes an axial displacement of the rotor. This can be traced in the amplitude spectrum of the axial vibrations, the stationary stall is visible as an amplitude increase at the blade passing frequency.

When the stall cell is rotating, axial vibrations at the stall rotational frequency can be observed. These axial vibrations are coherent with the stall cell rotation (Figure 10.9).

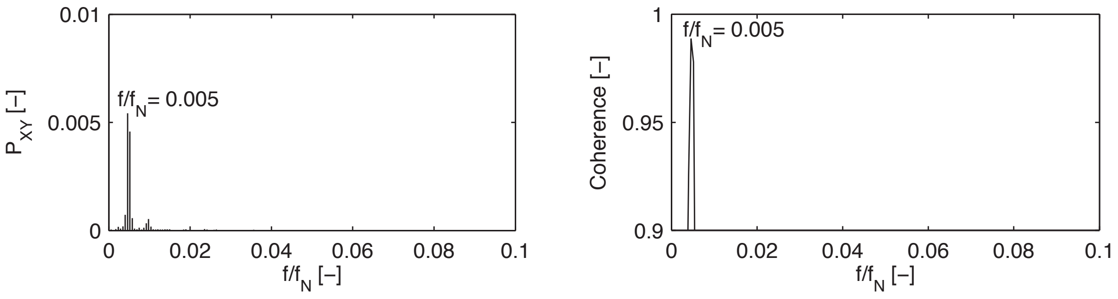

Figure 10.9: Cross-power spectrum and coherence function between side room pressure and axial shaft vibrations

The axial shaft vibrations exhibit the presence of stationary and rotating flow separations in the diffuser due to the modification of the side room flow as well as of the axial net force by the passage of the impeller blades through the stall cell. The oscillating axial net force acting on the impeller is resulting in a periodic displacement of the shaft at the blade passing frequency and, in the case of rotating stall, at the rotating frequency of the stall cells.

Part III

Conclusions and Perspective

Chapter 11

Conclusions and Perspective

11.1 Conclusions

An experimental study with the objective of an evaluation of the excitation of impeller deformations by hydrodynamic phenomena in a centrifugal pump, operating at part-load, has been performed using a single stage, high speed model pump. The model pump, operating at rotational speeds up to 5'500 rpm, has been equipped with a radial impeller having seven blades and a vaned diffuser with twelve stationary vanes.

The model pump has been instrumented with 81 piezo-resistive pressure sensors, 8 strain gauges and 3 accelerometers, distributed in the impeller, vaned diffuser and the annular collection chamber. The relative motion between pump shaft and bearing housings in axial and radial direction has been measured using 3 eddy current proximity sensors.

The pressure and deformation data in the rotating domain have been acquired and processed using an onboard data acquisition system, specifically designed for the intended experiments. The onboard data acquisition system has been directly mounted on the shaft non-drive end, the processed data have been transmitted to the stationary domain using a high-speed slip ring.

The measurement data have been acquired synchronously in the rotating and stationary domain, this has been ensured by the use of a simultaneous trigger signal for both data acquisition systems. A key phasor has been used to obtain an angular reference signal and to measure the rotational velocity of the pump shaft.

The measurements have been performed at different rotational speeds and relative flow rates ranging from overload to part-load. Depending on the actual flow regime, three different pressure fluctuation patterns have been observed during the measurements:

- Rotor-Stator interaction generated pressure fluctuations are dominant at the design flow rate.
- A stationary high pressure zone is observed at high part-load.
- The high pressure zone begins to rotate slowly at further reduced flow rates, eventually the number of rotating cells increases.

The pressure fluctuations were most intense close to the impeller outer diameter, where Rotor-Stator interaction occurs and quickly diminished upstream and downstream of this location. An analysis of the spatially distributed amplitudes and relative phases at the RSI frequencies and its harmonics unveiled the formation of rotating pressure waves with different numbers of nodes, which have been identified in the impeller as well as in the diffuser. These rotating pressure waves agree well with simplified models for the explanation of Rotor-Stator interaction phenomena, published by different authors. The Rotor-Stator interaction pressure fluctuations were transmitted also in the side rooms between impeller hub and shroud and the stationary casing walls.

The Rotor-Stator interaction pressure fluctuations create a periodic load on the stationary and rotating components in the pump stage, which cause subsequent deformations and vibrations. Strain measurements in the impeller, using spatially distributed strain gauges, embedded in the impeller shroud, show moderate impeller deformations at the design flow rate and above, which express the same frequency and phase relations as the pressure fluctuations due to Rotor-Stator interaction.

At part load, when flow separation occurs in the diffuser, the deformation pattern of the impeller shroud changes significantly. When a strain gauge passes the high pressure zone, caused by the flow separation in the diffuser, a large deformation is observed at the measurement location. This deformation is more than twice as big as the deformation caused by the RSI pressure fluctuations and by far dominates the deformation spectra, estimated from these data. An analysis of the relative phase of the strain gauges, including one specific strain gauge, embedded close to an impeller blade, shows that the deformations due to the separation are imposed on each impeller channel individually, while the deformations caused by RSI were independent of the relative locations of impeller blades and strain gauges, since the impeller shroud deformation follows exactly the excitation imposed by the Rotor-Stator interaction pressure fluctuations.

The shaft vibration measurements exhibited the impact of part-load operation on the entire rotor system. With a stationary separation zone present, the axial shaft vibration measurements expressed a strong increase of vibration amplitudes at the impeller blade passing frequency, this indicates a strong transient variation of the side room flow rotation and the resulting axial force during the passage of an impeller blade through the separation zone located in the diffuser.

When the separation zone begins to propagate, the rotating radial net force vector causes a subsequent shaft centerline displacement. This shaft centerline displacement yields shaft orbits, which are not aligned anymore and bears a risk to provoke a rotordynamic instability of the rotor system.

11.2 Outlook

The performed experiments showed the importance of flow separations for the mechanical loading and dynamic behavior of centrifugal pumps. Flow separations are an inherent feature of the operational behavior of centrifugal pumps which arise already inside the operational limits of centrifugal pumps, this can be easily demonstrated by the incidence variation for the diffuser inlet, which corresponds within the typical operational limits of large centrifugal pumps ($q^*=0.6$ ..1.2) to 100% . No guide vane geometry is capable to cover such big incidence angle variations without expressing flow separation.

On the other hand, approaches to passively reduce the separation risk at off-design flow rates, as proposed for example by [111] or [73] usually deteriorate the machine's efficiency, since they are often based on an increase in local friction losses. These consequences are often undesirable, especially in high energy pumps, where highest efficiencies need to be achieved.

Active control of stall as a more efficient tool has been investigated in most of the cases for vane-less turbocompressor diffusers by injection of air ([27],[106], but also for the improvement of the part-load behavior of a mixed flow pump ([51]), had rather limited success.

Another active control attempt has been made by Paduano et al. [98] using inlet guide vanes performing vibrations controlled by individual actuators for each vane in in order to impose pressure fluctuations to the inflow, which reduced the intensity and onset flow rate of rotating stall in the analyzed compressor. A promising approach to affect flow separation appears to be the use of so called vortex-generator-jets [76], these have been applied to conical diffusers ([95],[63]) and led to significant performance improvements.

In the actual situation it appears to be more practical, to control the flow structure during the operation of high energy pumps and to avoid long term use of pumps in operating ranges, where drastic consequences as structural failures due to too high dynamic loading of rotating or stationary components appear to be imminent. Rotating flow separations can furthermore negatively affect the rotordynamic behavior of rotor systems, since the precessing movement of the shaft may generate destabilizing forces in the clearances and therefore reduce the damping and change the eigenfrequency of the rotor.

Apart of modifications of the hydrodynamic design of the pump components in order to shift the flow separation onset towards lower flow rates, a close monitoring of the machines operation with respect to the occurrence of flow separation is advisable and possible with the typically available instrumentation in high-energy machines. This kind of centrifugal pumps, often critical for the operation of rather complex technical installations as thermal power plants or oil exploration facilities are virtually always equipped with monitoring systems for shaft vibrations and bearing housing vibrations.

In the present work, a clear relation between the occurrence of hydrodynamic instabilities and the shaft displacement, arising from the dynamic variation of the radial and axial net forces has been demonstrated. This establishes the opportunity of creating a stall detection system using the available shaft vibration monitoring. The detection of a stationary detachment is more difficult, as it manifests itself not directly in pressure fluctuation or radial shaft vibration signals, but it can be detected by an increase of the axial shaft vibration levels at the impeller blade passing frequency.

Appendix

Appendix A

Hydrodynamic Bearings

The radial and axial forces, resulting from the centrifugal pump operation have to be accommodated by bearings. For large centrifugal pumps, these bearings are usually hydrodynamic bearings. The fundamental operating principle are briefly outlined in this section.

Figure A.1 shows the velocity and pressure distribution for a Newtonian fluid in a wedge with a moving and a stationary wall. The wall boundary condition imposes a relative velocity of zero between the fluid and the walls and the continuity requirement imposes the velocity and pressure distribution along the wedge. This pressure distribution can be described by the Reynolds equation for the laminar flow of an incompressible, Newtonian fluid, where shear is proportional to velocity

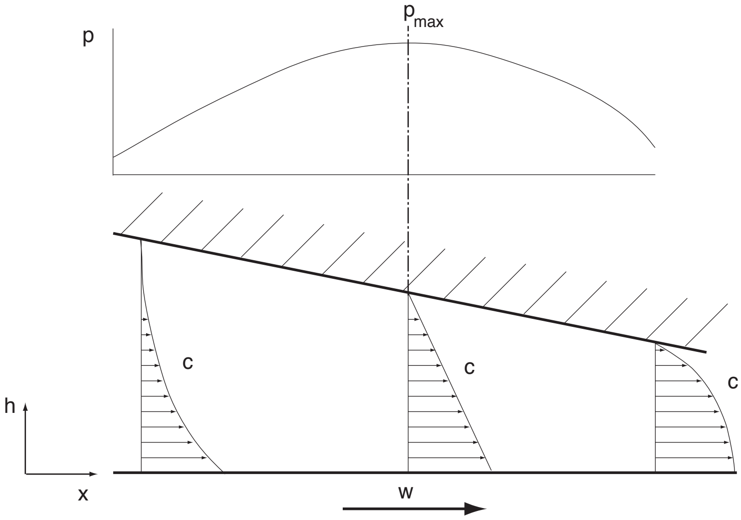

Figure A.1: Velocity and pressure distribution inside a wedge with a moving wall

$$\rho \frac{dc}{dt} = -\operatorname{grad} p + \eta \cdot \Delta c \tag{A.1}$$

and which describes the equilibrium between inertial forces (at the left side of equation (A.1)) and pressure and viscous forces (at the right side of equation (A.1)).

This fundamental principle finds its application in axial and radial bearings (Figure A.2). While the wedge in radial bearings (Figure A.2a) is given by the eccentricity of the shaft inside the bearing, axial bearings (Figure A.2b) can be equipped with tilt-able pads, defining each one another wedge.

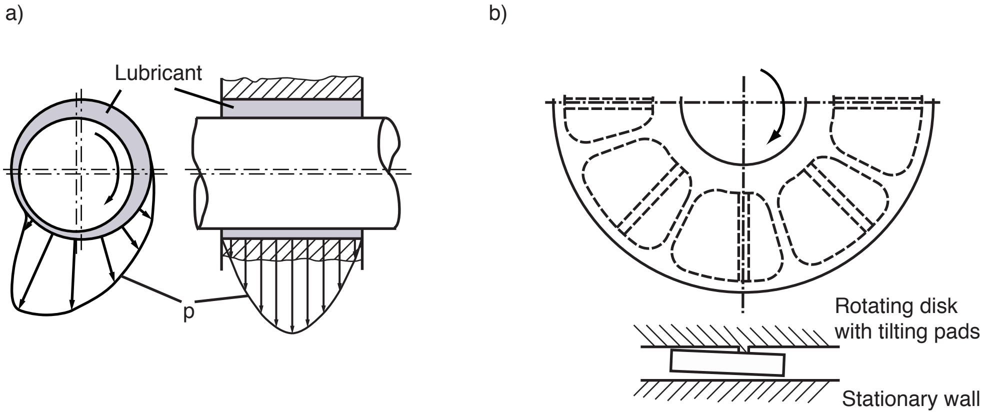

Figure A.2: Hydrodynamic bearings for radial and axial loads

Application of the continuity condition and a coordinate transformation to equation A.1, yields the unsteady pressure distribution for a radial bearing as shown in Figure A.2a as

$$\frac{1}{(D_J/2)^2}\frac{\partial}{\partial\varphi}\left[h^3\frac{\partial p}{\partial\varphi}\right]+\frac{\partial}{\partial z}\left[h^3\frac{\partial p}{\partial z}\right]=6\cdot\eta\cdot\omega\left\{\frac{\partial h}{\partial\varphi}+\frac{2}{\omega}\frac{\partial h}{\partial t}\right\} \tag{A.2}$$

Detailed derivations of equation A.2 can be found in [47], the definitions are presented in Figure A.3.

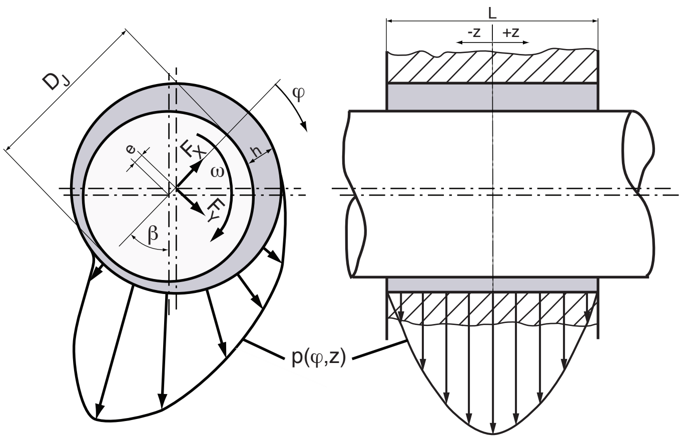

Figure A.3: Definitions for a journal bearing

The reaction force of the bearing can be found by the integration of the pressure distribution around the circumference as well as along the axial length of the bearing.

$$
\begin{aligned}
F_x &= \int_0^{\varpi} \int_{-L/2}^{L/2} pR \cos\varphi \, d\varphi \, dz \\
F_y &= \int_0^{\pi} \int_{-L/2}^{L/2} pR \sin\varphi \, d\varphi \, dz
\end{aligned}
\tag{A.3}
$$

The integration is performed only over half of the circumference, since the Sommerfeld boundary condition yields an antisymmetric solution about $\varphi = \pi$ with negative pressures between $\varphi = \pi$ and $\varphi = 2\pi$, which is unphysical, as Newtonian fluids can only carry pressure loads, but not tension loads.

Using the shaft eccentricity, defined as the ratio $\epsilon = e/\delta_B$, with δ_B being the radial clearance of the bearing, the attitude angle β, can be defined as

$$
\tan\beta = -\frac{F_x}{F_y} = \frac{\pi}{4} \frac{\sqrt{1-\epsilon^2}}{\epsilon}
\tag{A.4}
$$

The attitude angle defines the shaft centerline position with respect to the resultant load. This relationship describes approximately a semi-circle, the resulting curve is called the Gümbel curve (Figure A.4).

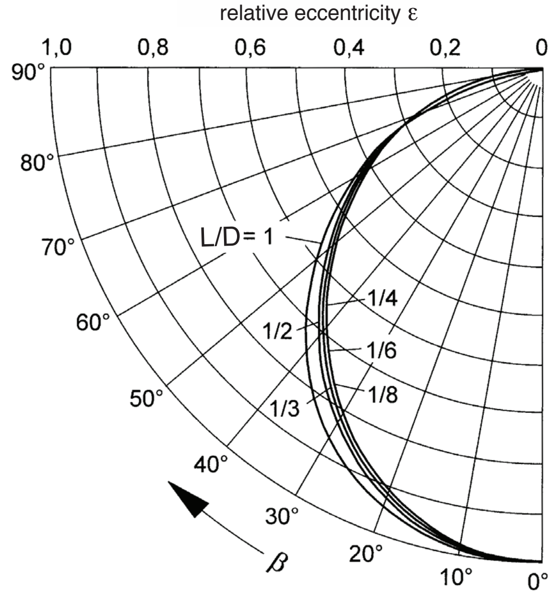

Figure A.4: Attitude angle in function of eccentricity and bearing length [11]

Bibliography

References

[1] Abramian, M., and Howard, J. H. G. Experimental investigation of the steady and unsteady relative flow in a model centrifugal impeller passage. *Journal of Turbomachinery 116*, 2 (1994), 269–279.

[2] Adkins, D., and Brennen, C. Analyses of hydrodynamic radial forces on centrifugal pump impellers. *Journal of Fluids Engineering, Transactions of the ASME 110*, 1 (1988), 20–28.

[3] Agostinelli, A., Nobles, D., and Mockridge, C. An experimental investigation of radial thrust in centrifugal pumps. *ASME J. Eng. for Power 82*, 2 (1960), 120–126.

[4] Akhras, A., El Hajem, M., Champagne, J.-Y., and Morel, R. The flow rate influence on the interaction of a radial pump impeller and the diffuser. *International Journal of Rotating Machinery 10*, 4 (2004), 309–317.

[5] Akin, O., and Rockwell, D. Interaction of zones of flow separation in a centrifugal impeller-stationary vane system. *Experiments in Fluids 17*, 6 (Oct. 1994), 427–433.

[6] Ardizzon, G., and Pavesi, G. Analysis of unsteady impeller diffuser interaction in a centrifugal pump. In *22nd IAHR Symposium on Hydraulic Machinery and Systems* (2004), IAHR.

[7] Arndt, N., Acosta, A., Brennen, C., and Caughey, T. Rotor-stator interaction in a diffuser pump. *Journal of Turbomachinery 111*, 3 (1989), 213–221.

[8] Arndt, N., Acosta, A., Brennen, C., and Caughey, T. Experimental investigation of rotor-stator interaction in a centrifugal pump with several vaned diffusers. *Journal of Turbomachinery 112*, 1 (1990), 98–108.

[9] Ausoni, P. *Turbulent vortex shedding from a blunt trailing edge hydrofoil.* PhD thesis, EPFL, Lausanne, 2009.

[10] Avellan, F., Etter, S., Gummer, J. H., and Seidel, U. Dynamic Pressure Measurements on a Model Turbine Runner and their Use in Preventing Runner Fatigue Failure. In *Proceedings of the 20th IAHR Symposium, Charlotte, North Carolina, USA, August* (2000).

[11] Beitz, W., and Grote, K.-H., Eds. *Dubbel - Taschenbuch für den Maschinenbau.* Springer, 2001.

[12] Benra, F.-K. Numerical and experimental investigation on the flow induced oscillations of a single-blade pump impeller. *Journal of Fluids Engineering 128*, 4 (2006), 783–793.

[13] Berten, S., Dupont, P., Farhat, M., and Avellan, F. Rotor-Stator Interaction Induced Pressure Fluctuations: CFD and Hydroacoustic Simulations in the Stationary Components of a Multistage Centrifugal Pump. In *Proceedings of FEDSM 2007* (2007).

[14] Bolleter, U. Blade passage tones of centrifugal pumps. *Vibrations 4*, 3 (September 1988), 8–13.

[15] Braun, O. *Part load flow in radial centrifugal pumps.* PhD thesis, EPFL, Lausanne, 2009.

[16] Bulot, N., and Trébinjac, I. Impeller-diffuser interaction: Analysis of the unsteady flow structures based on their direction of propagation. *Journal of Thermal Science 16*, 3 (2007), 193–202.

[17] Busemann, A. Das Förderhöhenverhältnis radialer Kreiselpumpen mit logarithmisch-spiraligen Schaufeln. *Z. Angew. Math. Mech 8* (1928), 372–384.

[18] Chamieh, D. S., Acosta, A. J., Brennen, C. E., and Caughey, T. K. Experimental measurements of hydrodynamic radial forces and stiffness matrices for a centrifugal pump-impeller. *Journal of Fluids Engineering, Transactions of the ASME 107*, 3 (1985), 307–315.

[19] Chen, Y. Water-pressure oscillations in the volute casings of storage pumps. *Sulzer Technical Review*, Research Number (1961), 21–34.

[20] Chen, Y., Chen, J., Seidel, U., Haupt, U., and Rautenberg, M. Experimental investigation of the flow field of deep rotating stall in a centrifugal compressor. In *Proceedings of the International Gas Turbine and Aeroengine Congress and Exposition 1994* (Hague, Neth, 1994), ASME, pp. 1–8.

[21] Chen, Y. N., Haupt, U., and Rautenberg, M. Rossby waves and associated transient rotating stall vortices in radial and axial turbocompressors. *Zeitschrift für Flugwissenschaften und Weltraumforschung 14* (Aug. 1990), 233–246.

[22] Childs, D. Fluid-structure interaction forces at pump-impeller-shroud surfaces for axial vibration analysis. *ASME J. Vibr. Acoust. 113* (1991), 108–115.

[23] Childs, D. Pressure oscillation in the leakage annulus between a shrouded impeller and its housing due to impeller-discharge-pressure disturbances. *Journal of Fluids Engineering, Transactions of the ASME 114*, 1 (1992), 61–67.

[24] Cizmas, P. G. A., and Palacios, A. Proper orthogonal decomposition of turbine rotor-stator interaction. *Journal of Propulsion and Power 19*, 2 (2003), 268–281.

[25] Cooley, J. W., and Tukey, J. W. An algorithm for the machine calculation of complex fourier series. *Math. Comput.*, 19 (1965), 297–301.

[26] Coutu, A., Roy, M., Monette, C., and Nennemann, B. Experience with rotor-stator interactions in high head francis runner. In *24th Symposium on Hydraulic Machinery and Systems* (2008), IARH. OCTOBER 27-31, FOZ DO IGUASSU.

[27] Day, I. Active suppression of rotating stall and surge in axial compressors. *Journal of Turbomachinery 115*, 1 (1993), 40–47.

[28] Den Hartog, J. Mechanical vibrations in penstocks of hydraulic machinery. *Trans. Amer. Society of Mechanical Engineers, Hydraulics* (1930), 101–110.

[29] Deniz, S., Greitzer, E., and Cumpsty, N. Effects of inlet flow field conditions on the performance of centrifugal compressor diffusers: Part 2-straight-channel diffuser. *J. Turbomach. 122*, 1 (2000), 11–21.

[30] Doerfler, P. On the role of phase resonance in vibrations caused by blade passage in radial hydraulic turbomachines. In *12th IAHR Symp. on Hydraulic Machinery in the Energy Related Industries* (Aug. 27-30 1984), IAHR, pp. 228–241.

[31] Dring, R., Joslyn, H., Hardin, L., and Wagner, J. Turbine rotor-stator interaction. *Journal of Engineering for Power 104* (1982), 729–742.

[32] Dupont, P., Caignaert, G., Bois, G., and Schneider, T. Rotor-stator interactions in a vaned diffuser radial flow pump. In *Proceedings of 2005 ASME Fluids Engineering Division Summer Meeting, FEDSM2005* (Houston, TX, 2005), vol. 2005, pp. 976–983.

[33] Eckert, L. Radial wheel damages as a result of aeroelastic self excited wheel vibrations. *VDI Berichte*, 1606 (2001), 259–278.

[34] Eisele, K., Zhang, Z., Casey, M., Gülich, J., and Schachenmann, A. Flow analysis in a pump diffuser - part 1: LDA and PTV measurements of the unsteady flow. *ASME Journal of Fluids Engineering 119*, 4 (1997), 968–977.

[35] Eisinger, F. Acoustic fatigue of impellers of rotating machinery. *Flow-Induced Vibration, Volume 2: Axial Flow, Piping Systems, Other Topics ASME PVP-VOL. 4202-2* (2001), 154–160.

[36] Eisinger, F., and Sullivan, R. Acoustically-induced structural fatigue of impeller discs - a brief note. In *American Society of Mechanical Engineers, International Gas Turbine Institute, Turbo Expo (Publication) IGTI* (2002), vol. 5 B, pp. 1063–1070.

[37] Emmons, H., Kronauer, R., and Rockett, J. A survey of stall propagation-experiment and theory. *ASME Journal of Basic Engineering 81* (1959), 409–416.

[38] Farhat, M., Avellan, F., and Seidel, U. Pressure Fluctuation Measurements in Hydro Turbine Models. In *Proceedings of the 9th International Symposium on Transport Phenomena and Dynamics of Rotating Machinery, Honolulu, Hawaii, USA, February* (2002).

[39] Farhat, M., Natal, S., Avellan, F., Paquet, F., Lowys, P. Y., and Couston, M. Onboard Measurements of Pressure and Strain Fluctuations in a Model of low Head Francis Turbine. part 1 : Instrumentation. In *Proceedings of the 21st IAHR Symposium on Hydraulic Machinery and Systems* (2002), pp. 865–872.

[40] Feng, J., Benra, F.-K., and Dohmen, H. Numerical investigation on pressure fluctuations for different configurations of vaned diffuser pumps. *International Journal of Rotating Machinery 2007* (2007), 1–10.

[41] Filipenco, V., Deniz, S., Johnston, J., Greitzer, E., and Cumpsty, N. Effects of inlet flow field conditions on the performance of centrifugal compressor diffusers: Part 1 - discrete passage diffuser. *Journal of Turbomachinery 122*, 1 (2000), 1–10.

[42] Fisher, R., Seidel, U., Grosse, G., Gfeller, W., and Klinger, R. A case study in resonant hydroelastic vibration: The causes of runner cracks and

the solutions implemented for the xiaolangdi hydroelectric project. In *Proceedings of the XXIst IAHR Symposium on Hydraulic Machinery and Systems* (Lausanne, September 2002), IAHR.

[43] Fox, R., and Kline, S. Flow regimes in curved subsonic diffusers, trans. *ASME, J. of Basic Engineering 84* (1962).

[44] Franke, G., Powell, C., Seidel, U., Koutnik, J., and Fisher, R. On pressure mode shapes arising from rotor stator interactions. In *IAHR WG1-2003 Meeting* (2003).

[45] Frigne, P., and Van Den Braembussche, R. Distinction between different types of impeller and diffuser rotating stall in a centrifugal compressor with vaneless diffuser. *J Eng Gas Turbines Power Trans ASME 106* (1984), 468–474.

[46] Gantar, M., Florjancic, D., and Sirok, B. Hydraulic axial thrust in multistage pumps—origins and solutions. *Journal of Fluids Engineering 124*, 2 (2002), 336–341.

[47] Gohar, R., and Rahnejat, H. *Fundamentals of Tribology.* Imperial College Press, 2008.

[48] González, J., Fernández, J., Blanco, E., and Santolaria, C. Numerical simulation of the dynamic effects due to impeller-volute interaction in a centrifugal pump. *Journal of Fluids Engineering, Transactions of the ASME 124*, 2 (2002), 348–355.

[49] Gostelow, J. A new approach to the experimental study of turbomanchinery flow phenomena. *Journal of engineering for power 99* (January 1977), 97–105.

[50] Goswami, J. C., and Hoefel, A. E. Algorithms for estimating instantaneous frequency. *Signal Processing 84*, 8 (Aug. 2004), 1423–1427.

[51] Goto, A. Suppression of mixed-flow pump instability and surge by the active alteration of impeller secondary flows. *Journal of Turbomachinery 116*, 4 (1994), 621–628.

[52] Goto, A., Takemura, T., and Zangeneh, M. Suppression of secondary flows in a mixed-flow pump impeller by application of three-dimensional inverse design method: Part 2 - experimental validation. *Journal of Turbomachinery 118*, 3 (1996), 544–551.

[53] Greitzer, E. Stability of pumping systems - the 1980 freeman scholar lecture. *Journal of Fluids Engineering, Transactions 103*, 2 (June 1981), 193–242.

[54] Guelich, J., and Egger, R. Part-load flow and hydraulic stability of centrifugal pumps. Tech. Rep. TR-100219, EPRI, 3412 Hillview Avenue, Palo Alto, California, 1992.

[55] Guelich, J., Jud, W., and Hughes, S. Review of parameters influencing hydraulic forces on centrifugal impellers. *Proceedings of the Institution of Mechanical Engineers. Part A. Power and process engineering 20 l*, 3 (1987), l63–174.

[56] Guelich, J. F. *Kreiselpumpen*, 2nd ed. Springer-Verlag, Berlin Heidelberg New York, 2004.

[57] Guelich, J. F., and Bolleter, U. Pressure pulsations in centrifugal pumps. *Journal of Vibration and Acoustics 114*, 2 (1992), 272–279.

[58] Guo, S., and Maruta, Y. Experimental investigations on pressure fluctuations and vibration of the impeller in a centrifugal pump with vaned diffusers. *JSME International Journal, Series B: Fluids and Thermal Engineering 48*, 1 (February 2005), 136–143.

[59] Hasegawa, Y., Kikuyama, K. Maeda, T., and Murakami, M. Unsteady pressure distibutions and forces on the impeller blades of a centrifugal pump. In *IAHR Symposium 1990 Belgrade* (1990), IAHR, pp. 1–12.

[60] Haupt, U., Seidel, U., Abdel-Hamid, A., and Rautenberg, M. Unsteady flow in a centrifugal compressor with different types of vaned diffusers. *J Turbomach 110*, 3 (1988), 293–302.

[61] Hergt, P., and Benner, R. Visuelle Untersuchung der Strömung im Leitrad einer Kreiselpumpe. *Schweizerische Bauzeitung 86*, 40 (1968), 716–720.

[62] Hergt, P., and Krieger, P. Radial forces in centrifugal pumps with guide vanes. In *Proc. Inst. Mech. Eng.* (1970), vol. 184, Part 3N, pp. 101–107.

[63] Higashiura, M., Aoki, H., Morioka, T., and Honami, S. A separation control of the diffuser flow by the vortex generator jets. *Transactions of the Japan Society of Mechanical Engineers, Part B 70*, 696 (2004), 2012–2017.

[64] Hirschberger, M., and James, I. A review of nss limitations - new opportunities. In *Proceedings of the twenty-fifth International Pump Users Symposium* (2009).

[65] Hodkiewicz, M. R. *The effect of partial-flow operation on the axial vibration of double-suction centrifugal pumps.* PhD thesis, The University of Western Australia, 2005.

[66] Hoffmann, K. *Anwendung der Wheatstoneschen Brückenschaltung.* HBM, 1973.

[67] Horiguchi, H., Ueno, Y., Takahashi, K., Miyagawa, K., and Tsujimoto, Y. Dynamic characteristics of the radial clearance flow between axially oscillating rotational disk and stationary disk. *International Journal of Fluid Machinery and Systems 2* (2009), 147–155.

[68] Horlock, J., and Lakshminarayana, B. Secondary flows : Theory, experiment and application in turbomachinery aerodynamics. *In : Annual Review Of Fluid Mechanics Book: Publ. By Annual Reviews Inc., U.S.A. 5* (1973), 1973.

[69] Hsu, Y., and Brennen, C. E. Fluid flow equations for rotordynamic flows in seals and leakage paths. *Journal of Fluids Engineering 124*, 1 (2002), 176–181.

[70] Iino, T. Potential interaction between a centrifugal impeller and a vaned diffuser. *ASME Fluid/Structure Interactions in Turbomachinery* (1981), 63–69.

[71] Inoue, M., and Cumpsty, N. Experimental study of centrifugal discharge flow in vaneless and vaned diffusers. *ASME Journal of Engineering Gas Turbines and Power 106* (1988), 455–467.

[72] Inoue, M., Kuroumaru, M., Yoshida, S., and Furukawa, M. Short and long length-scale disturbances leading to rotating stall in an axial compressor stage with different stator/rotor gaps. *Journal of Turbomachinery 124*, 3 (2002), 376–384.

[73] Ishida, M., Sakaguchi, D., and Ueki, H. Suppression of rotating stall by wall roughness control in vaneless diffusers of centrifugal blowers. *Journal of Turbomachinery 123*, 1 (2001), 64–72.

[74] Jaberg, H., and Hergt, P. Flow patterns at exit of radial impellers at part load and their relation to head curve stability. In *Pumping Machinery. Papers Presented at 3rd Joint ASCE/ASME Mechanics Conf.* (San Diego, CA, USA, 1989), vol. 81, ASME, pp. 213–225.

[75] Johnson, D., Pedersen, N., and Jacobsen, C. Measurements of rotating stall inside a centrifugal pump impeller. In *Proceedings of FEDSM2005 2005 ASME Fluids Engineering Division Summer Meeting and Exhibition* (June 19-23 2005).

[76] Johnston, J. P., and Nishi, M. Vortex generator jets. means for flow separation control. *AIAA Journal 28*, 6 (1990), 989–994.

[77] Jong, J., McBride, J., Jones, J., Fiorucci, T., and Zoladz, T. Synchronous phase averaging method for machinery diagnostics. In *MFPT 50 Proceedings* (1998), Society for Machinery Failure Prevention Technology.

[78] Kemp, N., and Sears, W. Aerodynamic interference between moving blade rows. *Journal of the Aeronautical Sciences 20*, 9 (1953), 585–597.

[79] Kline, S. On the nature of stall. *J. Basic Eng. 81*, 3 (1959), 305–320.

[80] Krause, N., Zähringer, K., and Pap, E. Time-resolved particle imaging velocimetry for the investigation of rotating stall in a radial pump. *Experiments in Fluids 39*, 2 (2005), 192–201.

[81] Lauer, J. *Einfluß der Eintrittsbedingung und der Geometrie auf die Strömung in den Radseitenräumen von Kreiselpumpen.* PhD thesis, Technische Universität Darmstadt, 1999.

[82] Lockey, K., Keller, M., Sick, M., Staehle, M., and Gehrer, A. Flow-induced vibrations at stayvanes: Experience on site and cfd simulations. *International Journal on Hydropower and Dams 13*, 5 (2006), 102–106.

[83] Longatte, F., and Kueny, J.-L. Analysis of rotor-stator-circuit interactions in a centrifugal pump. In *Proceedings of the 3rd ASME/JSME Joint Fluids Engineering Conference* (1999), ASME.

[84] Makay, E., and Szamody, O. Survey of feed pump outages. Tech. Rep. FP-754, EPRI, 1978.

[85] McDougall, N. M., Cumpsty, N. A., and Hynes, T. P. Stall inception in axial compressors. *Journal of Turbomachinery 112*, 1 (1990), 116–123.

[86] McFadden, P. D. A revised model for the extraction of periodic waveforms by time domain averaging. *Mechanical Systems and Signal Processing 1*, 1 (Jan. 1987), 83–95.

[87] Meschkat, S. *Experimentelle Untersuchung der Auswirkungen instationärer Rotor-Stator-Wechselwirkungen auf das Betriebsverhalten einer Spiralgehäusepumpe.* PhD thesis, TU Darmstadt, 2004.

[88] Miskovish, R., and Brennen, C. Some unsteady fluid forces on pump impellers. *Journal of Fluids Engineering, Transactions of the ASME 114*, 4 (1992), 632–637.

[89] Miyabe, M., Furukawa, A., Maeda, H., Umeki, I., and Jittani, Y. A behavior of the diffuser rotating stall in a low specific speed mixed-flow pump. *International Journal of Fluid Machinery and Systems 2* (2009), 31–39.

[90] Miyabe, M., Maeda, H., Umeki, I., and Jittani, Y. Unstable head-flow characteristic generation mechanism of a low specific speed mixed flow pump. *Journal of Thermal Science 15*, 2 (June 2006), 115–120.

[91] Möhring, U. *Untersuchung des radialen Druckverlaufes und des übertragenen Drehmoments im Radseitenraum von Kreiselpumpen bei glatter, ebener Radseitenwand und bei Anwendung von Rückenschaufeln.* PhD thesis, TU Braunschweig, 1976.

[92] Moore, J. J., and Palazzolo, A. B. Rotordynamic force prediction of whirling centrifugal impeller shroud passages using computational fluid dynamic techniques. *Journal of Engineering for Gas Turbines and Power 123*, 4 (2001), 910–918.

[93] Morgenroth, M., and Weaver, D. Sound generation by a centrifugal pump at blade passing frequency. *Journal of Turbomachinery 120*, 4 (1998), 736–743.

[94] Murakami, M., Kikuyama, K., and Asakura, E. Velocity and pressure distributions in the impeller passages of centrifugal pumps. *Journal of Fluids Engineering, Transactions of the ASME 102*, 4 (1980), 420–426.

[95] Nishi, M., Yoshida, K., and Morimitsu, K. Control of separation in a conical diffuser by vortex generator jets. *JSME international journal. Ser. B, Fluids and thermal engineering 41*, 1 (1998), 233–238.

[96] Ohashi, H. Case study of pump failure due to rotor-stator interaction. *International Journal of Rotating Machinery 1*, 1 (1994), 53–60.

[97] Osada, T., Kawakami, T., Yokoi, T., and Tsujimoto, Y. Field study on pump vibration and iso's new criteria. *Journal of Fluids Engineering, Transactions of the ASME 121*, 4 (1999), 798–803.

[98] Paduano, J., Epstein, A., Valavani, L., Longley, J., Greitzer, E., and Guenette, G. Active control of rotating stall in a low speed axial compressor. In *Conference of International Gas Turbine and Aeroengine Congress and Exposition* (1991), ASME.

[99] Parrondo-Gayo, J., González-Pérez, J., and Fernández-Francos, J. The effect of the operating point on the pressure fluctuations at the blade passage frequency in the volute of a centrifugal pump. *Journal of Fluids Engineering, Transactions of the ASME 124*, 3 (2002), 784–790.

[100] Pedersen, N., Byskow, R., and Jacobsen, C. Flow in a centrifugal pump impeller at design and off-design conditions - part II: Large eddy simulations. *Journal of Fluids Engineeering 125* (January 2003), 73–83.

[101] Pedersen, N., Larsen, P., and Jacobsen, C. Flow in a centrifugal pump impeller at design and off-design conditions - part I: Particle image velocimetry (piv) and laser doppler velocimetry (ldv) measurements. *Journal of Fluids Engineeering 125* (January 2003), 61–72.

[102] Pereira, F., Farhat, M., and Avellan, F. Dynamic calibration of transient sensors by spark generated cavity. In *Proceedings of IUTAM Symposium on Bubble Dynamics and Interface Phenomena* (1999).

[103] Pfleiderer, C. *Die Kreiselpumpen für Flüssigkeiten und Gase : Wasserpumpen, Ventilatoren, Turbogebläse, Turbokompressoren.* Springer, Berlin, Heidelberg, New York, 1961.

[104] Poncet, S., and Chauve, M.-P. Crossflow instability in rotor-stator flows with axial inward throughflow. *Journal of Fluid Mechanics 545*, -1 (2005), 281–289.

[105] Prakash, O., and Pandey, R. Failure analysis of the impellers of a feed pump. *Engineering Failure Analysis 3*, 1 (1996), 45–52.

[106] Prasad, J., Neumeier, Y., Lal, M., Bae, S., and Meehan, A. Experimental investigation of active and passive control of rotating stall in axial compressors. In *Proceedings of the 1999 IEEE International Conference on Control Applications (CCA) and IEEE International Symposium on Computer Aided Control System Design (CACSD)* (1999), vol. 2, IEEE, pp. 985–990.

[107] Pérez, J. G., Morros, C. S., Gayo, J. L. P., Francos, J. F., and Marigorta, E. B. Unsteady radial forces on the impeller of a centrifugal pump with radial gap variation. In *Proceedings of the ASME FEDSM03* (2003).

[108] Qin, W., and Tsukamoto, H. Theoretical study of pressure fluctuations downstream of a diffuser pump impeller - part 1: Fundamental analysis on rotor-stator interaction. *J Fluids Eng Trans ASME 119*, 3 (1997), 647–652.

[109] Rebernik, B. Radialkräfte von Kreiselpumpen mit unterschiedlichen Gehäuseformen. In *"25 Jahre ASTRÖ"*. Aströ, Graz, 1979, pp. 55–60.

[110] Rose, M. Low flowrate effects in a centrifugal pump impeller. *Proc. Inst. Mech. Eng. Part A J. Power Eng. 218*, 6 (2004), 417–427.

[111] Saha, S. L., Kurokawa, J., Matsui, J., and Imamura, H. Passive control of rotating stall in a parallel-wall vaned diffuser by j-grooves. *Journal of Fluids Engineering 123*, 3 (2001), 507–515.

[112] Sano, T., Nakamura, Y., Yoshida, Y., and Tsujimoto, Y. Alternate blade stall and rotating stall in a vaned diffuser. *JSME Int. J. Ser. B Fluids Therm. Eng. 45*, 4 (2002), 810–819.

[113] Sano, T., Yoshida, Y., Tsujimoto, Y., Nakamura, Y., and Matsushima, T. Numerical study of rotating stall in a pump vaned diffuser. *Journal of Fluids Engineering, Transactions of the ASME 124*, 2 (2002), 363–370.

[114] Schneider, K. *Das Verhalten von Kreiselpumpen beim Auftreten von Druckwellen.* PhD thesis, Universität Stuttgart, 1986.

[115] Schwartz, R. E., and Nelson, R. M. Acoustic resonance phenomena in high energy variable speed centrifugal pumps. In *Proceedings of the 1st International Pump Users Symposium* (Texas A&M University, Houston, TX, 1984), pp. 23–28.

[116] Shannon, C. E. Communication in the presence of noise. *Proceedings of IRE 37* (1949), 10–21.

[117] Shi, F., and Tsukamoto, H. Numerical study of pressure fluctuations caused by impeller-diffuser interaction in a diffuser pump stage. *Journal of Fluids Engineering 123* (September 2001), 466–474.

[118] Shi, Q. Abnormal noise and runner cracks caused by von karman vortex shedding: a case study in dachaoshan hydroelectric project. In *Proceedings of the 22nd IAHR Symposium on Hydraulic Machinery and Systems* (Stockholm, 2004), IARH.

[119] Sinha, M., Pinarbasi, A., and Katz, J. The flow structure during onset and developed states of rotating stall within a vaned diffuser of a centrifugal pump. *Journal of Fluids Engineering, Transactions of the ASME 123*, 3 (2001), 490–499.

[120] Spakovszky, Z. S. Backward traveling rotating stall waves in centrifugal compressors. *Journal of Turbomachinery 126*, 1 (2004), 1–12.

[121] Spence, R., and Amaral-Teixeira, J. Investigation into pressure pulsations in a centrifugal pump using numerical methods supported by industrial tests. *Computers and Fluids 37*, 6 (2008), 690–704.

[122] Spence, R., and Amaral-Teixeira, J. A cfd parametric study of geometrical variations on the pressure pulsations and performance characteristics of a centrifugal pump. *Computers & Fluids 38*, 6 (2009), 1243 – 1257.

[123] Stanmore, L. Field problems relating to high-energy centrifugal pumps operating at part-load. In *Conference on Part-load Pumping Operation, Control and Behaviour* (London, Edinburgh, 1988), M. E. Publications, Ed., pp. 109–121.

[124] Stenning, S. Rotating stall and surge. *Journal of Fluids Engineering, Transactions of the ASME 102*, 1 (1980), 14–20.

[125] Stoffel, B. Experimentelle Untersuchungen zur räumlichen und zeitlichen Struktur der Teillast-Rezirkulationen bei Kreiselpumpen. *Forschung im Ingenieurwesen 55*, 5 (1989), 149–152.

[126] Stoffel, B., and Krieger, P. Experimental investigation on the energy balance of radial centrifugal pump impellers at part load conditions. In *Proceedings of the Hydraulic Machinery and Systems, IAHR Symposium* (1981).

[127] Sutton, G. History of liquid propellant rocket engines in the united states. *Journal of Propulsion and Power 19*, 6 (2003), 978–1007.

[128] Tamm, A. *Beitrag zur Bestimmung der Wirkungsgrade einer Kreiselpumpe durch theoretische, numerische und experimentelle Untersuchungen.* PhD thesis, TU Darmstadt, 2002.

[129] Tanaka, H. Vibration behaviour and dynamic stress of runners of very high head reversible pump-turbines. In *IAHR Symposium 1990 Belgrade* (1990), IAHR.

[130] Tsujimoto, Y., Yoshida, Y., Ohashi, H., Teramoto, N., and Ishizaki, S. Fluid force moment on a centrifugal impeller shroud in processing motion. *J Fluids Eng Trans ASME 119*, 2 (1997), 366–371.

[131] Ubaldi, M., Zunino, P., Barigozzi, G., and Cattanei, A. An experimental investigation of stator induced unsteadiness on centrifugal impeller outflow. *Journal of Turbomachinery 118* (1996), 41–51.

[132] Verhoeven, J. Excitation force identification of rotating machines using operational rotor/stator amplitude data and analytical synthesized transfer functions. *Journal of vibration, acoustics, stress, and reliability in design 110*, 3 (1988), 307–314.

[133] Verhoeven, J. Unsteady hydraulic forces in centrifugal pumps. In *Conference on Part-load Pumping Operation, Control and Behaviour* (London, Edinburgh, 1988), Mechanical Engineering Publications, pp. 153–165.

[134] von Backström, T. A unified correlation for slip factor in centrifugal impellers. *Journal of Turbomachinery 128*, 1 (2006), 1–10.

[135] Wang, H., and Tsukamoto, H. Fundamental analysis on rotor-stator interaction in a diffuser pump by vortex method. *Journal of Fluids Engineering, Transactions of the ASME 123*, 4 (2001), 737–747.

[136] Wang, H., and Tsukamoto, H. Experimental and numerical study of unsteady flow in a diffuser pump at off-design conditions. *Journal of Fluids Engineering, Transactions of the ASME 125*, 5 (2003), 767–778.

[137] Wesche, W. *Experimentelle Untersuchungen am Leitrad einer radialen Kreiselpumpe.* PhD thesis, TU Braunschweig, 1989.

[138] Wiesner, F. A review of slip factors for centrifugal impellers. *Trans. ASME, J. Engng Pwr 89*, 4 (1967), 558–572.

[139] Yoshida, Y., Murakami, Y., Tsurusaki, H., and Tsujimoto, Y. Rotating stalls in centrifugal impeller/vaned diffuser systems. In *Proc. First ASME/JSME Joint Fluids Eng. Conf., FED-107* (1991), ASME/JSME, pp. 125–130.

[140] Zangeneh, M., Goto, A., and Harada, H. On the design criteria for suppression of secondary flows in centrifugal and mixed flow impellers. *Journal of Turbomachinery 120*, 4 (1998), 723–735.

[141] Zangeneh, M., Goto, A., and Takemura, T. Suppression of secondary flows in a mixed-flow pump impeller by application of three-dimensional inverse design method: Part 1 - design and numerical validation. *Journal of Turbomachinery 118*, 3 (1996), 536–543.

[142] Zhang, M., and Tsukamoto, H. Unsteady hydrodynamic forces due to rotor-stator interaction on a diffuser pump with identical number of vanes on the impeller and diffuser. *Journal of Fluids Engineering, Transactions of the ASME 127*, 4 (2005), 743–751.

[143] Zhu, B., and Kamemoto, K. Numerical simulation of unsteady interaction of centrifugal impeller with its diffuser using lagrangian discrete vortex method. *Acta Mechanica Sinica/Lixue Xuebao 21*, 1 (2005), 40–46.

[144] Zilling, H. Investigation of the axial thrust and the flow in the lateral spaces between impeller and casing of a single-stage centrifugal pump with diffuser. [Untersuchung des Axialschubs und der Stroemungsvorgaenge in den Radseitenraeumen einer einstufigen radialen Kreiselpumpe mit Leitrad.]. *Stroemungsmech Stroemungsmasch*, 15 (1973), 1–47.

[145] Zobeiri, A. *Investigations of time dependent flow phenomena in a turbine and a pump-turbine of Francis type.* PhD thesis, EPFL, Lausanne, 2009.

[146] Zobeiri, A. Vortex shedding from blunt and oblique trailing edge hydrofoils. In *3rd IAHR International Meeting of the Workgroup on Cavitation and Dynamic Problems in Hydraulic Machinery and Systems* (Brno, Czech Republic, October 2009), IARH.

Stefan BERTEN

Schlossmühlestrasse 252
CH-8408 Winterthur, Switzerland

Tel.: +41 52 202 8571
Mobile: +41 79 412 6958
E-mail: stefan.berten@solnet.ch

Born: 5. 7.1967 in Rostock (Gemany)
Nationality: German

EDUCATION

2005-2009:	**PhD in engineering science** École Polytechnique Fédérale de Lausanne (EPFL), Switzerland
1990-1995:	**Dipl.-Ing. Maschinenbau** Otto-von-Guericke University, Magdeburg, Germany
1985-1987	**Abitur** Volkshochschule Rostock
1984-1986:	**Maschinen und Anlagenmonteur** Dieselmotorenwerk Rostock, Germany

PROFESSIONAL EXPERIENCE

2010-:	**Sulzer Pumps, Winterthur, Switzerland** Research Engineer in Hydraulic Development Group
2005-2009:	**École Polytechnique Fédérale de Lausanne (EPFL), Switzerland. Laboratory for Hydraulic Machines (LMH).** Doctoral thesis: Hydrodynamics of High Specific Power Pumps for Off-Design Conditions
2000-2005:	**Sulzer Pumps, Winterthur, Switzerland** Research Engineer in Hydraulic Development Group
1995-2000:	**Sulzer Pumpen Deutschland GmbH, Germany** Hydraulic Design Engineer
1990	**Dieselmotorenwerk Rostock, Germany** Mechanic (Assembly of ship diesel engines)
1987-1990:	**Military service**
1986-1987:	**Dieselmotorenwerk Rostock, Germany** Mechanic (Assembly of ship diesel engines)

INFORMATICS

OS:	Windows, MS-DOS, Unix (Linux, OS-X).
Programming:	Fortran, Matlab, Visual Basic.
CFD:	CFX, ICEM.
CAD:	Unigraphics, Medusa.
Office:	MS-Office, Latex.
Multimedia:	MS-Office, Suite Adobe, HTML.

LANGUAGES

German	Native speaker.
English	Conversational.
French	Conversational.
Russian	Basic.